NUREG/CR-3948
EGG-2297

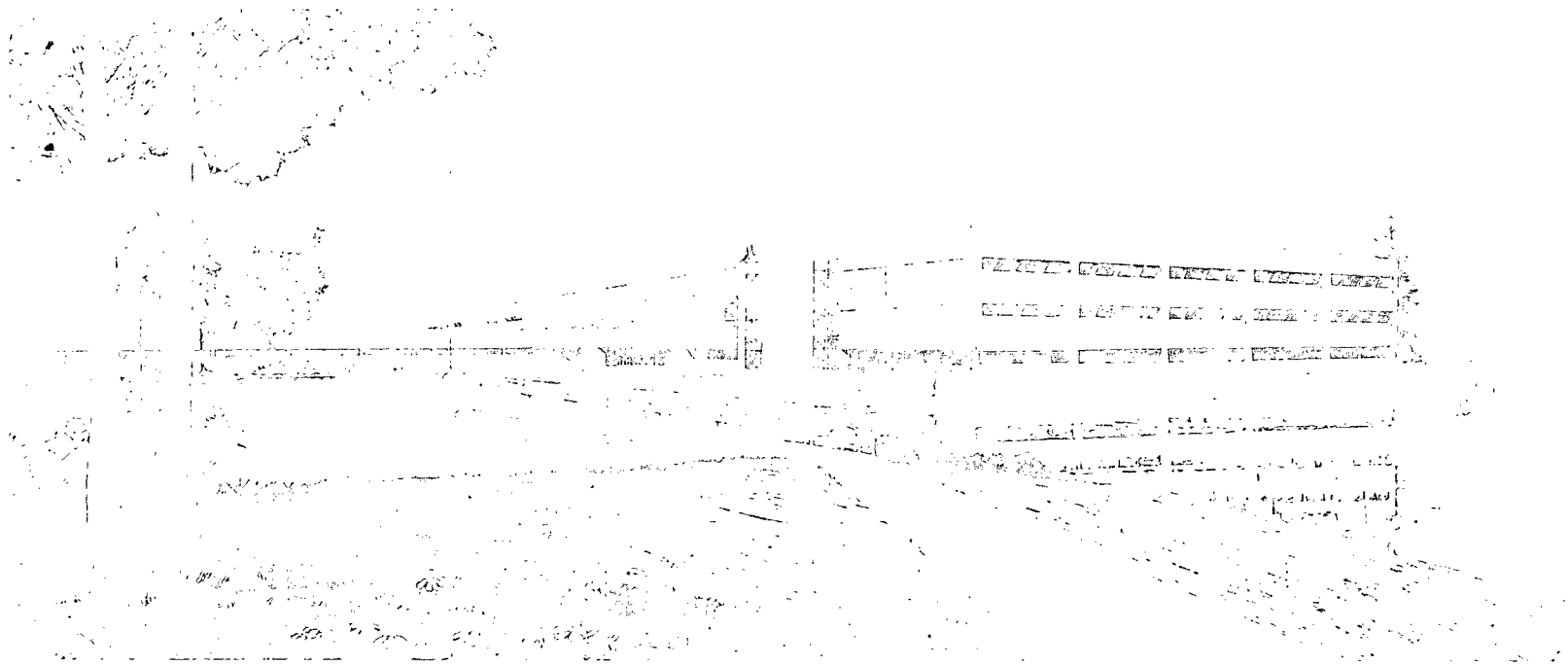

Idaho National Engineering Laboratory
Operated by the U.S. Department of Energy

Experimental Results of the Operational Transient (OPTRAN) Tests 1-1 and 1-2 in the Power Burst Facility

Richard K. McCardell
Scott A. Ploger
Robert D. McCormick
Vikram N. Shah

June 1985

Prepared for the
U.S. Nuclear Regulatory Commission
Under DOE Contract No. DE-AC07-76IDO1570

EG&G Idaho

Available from

Superintendent of Documents
U.S. Government Printing Office
Post Office Box 37082
Washington, D.C. 20013-7982

and

National Technical Information Service
Springfield, VA 22161

NOTICE

This report was prepared as an account of work sponsored by an agency of the United States Government. Neither the United Sates Government nor any agency thereof, nor any of their employees, makes any warranty, expressed or implied, or assumes any legal liability or responsibility for any third party's use, or the results of such use, of any information, apparatus, product or process disclosed in this report, or represents that its use by such third party would not infringe privately owned rights.

NUREG/CR-3948
EGG-2297
Distribution Category: R3

EXPERIMENTAL RESULTS OF THE OPERATIONAL TRANSIENT (OPTRAN) TESTS 1-1 AND 1-2 IN THE POWER BURST FACILITY

Richard K. McCardell
Scott A. Ploger
Robert D. McCormick
Vikram N. Shah

Published June 1985

EG&G Idaho, Inc.
Idaho Falls, Idaho 83415

Prepared for the
U.S. Nuclear Regulatory Commission
Washington, D.C. 20555
Under DOE Contract No. DE-AC07-76IDO1570
FIN No. A6305

ABSTRACT

Operational transients occur occasionally in light water reactors when minor malfunctions of certain system components affect the reactor core. Potential effects of such malfunctions include a loss of the secondary heat sink, an increase in system pressure, and, in boiling water reactors (BWR), void collapse and a brief increase in reactor power. This report presents the results of the operational transient Tests OPTRAN 1-1 and OPTRAN 1-2, including a comparison of the data with posttest calculations and the postirradiation examination results. The OPTRAN 1-1 tests simulated operational transients with reactor scram. Four progressively higher and broader power transients at a constant coolant flow rate were performed. The first transient simulated a BWR-5 turbine trip without steam bypass, with fuel rods operating near BWR-6 core average rod powers. The second transient simulated a generator load rejection without steam bypass, with fuel rods operating near core average powers. The last two transients were performed at higher core average peak rod powers than safety analyses predict to be possible in commercial reactors to define failure threshold margins.

Test OPTRAN 1-2 was performed to evaluate the probability and extent of fuel rod damage for the most severe BWR anticipated transient without scram (ATWS) that results in boiling transition, a main steam line isolation valve closure transient without scram. Two sets of two fuel rods were tested. In each set, an unirradiated fuel rod was used to heat the coolant to typical BWR conditions for each previously irradiated fuel rod. Following an extensive fuel conditioning period of operation, a single power transient was performed that simulated the power history and coolant conditions calculated for a main steam line isolation valve closure ATWS.

FIN No. A6305—TFBP Severe Fuel Damage Studies

EXECUTIVE SUMMARY

Anticipated nuclear power reactor transients are deviations from normal plant operating conditions that may result from system component malfunctions or reactor operating errors that may occur one or more times during the service life of a reactor and are normally accompanied by a control rod scram. They are distinguished from accidents, which have a much lower probability of occurrence and may result in much more severe consequences. The effects of the anticipated system component malfunctions may include a loss of the secondary heat sink, an increase in coolant system pressure, and, in boiling water reactors, void collapse and a brief surge in reactor power. Dryout and severe cladding temperature excursions are not expected during such transients and, therefore, the damage mechanism of concern is cladding fracture due to pellet-cladding mechanical and chemical interactions (PCI).

Fuel rod cladding fracture due to a PCI mechanism has been recognized as a problem since 1964. Such failures are apparently induced by power increases after a sufficiently high burnup is attained to allow fission product release. There has been a strong incentive to find a remedy for these failures because the present method of prevention is to accept limits on rates of reactor power increase. These limits are very expensive due to the lost power output during slow increases, especially for load follow operations. Most investigators now accept the view that both the presence of aggressive chemical species and high localized stresses are prerequisites for power-ramp-induced PCI failures.

Severe core power increases are possible during a variety of anticipated transients and yet the most severe postulated anticipated transients have not occurred in commercial reactors. Therefore, the U.S. Nuclear Regulatory Commission (NRC) was uncertain whether light water reactor fuel rods would fail or can be damaged during such events. For anticipated transient conditions, the commonly used overheating fuel failure criteria may not be appropriate for PCI damage. Therefore, a series of in-pile fuel behavior tests designated OPTRAN 1-1 were conducted in the Power Burst Facility (PBF) by EG&G Idaho, Inc., for the NRC to (a) determine the threshold at which light water reactor fuel rods are likely to fail during severe anticipated transients that result in a brief increase in reactor power and (b) identify any fuel rod damage mechanisms that might occur.

Six fuel rods were tested in the OPTRAN 1-1 test series. All six test fuel rods were originally fabricated by the General Electric Company (GE) and irradiated in the Northern States Power Company's Monticello boiling water reactor (SRP II bundle) to burnups ranging from about 5000 to 22,000 MWd/t. Four of the six fuel rods were similar to GE4 or GE5 design rods, except for fuel length (0.75 m) and plenum volume. Two of the test fuel rods (901-2, and 901-4) were PCI remedy rods. Each fuel rod was surrounded by an individual flow shroud, and four fuel rods and flow shroud assemblies were symmetrically placed within the PBF test train for each OPTRAN 1-1 transient. Two of the fuel rods (901-1 and 901-3) were tested in only the first of the four OPTRAN 1-1 transients, transient OPTRAN 1-1A. These two fuel rods were replaced with test rods 901-5 and 901-6 for the final three transients, OPTRAN 1-1 B, C, and D. Test rods 901-2 and 901-4 were used during all four OPTRAN 1-1 transients.

The nuclear operation in the PBF for the OPTRAN 1-1 test consisted of two extensive fuel conditioning phases and four power transients. The purposes of the fuel conditioning were to measure the ratio of test rod power to PBF core power and to carefully condition the fuel rods to a peak rod power of 27 kW/m, since the test rods had been irradiated at the Monticello BWR core periphery at average rod powers from only 9.9 to 12.7 kW/m. The first OPTRAN 1-1 test transient simulated a BWR turbine trip without steam bypass with the irradiated fuel rods operating above typical BWR core average powers (of 18 kW/m). The peak fuel rod power was increased from 24.3 kW/m to 90.3 kW/m in 0.32 s while maintaining a constant coolant flow rate.

Since two of the test fuel rods were replaced after OPTRAN 1-1 Transient A, a second fuel conditioning operation to a peak rod power of about 30 kW/m was performed. The power history of OPTRAN 1-1 Transient B (30.9 kW/m to 201.5 kW/m in 0.66 s) simulated a BWR generator load rejection transient without steam bypass for fuel rods operating above BWR core-average peak rod powers except that the time duration of the transient was about twice that predicted by GE.

OPTRAN 1-1 transients C and D were performed at progressively higher transient powers

than the GE safety analysis predicted to be possible in an effort to determine failure threshold margins. The peak fuel rod power was increased from 28.9 to 240.5 kW/m in about 0.74 s during Transient C and from 24.4 to 264.0 kW/m in 0.96 s during Transient D. No fuel rod failures occurred during the OPTRAN 1-1 transients.

Many of the anticipated transients may be postulated to occur with a failure of the automatic scram system and are then called anticipated transients without scram (ATWS). The potential for fuel rod damage may be higher for ATWS events than for anticipated transients with scram because dryout and severe cladding temperature excursions up to 1050 K can occur during an ATWS. Thus in addition to the PCI mechanism for cladding failure, cladding oxidation and embrittlement and cladding collapse and waisting (collapse into gaps between the fuel pellets) may occur during an ATWS.

Test OPTRAN 1-2 was performed to evaluate the probability and extent of fuel rod damage for the most severe BWR ATWS that results in boiling transition. Two irradiated fuel rods were tested in tandem with two unirradiated highly enriched fuel rods. The purpose of the unirradiated rod in each set was to provide coolant conditions for the irradiated test fuel rod typical of the coolant conditions existing near the axial flux peak region of a commercial BWR core.

The nuclear operation for Test OPTRAN 1-2 consisted of an extensive fuel rod conditioning phase and a single power transient. The power transient that was performed simulated a main steam isolation valve closure transient without scram at near-typical coolant pressure, quality, and flow rate conditions that are calculated to exist during such an ATWS. The purposes of the fuel conditioning were to measure the ratio of test rod power to core power and to carefully condition the preirradiated fuel rods to a peak power of 29 kW/m. The Monticello BWR irradiation was at an average rod power of 9.2 kW/m for Rod 902-2 and at 7.8 kW/m for Rod 902-4. During the OPTRAN 1-2 transient the peak test rod power was increased from 27 to 294 kW/m, at a maximum ramp rate of 300 kW/m/s. The test rod power was then reduced to 10 kW/m in about 32 s and was held constant at 10 kW/m for the next 1170 s.

The test rod shroud outlet coolant conditions were initially maintained below saturation temperature to obtain a thermal-hydraulic power calibration of the test rod and heater rod powers. Prior to the transient, saturated water conditions at the inlet of the test rods was obtained by decreasing the coolant flow rate. Boiling transition occurred on both OPTRAN 1-2 test rods. No test fuel rod failures occurred during the OPTRAN 1-2 transient.

It is important to note that, based on the results of ORIGEN2 calculations, the iodine inventory in the test fuel rods at the time of the OPTRAN transients was very nearly the same as it was at the end of the Monticello irradiation.

Posttest analyses of the behavior of the OPTRAN 1-1 and OPTRAN 1-2 fuel rods were performed to gain insight into the timing and magnitude of the measured fuel rod elongation and their relationship with respect to PCI and possible PCI cracking of the cladding. The analyses of the OPTRAN 1-1 and 1-2 fuel rods were performed in two parts. The steady-state fuel rod analysis computer code FRAPCON-2 was used in the first part to calculate fuel rod behavior during the irradiation in the Monticello reactor and the preconditioning in PBF. Then, the transient fuel rod analysis code FRAP-T6 was used to calculate the behavior of the fuel rods during the transients. Computer code calculations of the test fuel rod elongations during the four OPTRAN 1-1 transients, and calculations of both the fuel rod elongations and cladding surface temperatures for the OPTRAN 1-2 transients were in very good agreement with the measurements.

The posttest calculations indicate that the test fuel rod initial conditions established by the steady-state irradiation and preconditioning play important roles in fuel rod behavior during transients. The steady-state irradiation of the fuel rods in the Monticello Reactor was performed at low power and, therefore, the fuel experienced a small amount of swelling. In addition, the amount of fission products accumulated on the grain boundaries was small. The fuel experienced additional densification during preconditioning because the fuel temperatures during preconditioning were higher than during the steady-state operation. The total densification was calculated to be larger than the swelling experienced by the fuel. Also, the cladding was calculated to experience very little creepdown during the steady-state irradiation. Therefore, at the end of the steady-state irradiation and preconditioning, the gap between the cladding and fuel was calculated to be larger than the as-fabricated gap. The fuel-to-cladding gap just prior to the transient was calculated to be larger for the OPTRAN 1-2 fuel rods than for the OPTRAN 1-1 fuel rods because

the OPTRAN 1-2 fuel rods experienced a smaller amount of swelling. Thus, even though the peak rod powers reached during the OPTRAN 1-2 transient were higher than for OPTRAN 1-1 Transient D, the calculated cladding hoop stress was higher for OPTRAN 1-1 Transient D than for OPTRAN 1-2. Based solely on calculated stresses, the test rods used in OPTRAN 1-1 would be more likely to develop PCI cracks than the test rods used in OPTRAN 1-2.

The calculations indicate that Rod 901-1 did not experience any radial PCI. The hoop stresses in Rod 901-1 were due to differential pressure and the maximum calculated hoop stress was equal to -54.6 MPa. Rod 901-6 was calculated to experience increasingly harder radial PCI during transients B, C, and D. It experienced the maximum calculated hoop stress of 188.0 MPa during transient D. Rod 902-4 experienced a maximum calculated hoop stress of 110.2 MPa. The calculated permanent hoop strains remained negative for all the test rods. Because Rod 901-6 experienced the maximum hoop stress of 188.0 MPa for less than 1.0 s, it was unlikely to have any PCI cracks developed in this rod.

The peak hoop stress values for OPTRAN 1-1 Transient D and OPTRAN 1-2, while seemingly low, are difficult to place in proper perspective. Had the OPTRAN rods been irradiated at significantly higher powers in Monticello, fuel swelling (and possibly cladding creepdown) would have occurred to a larger extent. The fuel-to-cladding gap sizes would have been smaller going into the OPTRAN transients, so cladding hoop stresses would have been larger during the transients. Accordingly, it is recommended that FRAPCON-2/FRAP-T6 calculations be repeated for core-average and peak-power BWR rods so that quantitative estimates of the low base-power influences can be made.

Even then, predictions on PCI crack formation for higher power rods could not be made without comparisons to hoop stresses in situations where PCI cracks did form. The Studsvik Demo-Ramp II and Trans-Ramp I projects were performed on representative BWR rods and did induce incipient cracks from higher power irradiations of less than a one-minute duration. FRAPCON-2/FRAP-T6 calculations should also be performed for an appropriate subset of these rods. It is likely that FRAP-calculated hoop stress values during the Studsvik experiments would be much larger than FRAP-calculated stresses for a peak-power BWR rod during OPTRAN 1-1 and 1-2. If so, a strong conclusion could be made that fuel rods would not fail from PCI during similar commercial transients. Alternatively, if peak hoop stresses were found to be approximately equivalent, further assessments of transient fission product releases during both situations by a code like FASTGRASS would be required.

The posttest calculations indicate that only small amounts of fission products accumulated at grain boundaries at the end of the steady-state operation and preconditioning. The low fission product accumulation at grain boundaries resulted because the time-weighted average rod powers at the Monticello core periphery ranged between only 7.8 and 12.7 kW/m, compared with a BWR 8 x 8 core-average rod power of 18 kW/m. Peak centerline fuel temperatures were calculated to be between 900 and 1200 K during the Monticello irradiation, compared with core-average commercial maximum temperatures between 1400 and 1600 K. The lower OPTRAN fuel temperatures led to slower diffusion of fission products within UO_2 grains and prevented appreciable gas bubble accumulation at fuel grain boundaries. Formation of connected porosity and interlinked bubbles at grain faces was also inhibited. Thus, there was little possibility of a burst-type release of corrosive fission products upon pellet expansion and microcracking during the OPTRAN power transients. Commercial fuel rods operated at or above average core powers would be expected to release considerably larger portions of their gaseous inventories under comparable circumstances. The differences in fuel temperatures and prospective gas releases could be quite important in exceeding an iodine concentration threshold for stress-corrosion cracking during the OPTRAN tests.

Because no test rods failed and because test rod instrumentation was limited by the necessity of preserving internal chemistries, the majority of the test fuel rod damage information had to be provided by postirradiation examinations (PIE). The hot cell techniques used for the PIE included pulsed-eddy-current (PEC) scanning for cladding cracks and rod diameter changes, gross and spectral gamma scans for fission product distribution, composition analyses on extracted gap/plenum gases, fuel burnup measurements, flattening of cladding clamshell segments to expose any incipient cracks, fractographic investigations by scanning electron microscope, and determinations of cladding deformation and phase transformations by metallography.

Results of pretest visual examination of the OPTRAN fuel rods indicated no signs of exposure to a severe power excursion except that the two test

rods from OPTRAN 1-2 were bowed over most of their 75-cm fueled length. (The two fresh heater rods were failed as expected). The PEC investigations, which have a detection threshold for cladding cracks that are <10% of the 0.86-mm wall thickness, indicated no incipient cracks propagating from interior cladding surfaces on the seven OPTRAN rods scanned. No permanent hoop strains (ridges) at pellet length intervals were observed and the OPTRAN 1-2 rod PEC scans indicated that waisting of ductile cladding into interfacial gaps did not occur.

The normalized gamma activity measurements indicate that no axial migration of cesium or iodine occurred as a consequence of the OPTRAN power spikes. However, transient release and radial redistribution of fission products cannot be discounted. The iodine inventory in the test fuel rods at the initiation of the OPTRAN transients was very nearly the same as it was at the end of the Monticello irradiation. Iodine freed from the UO_2 lattice could have reached and reacted with the cladding without moving along the rods.

Gases occupying the gap/plenum regions of each OPTRAN fuel rod were withdrawn for composition and volumetric analyses. Results from the rod plenum gas analysis were as expected, with the rods undergoing the mildest OPTRAN 1-1 transient indicating the lowest fission gas release and the rods undergoing the OPTRAN 1-2 transient indicating the highest fission gas release. OPTRAN 1-2 had a higher fission gas release than OPTRAN 1-1 Transient D because the fuel centerline temperature was considerably higher for OPTRAN 1-2 than OPTRAN 1-1D (calculated values of 2070 K compared with 1789 K). The measured fission gas release percentage measured for the OPTRAN tests cannot be applied to typical commercial fuel rods undergoing similar transients because the base irradiation powers of the OPTRAN fuel rods were much lower than commercial average rod powers. Consequently, commercial fuel rods operated at or above core average powers could be expected to release considerably larger portions of their gaseous inventories under comparable transient circumstances.

Cladding clamshell investigations were focused on searching for and characterizing incipient cladding cracks. About 60% of the cladding length was examined on each OPTRAN fuel rod. Three clamshell sections were extracted from each OPTRAN rod. This investigation revealed only one isolated defect that could be classified as an incipient crack. The defect was found on Rod 902-4, an OPTRAN 1-2 rod. The defect was longer than typical PCI-induced cladding perforations and it demonstrated a mixture of ductile and brittle fracture nodes. Despite these discrepancies, PCI and stress-corrosion cracking cannot be completely disregarded as potential causes for the observed defect. However, because higher cladding hoop stresses were calculated for the OPTRAN 1-1 Transient D, than for OPTRAN 1-2, PCI cracks would have been more likely to occur on Rod 901-6. This suggests that the incipient crack found on Rod 902-4 may have been a fabrication defect.

Metallographic examinations show that during the dryout phase of the OPTRAN 1-2 test cladding material was transformed to beta-zircaloy and, therefore, cladding temperatures in excess of 1234 K were obtained. This is considerably higher than the maximum calculated cladding surface temperature of 1007 K.

The results of the OPTRAN 1-1 and 1-2 experiments are very encouraging. No fuel rod cladding failures occurred and only one isolated defect that could be classified as an incipient crack could be found. For fuel rods with average powers during irradiation up to 12.7 kW/m it can be concluded that for anticipated transients, represented by the OPTRAN 1-1 and OPTRAN 1-2 tests, fuel rod damage will probably not occur. Unfortunately, conclusions cannot be reached regarding anticipated transients nor anticipated transients without scram in general because of the low average irradiation power in Monticello for the OPTRAN 1-1 and OPTRAN 1-2 test fuel rods and because of the prior statistics for these experiments (only eight fuel rods were tested). However, GE is of the opinion that fuel rod failures caused by PCI are just as likely to occur if the rods have not been operated at high power. GE claims that this was recently confirmed during the Super Ramp Program where fuel rods that had a peak base irradiation power of 27 kW/m failed at about the same ramp power levels as fuel which had a peak base irradiation power of 17.7 kW/m.

Clearly, the issue of PCI cladding failures during anticipated transients can only be totally resolved by additional OPTRAN-type tests using high-burnup test rods irradiated at BWR core-average and peak powers.

CONTENTS

ABSTRACT i

EXECUTIVE SUMMARY iii

INTRODUCTION 1

EXPERIMENT CONFIGURATION 3

OPTRAN 1-1 Fuel Assembly 3

OPTRAN 1-2 Fuel Assembly 3

OPTRAN 1-1 Test Train and Instrumentation 3

OPTRAN 1-2 Test Train and Instrumentation 3

TEST CONDUCT AND TIME DEPENDENT MEASUREMENTS 7

OPTRAN 1-1 Test Conduct 7

OPTRAN 1-1 Time Dependent Results 9

OPTRAN 1-2 Test Conduct 12

OPTRAN 1-2 Test Results 14

POSTTEST ANALYSIS 16

FRAPCON-2 Calculations for Steady State Irradiation and Preconditioning 16

FRAP-T6 Calculations for Rod 901-1 19
FRAP-T6 Calculations for Rod 901-6 21
Transient B 21
Transient C 27
Transient D 27
FRAP-T6 Calculations for Rod 902-4 31

Discussion of Calculated Results 34

POSTIRRADIATION EXAMINATION RESULTS 35

Visual Inspections 35

Pulsed-Eddy-Current Investigations 35

Gamma Scans 37

Rod Gas Determinations 39

Burnup Measurements 41

Cladding Clamshell Investigations 41

Scanning Electron Fractography 45

Metallographic Findings 53

DISCUSSION 55

CONCLUSIONS 58

REFERENCES 59

(The appendixes are on microfiche attached to the inside back cover of this report.)

APPENDIX A—TEST DESIGN AND CONFIGURATION FOR OPTRAN 1-1 AND OPTRAN 1-2 ..... A-1

APPENDIX B—TEST CONDITIONS AND CONDUCT B-1

APPENDIX C—OPERATIONAL TRANSIENT TEST SERIES OPTRAN 1-1 AND OPTRAN 1-2 DATA QUALIFICATION, UNCERTAINTIES, AND DATA PLOTS C-1

APPENDIX D—PRETEST CHARACTERIZATION OF GE SEGMENTED FUEL RODS D-1

APPENDIX E—POSTIRRADIATION EXAMINATIONS E-1

APPENDIX F—OPTRAN 1-1 AND OPTRAN 1-2 TESTS DOCUMENT AND RECORDS TRACEABILITY F-1

APPENDIX G—COMPUTER MODELS AND INPUT G-1

FIGURES

1. Cross-sectional view of OPTRAN 1-1 test assembly 4

2. Cross-sectional view of OPTRAN 1-2 test assembly 5

3. Schematic of OPTRAN 1-2 fuel rod shroud pairs 6

4. OPTRAN 1-1 fuel rod power history 8

5. Comparison of specified and measured peak rod power pulse during OPTRAN 1-1D 9

6. OPTRAN 1-1 peak fuel rod transient power 10

7. Cladding elongation Rod 901-1 during OPTRAN 1-1A transient 10

8. Cladding elongation Rod 901-6 during OPTRAN 1-1B transient 11

9. Cladding elongation Rod 901-6 during OPTRAN 1-1C transient 11

10. Cladding elongation Rod 901-6 during OPTRAN 1-1D transient 12

11. OPTRAN 1-2 fuel rod power history 13

12. Test rod peak power during OPTRAN 1-2 transient 14

13. Cladding elongation Rod 902-4 during OPTRAN 1-2 transient 15

14. Cladding temperature Rod 902-4 at 70 mm above midplane 15

15. Axial power distribution during steady-state irradiation; Rods (a) 901-1 and 901-6, (b) 902-4 17

16. Axial power distribution during preconditioning; Rods 901-1 and 901-6 18

17. Radial power profiles for unirradiated and irradiated fuel pellets, Rod 901-1 OPTRAN 1-1 22

18. Calculated average and peak fuel temperatures, Rod 901-1 during OPTRAN 1-1A 22

19. Comparison of measured and calculated cladding elongation with fuel rod power, Rod 901-1 during OPTRAN 1-1A 23

20. Calculated average and peak fuel temperatures, Rod 901-6 during OPTRAN 1-1B 25

21. Comparison of measured and calculated cladding elongation with fuel rod power, Rod 901-6 during OPTRAN 1-1B 25

22. Calculated maximum cladding hoop strains versus time, Rod 901-6 during OPTRAN 1-1B 26

23. Calculated average and peak fuel temperatures, Rod 901-6 during OPTRAN 1-1C 28

24. Comparison of measured and calculated cladding elongation with fuel rod power, Rod 901-6 during OPTRAN 1-1C 28

25. Calculated maximum cladding hoop strain versus time, Rod 901-6 during OPTRAN 1-1 29

26. Calculated average and peak fuel temperatures, Rod 901-6 during OPTRAN 1-1D 29

27. Comparison of measured and calculated cladding elongation with fuel rod power, Rod 901-6 during OPTRAN 1-1D 30

28. Calculated maximum cladding hoop strain versus time, Rod 901-6 during OPTRAN 1-1D 30

29. Calculated average and peak fuel temperatures and rod power for Rod 902-4, during OPTRAN 1-2 32

30. Comparison of measured and calculated cladding temperatures, Rod 902-4 during OPTRAN 1-2 32

31. Comparison of measured and calculated cladding elongation with peak rod power, Rod 902-4 during OPTRAN 1-2 33

32. Calculated maximum cladding hoop strains versus time, Rod 902-4 during OPTRAN 1-2 33

33. Bowing on OPTRAN 1-2 Rod 902-2, as viewed from the 0-degree (top) and 130-degree orientations 36

34. Bowing on OPTRAN 1-2 Rod 902-4, as viewed from the 315-degree (top) and 180-degree orientations 36

35. Normalized iodine distributions within OPTRAN 1-1 fuel rods 38

36. Normalized ^{137}Cs (30-year half-life) distributions within OPTRAN fuel rods 38

37. Normalized ^{134}Cs (two-year half-life) distributions within OPTRAN rods 39

38. Confirmation of GE burnup estimations by OPTRAN sample measurements 42

39. OPTRAN test rod configuration and sectioning locations on individual fuel rods 43

40. Preflattening appearances of interior cladding surfaces on representative clamshell specimens 44

41. Interior cladding surface anomalies exposed by flattening clamshell samples 46

42. Fracture surface after extension through punched Specimen C-8 (above) and after bottom half was mounted on an SEM stub 47

43. SEM fractography of Sample C-8 from OPTRAN 1-1 Rod 901-4 49

44. SEM investigations of the incipient crack found in Clamshell C-20 from OPTRAN 1-2 Rod 902-4 50

45. Cladding microstructures near the lower boiling transition boundary on OPTRAN 1-2 Rod 902-4 51

46. Cladding phase transformations from boiling transition and a possible crack nucleation site on Area 4 of Mount T-2194 52

A-1. PBF reactor A-4

A-2. PBF reactor core A-5

A-3. PBF in-pile tube cross-section A-7

A-4. Cross-sectional view of test assembly in OPTRAN 1-1 ..... A-10

A-5. Schematic of fuel rod shroud pair in OPTRAN 1-2 ..... A-12

A-6. Cross-sectional view of OPTRAN 1-2 test assembly A-13

B-1. OPTRAN 1-1 fuel rod power history B-6

B-2. OPTRAN 1-1 fuel rod power history B-7

B-3. OPTRAN 1-1 fuel rod power history B-8

B-4. Figure of merit versus control rod position OPTRAN 1-1 fuel conditioning B-9

B-5. OPTRAN 1-1 fuel rod transient power B-11

B-6. Peak to average fuel rod power from OPTRAN 1-1 flux wires B-15

B-7. OPTRAN 1-2 test operation rod history B-21

B-8. Figure of merit versus control rod positions for OPTRAN 1-2 ..... B-24

B-9. Test rod peak power versus time during OPTRAN 1-2 transient B-27
B-10. Peak-to-average fuel rod power from OPTRAN 1-2 flux wires B-27

D-1. A schematic of the GE BWR/6 segmented fuel rod D-8

D-2. Rods DTB-2707, 9C07-1 and 0D07-2 0-degree orientation D-41

D-3. Rods PC08-4, 5D05-5, and DTB-2608 0-degree orientation D-42

D-4. Rods STR-134, DTB-2406, DTB-2810, and W5-2 0-degree orientation D-43

D-5. Rods 8D25-3, STR-137, and 0R06-1 0-degree orientation D-44

D-6. Gross gamma scan of GE segmented Rod DTB-2406, cps range 5 x 10^3 ..... D-45

D-7. Gross gamma scan of GE segmented Rod DTB-2810, cps range 5 x 10^3 ..... D-45

D-8. Gross gamma scan of GE segmented Rod 0D07-2, cps range 5 x 10^3 ..... D-46

D-9. Gross gamma scan of GE segmented Rod 0D07-4, at 0 degrees, cps range 1 x 10^3 ..... D-46

D-10. Gross gamma scan of GE segmented Rod 5D05-5, at 0 degrees, cps range 2 x 10^3 ..... D-47

D-11. Gross gamma scan of GE segmented Rod 9D07-2, at 0 degrees, cps range 5 x 10^3 ..... D-47

D-12. Gross gamma scan of GE segmented Rod 0A06-1, cps range 5 x 10^3 ..... D-48

D-13. Gross gamma scan of GE segmented Rod 0A06-4, at 0 degrees, cps range 5 x 10^2 ..... D-48

D-14. Neutron radiograph of GE segmented fuel D-51

D-15. Neutron radiograph of GE segmented fuel D-52

D-16. Neutron radiograph of GE segmented fuel D-53

D-17. Pulsed-eddy-current scans of Rods DTC-1411, DTC-0604, DTC-2707, and 0C08-4 ..... D-54

D-18. Pulsed-eddy-current scans of Rods XZ00403 and DTB-2406 ..... D-55

D-19. Pulsed-eddy-current scans of Rods 9C07-1, STR-073, STR-074, and STR-077 ..... D-56

D-20. Pulsed-eddy-current scans of calibration standard and Rods STR-134, STR-137, and W5-2 ..... D-57

D-21. Pulsed-eddy-current scans of Rods 9D07-2, DTC-2108, DTC-1105, and DTC-1106 ..... D-58

D-22. Pulsed-eddy-current scans of Rods 5A08-2, 5A08-3, 5A08-4, and 8D15-3 ..... D-59

D-23. Pulsed-eddy-current scans of Rods 8D07-2, 9D03-3, 9DO3-4 and 9D01-4 ..... D-60

D-24. Pulsed-eddy-current scans of Rods 5D05-5, 0A06-4, 0A06-1, and 0D06-4 ..... D-61

D-25. Pulsed-eddy-current scans of Rods 0D06-2, 0D07-2, 0D07-3, and 0D07-4 ..... D-62

D-26. Pulsed-eddy-current scans of Rods DTB-2707, DTB-2608, and DTB-2810 ..... D-63

D-27. Photomicrograph of Rod 0D07-3, Section T-2151, 6X D-72

D-28. Photomicrograph of Rod 0D07-3, Section T-2151, 100 and 500X D-73

E-1. Posttest appearance of OPTRAN 1-1 Rod 901-1 at the 0-degree (top) and 180-degree (bottom) orientations E-4

E-2. Posttest appearance of OPTRAN 1-1 Rod 901-2 at the 0-degree (top) and 180-degree (bottom) orientations E-4

E-3. Posttest appearance of OPTRAN 1-1 Rod 901-3 at the 0-degree (top) and 180-degree (bottom) orientations E-5

E-4. Posttest appearance of OPTRAN 1-1 Rod 901-4 at the 0-degree (top) and 180-degree (bottom) orientations E-5

E-5. Posttest appearance of OPTRAN 1-1 Rod 901-5 at the 0-degree (top) and 180-degree (bottom) orientations E-6

E-6. Posttest appearance of OPTRAN 1-1 Rod 901-6 at the 0-degree (top) and 180-degree (bottom) orientations E-6

E-7. Posttest appearance of OPTRAN 1-2 Rod 902-2 at the 0-degree (top) and 130-degree (bottom) orientations E-7

E-8. Posttest appearance of OPTRAN 1-2 Rod 902-4 at the 315-degree (top) and 180-degree (bottom) orientation E-9

E-9. Posttest gross gamma scans from OPTRAN 1-1 Rods 901-1 (top) and 901-2 (bottom) E-12

E-10. Posttest gross gamma scans from OPTRAN 1-1 Rods 901-7 and 901-4 (bottom) E-13

E-11. Posttest gross gamma scans from OPTRAN 1-1 Rods 901-5 (top) and 901-6 (bottom) E-14

E-12. Posttest gross gamma scans from OPTRAN 1-2 Rods 902-2 (top) and 902-4 (bottom) E-15

E-13. Measured ^{131}I profiles along OPTRAN 1-1 rods E-17

E-14. Measured ^{137}Cs profiles along OPTRAN 1-1 fuel rods E-17

E-15. Axially normalized ^{131}I distributions within OPTRAN 1-1 fuel rods E-18

E-16. Axially normalized ^{137}Cs distributions within OPTRAN 1-1 fuel rods E-18

E-17. Axially normalized ^{134}Cs distributions within OPTRAN 1-1 rods E-20

E-18. OPTRAN sample burnup measurements versus GE local burnup estimates E-25

E-19. OPTRAN test rod configuration and sectioning locations on individual fuel rods E-27

E-20. Posttest appearances of interior cladding surfaces from several OPTRAN fuel rods before flattening clamshell specimens E-28

E-21. Interior cladding surface anomalies exposed by flattening clamshell specimens E-30

E-22. Fracture surface after extension through punched specimen C-8 (above) and after bottom half was mounted on an SEM stub E-33

E-23. SEM configuration that optically reflective features found after flattening Clamshells C-5 and C-9 were shallow surface gouges rather than incipient cracks E-34

E-24. SEM investigations of fracture surface morphology on the incipient cladding defect found after flattening Clamshell C-8 from OPTRAN 1-1, Rod 901-4 ..... E-36

E-25. SEM fractography on the incipient cladding crack in Clamshell C-20 from OPTRAN 1-2, Rod 902-4 ..... E-37

E-26. Metallographic investigation of exterior cladding surface marks on Mount T-2175 from OPTRAN 1-1, Rod 901-3 ..... E-41

E-27. Metallographic examination of exterior cladding surface marks on Mount T-2176 from OPTRAN 1-1, Rod 901-3 ..... E-42

E-28. Metallography of mating half to C-20 SEM specimen E-44

E-29. Polarized-light metallography of etched cladding microstructures near the lower boiling transition boundary on OPTRAN 1-2, Rod 902-4 ..... E-46

E-30. Metallography of Area 4 on Mount T-2194 from Rod 902-4, illustrating cladding phase transformations from boiling transition and a possible crack nucleation site E-47

G-1. Analytical model configurations and test rod power profiles used for OPTRAN 1-1 and OPTRAN 1-2 FRAP-T calculations G-4

TABLES

1. Power levels and burnups during steady-state irradiation and preconditioning for Rods 901-1, 901-6, and 902-4 17

2. Densification, swelling, and local burnups for Rod 901-1 18

3. Densification, swelling, and local burnups for Rod 901-6 19

4. Densification, swelling, and local burnups for Rod 902-4 20

5. Values of variable DIFGAP for the transient analysis of Rod 901-1 20

6. Summary of FRAP-T6 results for OPTRAN transient tests 24

7. Rod gas analysis results 40

8. OPTRAN base power/temperature histories 40

A-1. OPTRAN 1-1 fuel rods A-9

A-2. Test OPTRAN 1-1 fuel rod design characteristics A-9

A-3. Test OPTRAN 1-2 fuel rod designations and burnups A-10

A-4. Test OPTRAN 1-2 fuel rod design characteristics A-11

A-5. Instrumentation for test OPTRAN 1-1 test train support structure A-16

A-6. Test OPTRAN 1-1 instrument identification, data channel recording, and display requirements A-20

A-7. Test OPTRAN 1-2 fuel rod and shroud instrumentation A-25

A-8. Test OPTRAN 1-2 test train assembly instrumentation A-27

A-9. Test OPTRAN 1-2 instrument identification, data channel recording, and display requirements A-33

B-1. Peak rod power from reactor core ion chambers B-18

B-2. Calculated peak and radially averaged fuel enthalpies in OPTRAN 1-1 ..... B-18

B-3. Comparison of corrected predicted and measured figure of merit in OPTRAN 1-1 and OPTRAN 1-2 tests B-20

D-1. Geometry and fuel type of GE segmented fuel rods D-4

D-2. Mechanical properties of GE segmented fuel rods D-6

D-3. Fabrication data D-8

D-4. Initial enrichment of the GE segmented fuel rods D-9

D-5. Bundle MTB001 power history (SRP II) D-10

D-6. Bundle MSB125 power history (SRP III) D-13

D-7. Fuel rod, bundle locations, and burnup history D-14

D-8. Fuel rod segment power history—W5-2 ..... D-16

D-9. Fuel rod segment power history—9D03-4 and 9D03-3 ..... D-17

D-10. Fuel rod segment power history—0C08-4 and 9C07-1 ..... D-18

D-11. Fuel rod segment power history—DTB-2810 ..... D-19

D-12. Fuel rod segment power history—DTB-2608, DTB-2707, and X200403-7 ..... D-19

D-13. Fuel rod segment power history—8D15-3 and DTB-2406 ..... D-20

D-14. Fuel rod segment power history—0D06-2 and 0D06-4 ..... D-21

D-15. Fuel rod segment power history—STR-074 and STR-073 ..... D-22

D-16. Fuel rod segment power history—STR-077 ..... D-23

D-17. Fuel rod segment power history—8D07-2 ..... D-24

D-18. Fuel rod segment power history—0D07-4 and 0D07-2 ..... D-25

D-19. Fuel rod segment power history—0D07-3 and 5D05-5 ..... D-26

D-20. Fuel rod segment power history—5A08-1, 5A08-2, 5A08-3, and 5A08-4 ..... D-27

D-21. Fuel rod segment power history—0A06-4 and 0A06-1 ..... D-29

D-22. Fuel rod segment power history—9D01-4 and 9D07-2 ..... D-30

D-23. Fuel rod segment power history—STR-137 and STR-134 ..... D-32

D-24. Pretest enrichment for GE segmented fuel rods D-33

D-25. Rod W5-2 visual examination D-35

D-26. Rod 8D15-3 visual examination D-36

D-27. Rod 0C08-4 visual examination D-37

D-28. Rod STR-134 visual examination D-38

D-29. Rod 9C07-1 visual examination D-38

D-30. Rod DTB-2707 visual examination D-39

D-31. Rod DTB-2608 visual examination D-39

D-32. Rod STR-137 visual examination D-40

D-33. Rod 9D07-2 diametral measurements D-65

D-34. Rod 0D07-2 diametral measurements D-66

D-35. Rod 0007-4 diametral measurements D-67

D-36. Rod 0A06-1 diametral measurements D-68

D-37. Rod 0A06-4 diametral measurements D-69

D-38. Rod 5D05-5 diametral measurements D-70

D-39. Rod DTB-2810 diametral measurements D-71

D-40. Rod DTB-2406 diametral measurements D-72

E-1. OPTRAN rod gas results E-21

E-2. OPTRAN burnup results E-25

G-1. Input used for analysis on test data from OPTRAN 1-1A, Rod 901-1 ..... G-5

G-2. Input used for analysis on test data from OPTRAN 1-1A, B, C, and D G-9

G-3. Input used for analysis on test data from OPTRAN 1-2, Rod 902-4 ..... G-14

EXPERIMENTAL RESULTS OF THE OPERATIONAL TRANSIENT (OPTRAN) TESTS 1-1 AND 1-2 IN THE POWER BURST FACILITY

INTRODUCTION

Anticipated nuclear power reactor transients are deviations from normal plant operating conditions that result from system component malfunctions or reactor operator errors that may occur one or more times during the service life of a reactor and are normally accompanied by a control rod scram. They are distinguished from accidents, which have a much lower probability of occurrence and may result in much more severe consequences. The Electric Power Research Institute (EPRI) has selected 37 categories of anticipated and unanticipated boiling water reactor (BWR) malfunctions and 41 categories of pressurized water reactor (PWR) malfunctions on the basis of transients defined in the United States Nuclear Regulatory Commission (USNRC) assessment of accident risks in U.S. nuclear power plants[1] and data from utilities for transients that have actually occurred.[2] These transients have been assigned a frequency of occurrence per reactor year from 0.02 $\pm$0.14 to 1.41 $\pm$1.89 for BWRs and from 0.01 $\pm$0.09 to 1.69 $\pm$2.44 for PWRs.

The effects of such malfunctions may include a loss of the secondary heat sink, an increase in coolant system pressure, and, in BWRs, void collapse and a brief surge in reactor power. The most severe postulated BWR-5 anticipated transient is a generator load rejection without steam bypass, characterized by a peak transient power spike of up to 495% of rated power for about one second. Dryout and severe cladding temperature excursions are not expected during such transients and, therefore, the damage mechanism of concern is cladding fracture due to pellet-cladding mechanical and chemical interactions (PCI).

The first indication that zircaloy-clad UO_2 rods might be susceptible to failure due to a pellet-cladding interactive mechanism inherent to the fuel and cladding materials was obtained in 1964 by the General Electric Company (GE) in the "High Performance UO_2 Program," jointly sponsored by the United States Atomic Energy Commission and EURATOM.[3] Since that time, the phenomenon of PCI-induced cladding failure during normal light water reactor operation has received considerable attention throughout the world. Such failures are apparently induced by power increases after a sufficiently high burnup is attained allowing fission product release. There has been a strong incentive to find a remedy for these failures because the present method of prevention is to accept limits on rates of reactor power increase. These limits are expensive due to the lost power output during slow increases, especially for load following operations. Experiments have been performed in the Halden, Studsvik, NRU, GETR, RISO, RCN-Petten, BR-2 and BR-3 reactors.[4-9] Most investigators now accept the view that both the presence of aggressive chemical species and high localized stresses are prerequisites for power-ramp-induced pellet-cladding-interaction failures.[10] However, pellet-cladding-mechanical-interaction failures have also occurred during severe power increases due to high strain-rate tearing of zircaloy cladding.[11]

Severe core power increases are possible during a variety of anticipated transients and yet the most severe postulated anticipated transients have not occurred in commercial reactors. Therefore, the USNRC was uncertain whether light water reactor fuel rods can fail or be damaged during such events. For anticipated transient conditions, the commonly used fuel failure criteria are overheating criteria; departure from nucleate boiling ratios (DNBR) for PWRs and minimum critical power ratios (MCPR) for BWRs. These overheating criteria may not be appropriate for PCI damage. Therefore, a series of in-pile fuel behavior tests labeled operational transient (OPTRAN) 1-1 were conducted in the Power Burst Facility (PBF) by EG&G Idaho, Inc., for the USNRC to (a) determine the threshold at which light water reactor fuel rods are likely to fail during severe anticipated transients that result in a brief increase in reactor power and (b) identify any fuel and damage mechanisms that may occur. The PBF data, along with other test data, will be used by the USNRC to assess the failure probabilities used in licensee dose calculations for anticipated transients. These results may also impact other questions such as: (a) should a reactor be derated following a

severe anticipated transient, (b) should PCI-damaged fuel be removed following a transient, and (c) should regulations be imposed to limit pellet-cladding interaction in irradiated fuel rods?

Many of the operational transients may be postulated to occur with a failure of the automatic scram system and are then termed anticipated transients without scram (ATWS). The probability of failure of a light water reactor scram system per demand is in dispute, but the likely range is from 10^{-4} to 10^{-6} per scram. The range of probabilities for the occurrence of an ATWS based on an anticipated transient with a probability of occurrence of once per reactor year is 10^{-4} to 10^{-6} per reactor year. ATWS events were elevated in status with the publication of NUREG-0460, Volumes I and II in 1978. This report reviewed available information on the subject and incorporated analyses performed by the vendors. A later volume of the report suggested that resolution of the ATWS concern should rest on engineering evaluation and judgment of the appropriateness of alternative plant modifications, rather than quantitative risk analyses.

The potential for fuel rod damage is higher for BWR ATWS events than for BWR anticipated tran sients with scram. The most severe BWR ATWS, according to vendor safety analyses[12] would result in reactor power increases up to 745% of the rated power for a short period of time followed by low-magnitude power oscillations for 20 min before the reactor is made subcritical by boron injection. Peak cladding temperatures up to $\simeq$1050 K for $\sim$80 s are predicted. This scenario suggests several fuel rod damage mechanisms: (a) pellet-cladding mechanical interaction (PCI), (b) boiling transition causing cladding oxidation and embrittlement; and (c) cladding collapse and "waisting" (plastic flow of hot, ductile cladding into interpellet gaps on unpressurized rods).

At cladding temperatures in excess of the recrystalization temperature ($\sim$920 K), cladding collapse onto the fuel stack and into fuel pellet interfaces has been observed in previous PBF tests, but cladding collapse has not caused failure. At higher temperatures ($>$1100 K), cladding oxidation of the outer surface due to zircaloy-water reaction and of the inner surface due to zircaloy-UO_2 reaction becomes appreciable. As oxygen diffuses into the inner and outer cladding surface, the zircaloy undergoes a metallurgical phase transformation from the beta phase to ZrO_2 and oxygen-stabilized alpha phase. Only the central beta phase retains the integrity and strength of the cladding wall, due to the brittle nature of the ZrO_2 and oxygen-stabilized alpha-zircaloy layers. Zircaloy oxidation would not be expected to result in cladding failure at the cladding temperatures and durations in boiling transition calculated to occur for even the most severe BWR ATWS.

Test OPTRAN 1-2 was performed to evaluate the probability and extent of fuel rod damage for the most severe BWR ATWS that results in boiling transition. Two irradiated fuel rods were tested in tandem with two unirradiated highly enriched heater rods. The purpose of the unirradiated rod in each set was to provide coolant conditions for the irradiated test fuel rod typical of the coolant conditions existing near the axial flux peak region of a commercial BWR core. Following an extensive fuel conditioning operation, a single power transient was performed that simulated a main steam isolation valve closure transient without scram at near-typical coolant pressure, quality, and flow rate conditions that are calculated to exist during such an ATWS.

EXPERIMENT CONFIGURATION

This section briefly describes the fuel rods used, the fuel rod instrumentation and mounting in the test assemblies, and the test trains used in the OPTRAN 1-1 and OPTRAN 1-2 tests. A detailed discussion of these items can be found in Appendix A.

OPTRAN 1-1 Fuel Assembly

Six fuel rods were tested. All six fuel rods were originally fabricated by GE, and irradiated in the Northern States Power Company's Monticello boiling water reactor (SRP II bundle) to burnups ranging from about 5,000 to 22,000 MWd/m t u . Four of the six fuel rods were similar to GE-4 or GE-5 design rods, except for fuel length (0.75 m) and plenum volume (which was scaled to the fuel length). Two of the fuel rods incorporated design modifications to improve their PCI resistance. Each fuel rod was surrounded by an individual flow shroud, and four fuel rods and shroud assemblies were symmetrically placed within the PBF test train for each transient. Figure 1 is a cross section of the fuel assembly showing the fuel rods and shrouds. Two of the fuel rods (901-1 and 901-3) were tested in only the first of four OPTRAN 1-1 transients, transient OPTRAN 1-1A. These two fuel rods were replaced with replacement rods 901-5 and 901-6, respectively for the final three OPTRAN 1-1 transients.

OPTRAN 1-2 Fuel Assembly

Test OPTRAN 1-2 was conducted with two BWR 8 x 8 fuel rods fabricated by GE and irradiated in the Northern States Power Company's Monticello BWR and two unirradiated 8 x 8 fuel rods fabricated by EG&G Idaho, Inc. The two irradiated fuel rods were of typical GE4 or GE5 design, except for fuel length (0.75 m). The two unirradiated heater fuel rods were enriched to 10 wt% ^{235}U to provide sufficient power to produce the required coolant conditions.

Each fuel rod was surrounded by a coolant flow shroud. The outlets of the heater-rod flow shrouds were connected by tubing to the inlets of the irradiated test rod flow shrouds as shown in Figure 2. A schematic of each pair of fuel rods and the coolant flow path is shown in Figure 3. Remotely operated orifices, installed at the heater rod shroud outlets, provided a means of reducing the coolant flow for the test rods by up to 55% prior to the power transient. The variable orifice design was necessary to obtain the required low flow rates for the test fuel rods, without causing severe failure of the much higher power heater rods prior to the transient.

OPTRAN 1-1 Test Train and Instrumentation

A Battelle Pacific Northwest Laboratory four-rod test train, which positions and supports the four fuel rods in the in-pile tube (IPT), was used for the in-pile OPTRAN 1-1 test series. The IPT flow tube directed the coolant from the IPT inlet down to the lower plenum and up into the fuel rod flow shrouds. Each fuel rod was fixed rigidly to the shroud at the top of the fuel rod and was free to expand axially downward against a linear variable differential transformer (LVDT) that measured the axial growth of each rod. The 0.75-m fuel rods and shrouds were positioned so that the axial midplane of the active fuel stack was at the same elevation as the axial midplane of the PBF driver core fuel rods (0.91 m long). The fuel rods were centered in the shroud with two sets of centering screws located at ± 254 mm from the fuel midplane.

In addition to the LVDTs, instruments were provided to measure coolant conditions, fuel rod power, and fission product release. The test rods were not opened prior to the PBF tests to preserve internal rod chemistries, so they contained no instrumentation. Flux wires, fission chambers, and self-powered neutron detectors (SPNDs) were used for neutron detection while flowmeters and thermocouples measured specific coolant conditions in each flow shroud. Pressures were measured by transducers mounted both inside and outside the IPT head. Figure 1 illustrates some of the instrument locations.

OPTRAN 1-2 Test Train and Instrumentation

A Battelle Pacific Northwest Laboratory four-rod test train was also used for OPTRAN 1-2. The test fuel rods were positioned so that the axial midplane of each active fuel stack was at the same

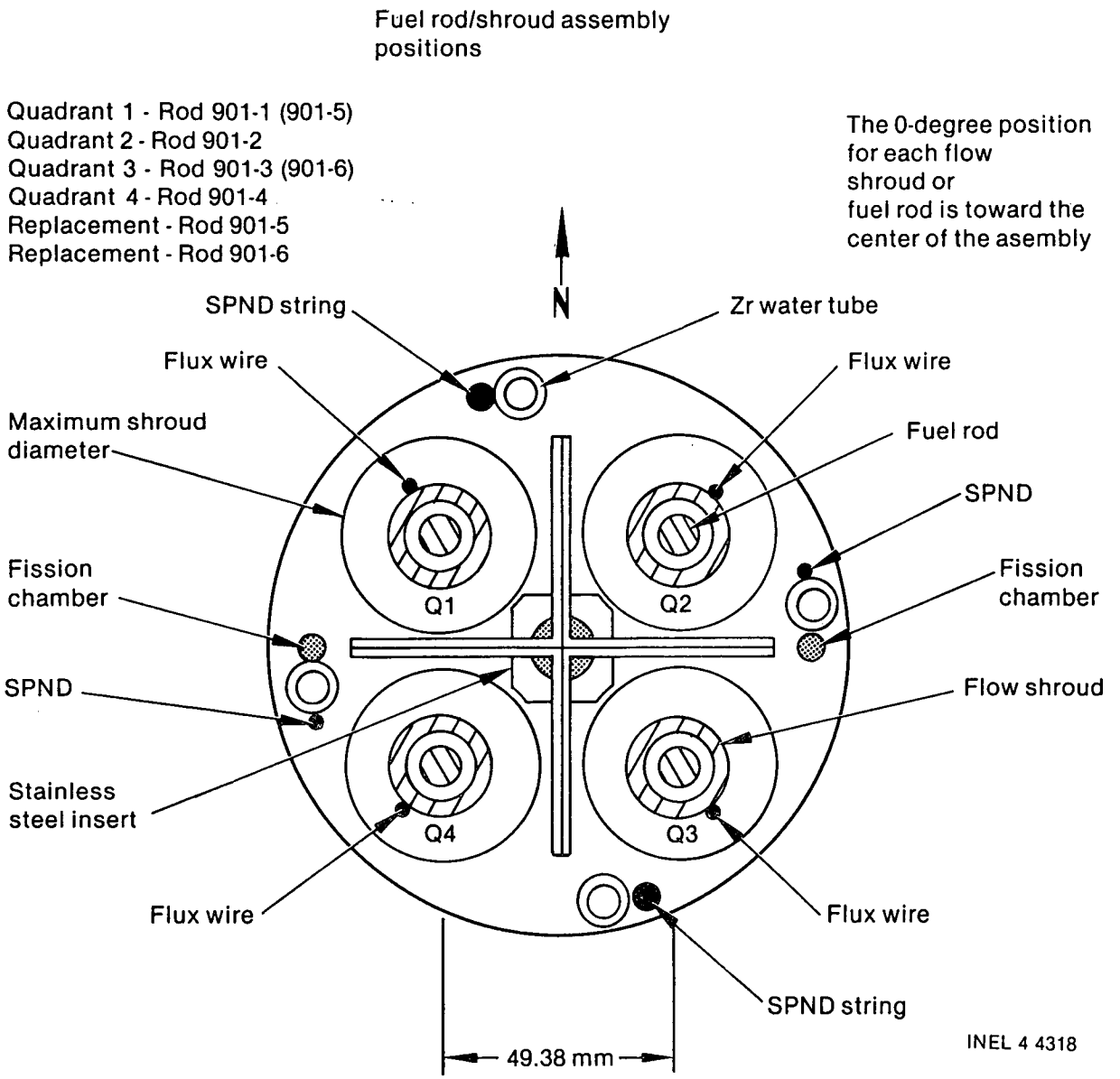

Figure 1. Cross-sectional view of OPTRAN 1-1 test assembly.

elevation as the axial midplane of the PBF core fuel rods (±4 mm) and each rod was centered in each flow shroud. Each fuel rod was fixed rigidly to the shroud at the top and the rod was free to expand axially downward against the fuel rod axial growth measurement transducer. In addition to the LVDTs, instruments were provided to measure coolant conditions, fuel rod power, fission product release, and cladding temperatures. Specifically, the two irradiated fuel rods each had three external cladding thermocouples. Flux wires, fission chamber, and SPNDs were used for neutron detection. Flowmeters and thermocouples measured the coolant conditions in each flow shroud. Pressures were measured with transducers mounted both inside and outside the IPT head. Figure 3 illustrates the location of some of the instruments.

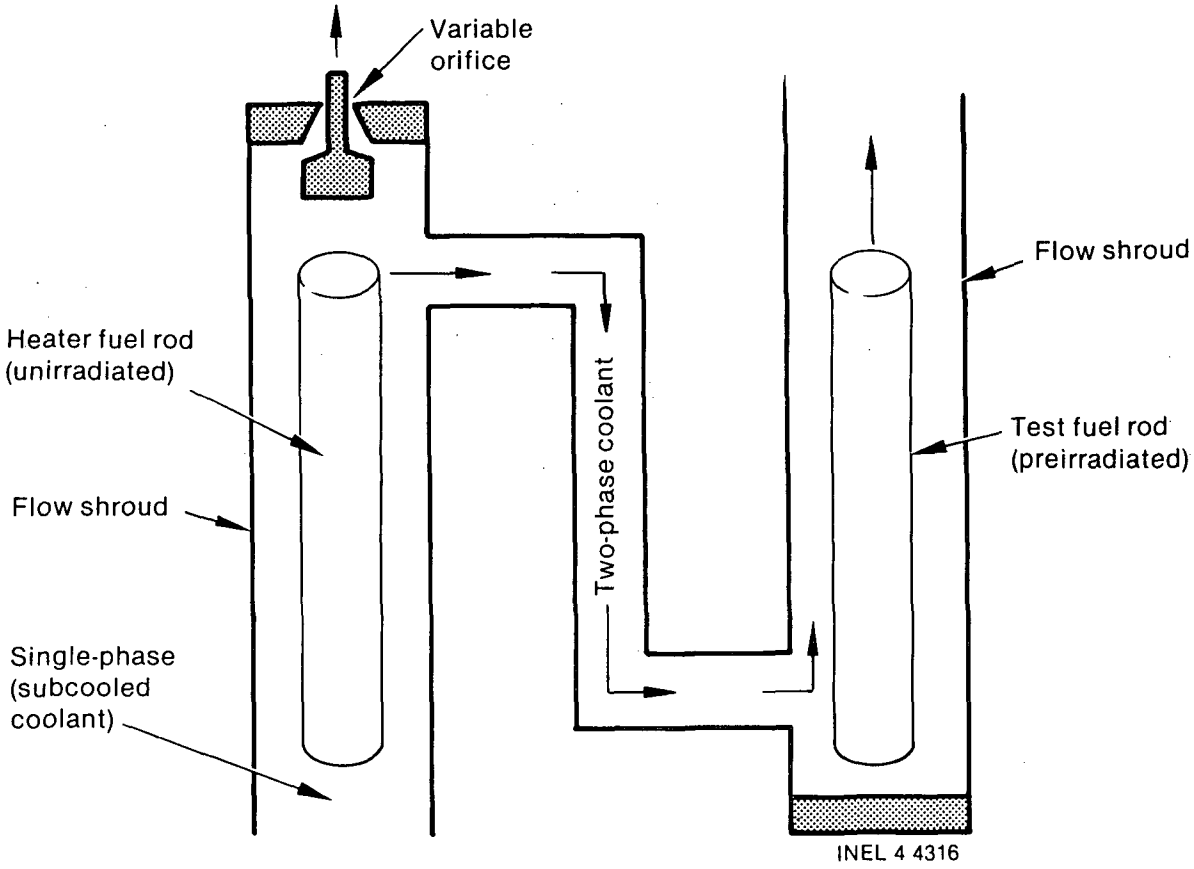

Figure 2. Cross-sectional view of OPTRAN 1-2 test assembly.

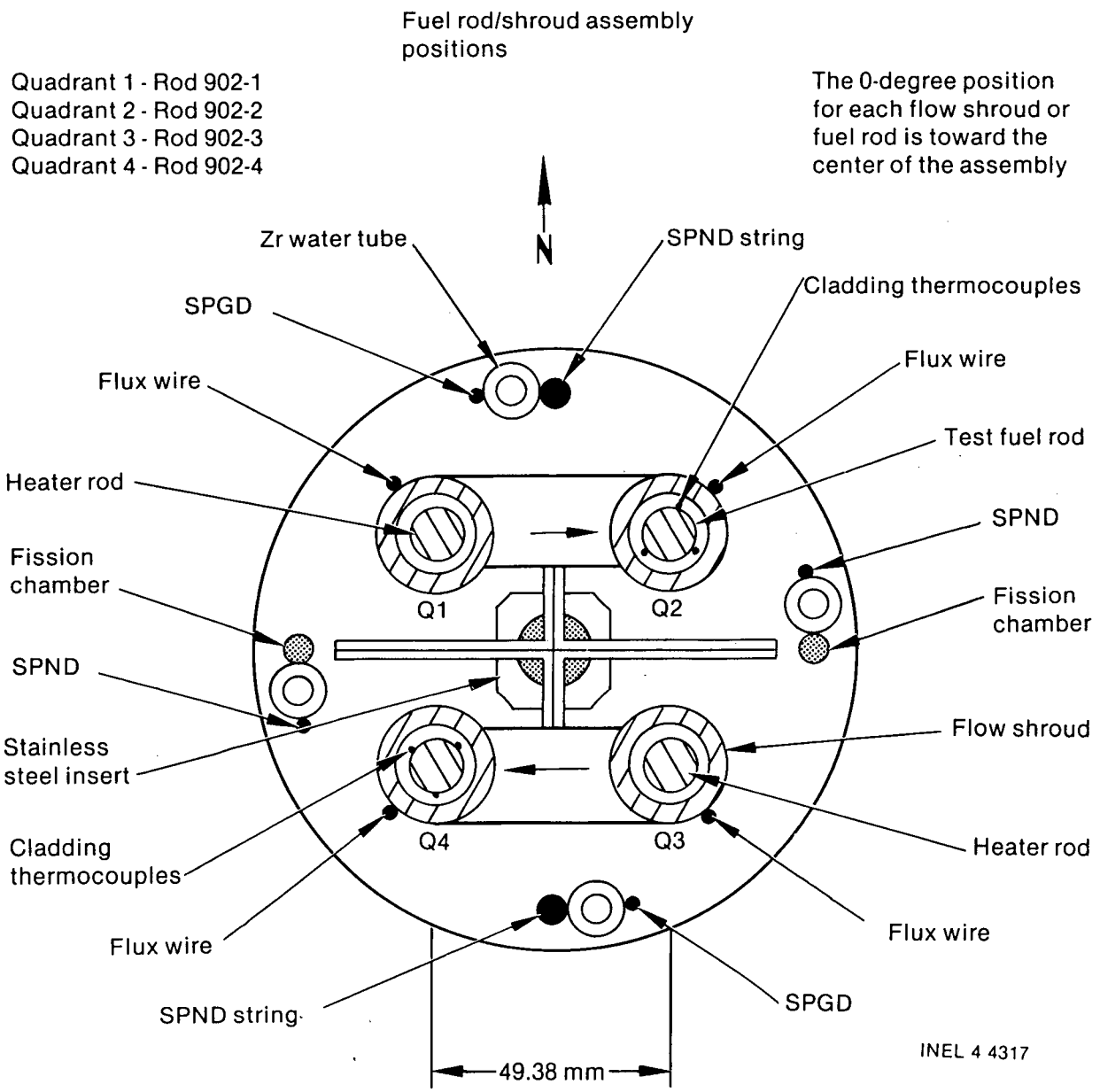

Figure 3. Schematic of OPTRAN 1-2 fuel rod shroud pairs.

TEST CONDUCT AND TIME-DEPENDENT MEASUREMENTS

This section describes the OPTRAN 1-1 and OPTRAN 1-2 tests, including details on the test operating sequence, power levels, and the fuel rod steady-state and transient-power histories. Following the discussion of test conduct is a description of measured time-dependent fuel rod axial growth for each of the OPTRAN 1-1 transients and a discussion of the measured fuel rod axial growth and measured cladding temperature for the OPTRAN 1-2 transient.

OPTRAN 1-1 Test Conduct

The nuclear operation in the PBF consisted of two extensive fuel conditioning phases and four power transients. The purpose of the fuel conditioning was to measure the figure of merit (ratio of test rod power to PBF core power) and to carefully condition the fuel rods to a peak rod power of 27 kW/m, (∿20 kW/m average), since the test rods had been irradiated at the Monticello BWR core periphery at average rod powers of only 9.9 to 12.7 kW/m. Because of safety restrictions, the transient pulse as recorded by reactor power instrumentation had to stay within a prescribed envelope. It was important that an accurate correlation be obtained between core power and test rod power prior to the transients so that test rod power could be automatically adjusted during the power transient. The fuel conditioning consisted of a slow power ramp with single-phase coolant conditions to a rod power of ∿27 kW/m. Maximum rod power ramp rates were held to 0.5 kW/m/min up to 25 kW/m and 0.35 kW/m/h from 25 to 27 kW/m. Each of the two fuel conditioning phases extended over ∿28 h. The first fuel conditioning contained five periods of steady reactor power operation to measure the PBF core thermal power. Figure 4 contains the fuel rod power history during the entire OPTRAN 1-1 test series.

Instruments used to determine fuel rod power during fuel conditioning were: shroud coolant inlet and outlet thermocouples, shroud flowmeters, shroud differential coolant thermocouples, and the system pressure. Details of the calculations are given in Appendix B, Section 2-1. The uncertainty of the rod powers in Figure 4 is ±2.1 kW/m (two sigma).

The first OPTRAN 1-1 test transient simulated a BWR turbine trip without steam bypass with the irradiated fuel rods operating above typical BWR core-average powers (of 18 kW/m). The peak fuel rod power was increased from 24.3 kW/m to 90.3 kW/m in 0.32 s, while maintaining a constant coolant flow rate during the power transient. The PBF was able to almost exactly reproduce the specified power history, as illustrated in Figure 5, which compares the two powers. Following the first transient, the loop was cooled and depressurized, the test train removed from the in-pile tube, and Rods 901-1 and 901-3 with their shrouds were removed and replaced with Rods 901-5 and 901-6 with their shrouds, respectively. Rods 901-1 and 901-3 were removed after the first transient for postirradiation examination so that the cladding could be examined for incipient PCI cracks on the inside surface after just one transient.

The second fuel conditioning was performed to condition the fuel rods to a peak rod power of ∿30 kW/m. The conditioning consisted of a 2-h power ramp to 26 kW/m, a 10-h power ramp to 30 kW/m, and a 12-h hold at 30 kW/m. Single-phase coolant conditions were also maintained during this fuel conditioning phase. The iodine inventory in the test fuel rods at the time of the OPTRAN transients was very nearly the same as it was at the end of the Monticello irradiation. Calculations performed for test rod 901-6 using the single-rod code ORIGEN2 indicate that the total iodine inventory in a test fuel rod operated at 8.39 kW in Monticello for 1101 days would be 0.0651 g. After 1666 days of decay after the Monticello irradiation, followed by the preconditioning between transient OPTRAN 1-1A and OPTRAN 1-1B, the total iodine inventory was 0.0638 g.

The power history of the second transient (30.9 to 201.5 kW/m in 0.66 s) simulated a BWR generator load rejection transient without steam bypass for fuel rods operating above BWR core-average peak rod powers, except that the time duration of the transient was about twice that predicted by GE.

The third and fourth transients were performed at progressively higher transient powers than GE safety analyses predicted to be possible in an effort to determine failure threshold margins. The peak fuel rod power was increased from 28.9 to 240.5 kW/m in about 0.74 s during the third transient and from 24.4 to 264.0 kW/m in 0.96 s during the fourth transient.

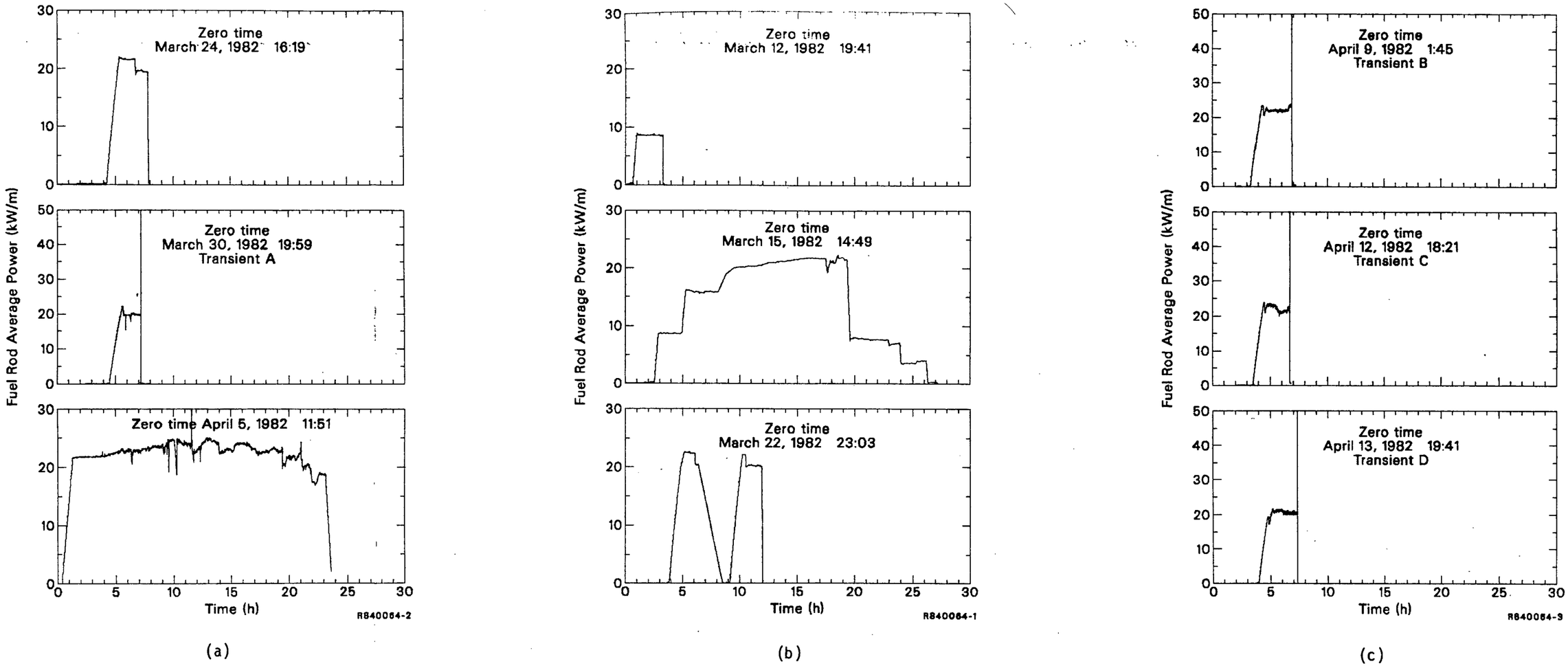

Figure 4. OPTRAN 1-1 fuel rod power history.

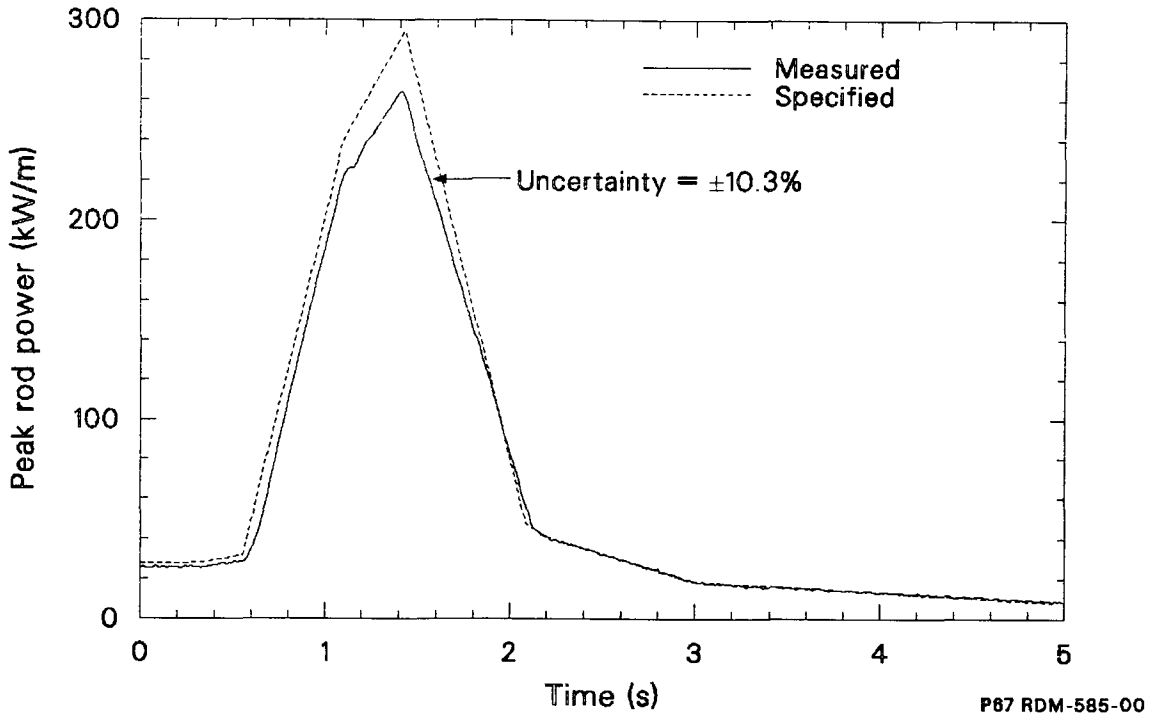

Figure 5. Comparison of specified and measured peak rod power pulse during OPTRAN 1-1D.

The four progressively higher and broader power transients shown in Figure 6 were conducted at power ramp rates as high as 550 kW/m/s. The two sigma uncertainty in the peak valves in Figure 6 are estimated to be 9.5% for A, 13.5% for B, 11% for C, and 10.3% for D. Details of the calculations are given in Appendix B. The power-time histories specified for the first two transients (Transients A and B) approximate the results of a conservative analysis of various BWR-5 anticipated transients performed by GE, using the ODYN computer code. The last transient was conducted at the physical limits of the PBF. Approximately a 2-h hold at steady power preceded each transient. The nominal pretransient coolant temperature, flow rate, and pressure conditions during each transient were 550 K, 525 cm^3/s, and 7.93 MPa, respectively. The fission product detection system registered no indications of rod failure at any time during OPTRAN 1-1.

OPTRAN 1-1 Time Dependent Results

Dryout and severe cladding temperature excursions are not expected during anticipated transients with scram such as those simulated during the OPTRAN 1-1 transient experiments. Therefore, the damage mechanism of primary concern is cladding fracture due to pellet-cladding mechanical and chemical interactions. After the fuel pellets contact the cladding during the transients, the fuel rods begin to increase in length with the fuel pellet stack. For these reasons cladding temperature was not measured during the OPTRAN 1-1 transients and the primary time-dependent measurement was fuel rod axial growth.

The measured axial growth for fuel Rod 901-1 during OPTRAN 1-1 Transient A is shown in Figure 7. Contact between fuel and cladding apparently occurred at 0.68 s when cladding elongation began. By 1.1 s, the fuel rod had grown 0.28 mm in the axial direction, after which the rod began to decrease in length.

The measured axial growth for Rod 901-6 during OPTRAN 1-1 Transient B is shown in Figure 8. Contact between the fuel and cladding apparently occurred at about 0.6 s at which time axial elongation began. The peak cladding growth of 0.64 mm occurred at 1.3 s and then began to decrease.

The measured axial growth for Rod 901-6 during OPTRAN 1-1 Transient C is shown in Figure 9.

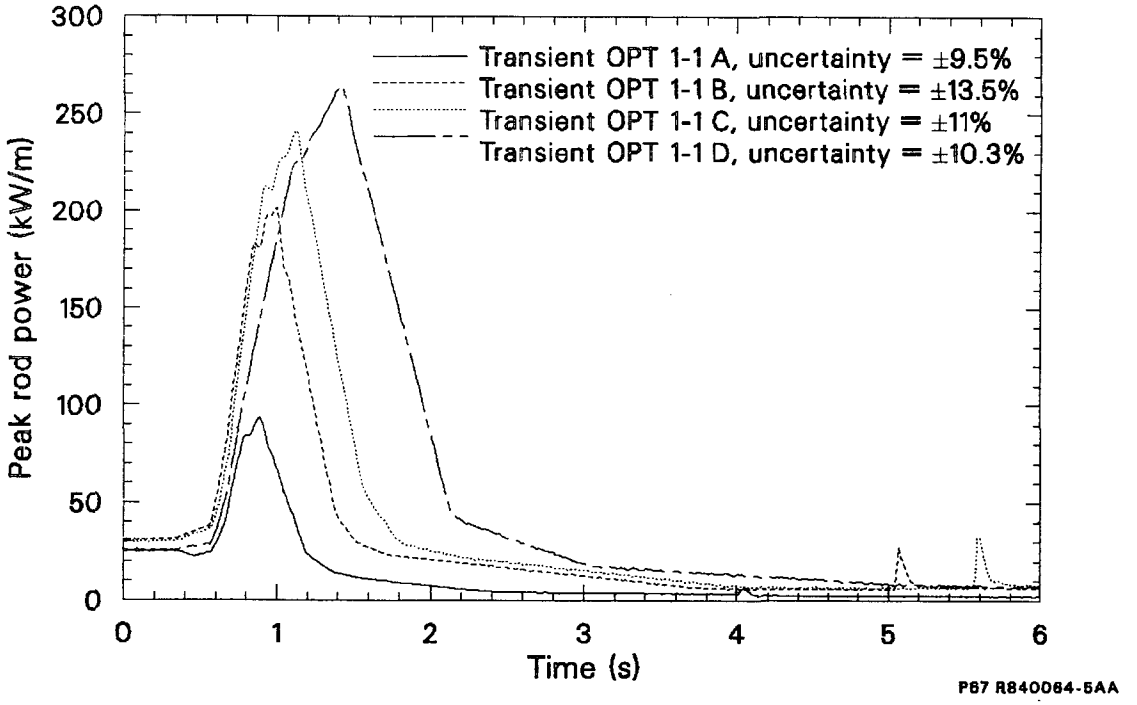

Figure 6. OPTRAN 1-1 peak fuel rod transient power.

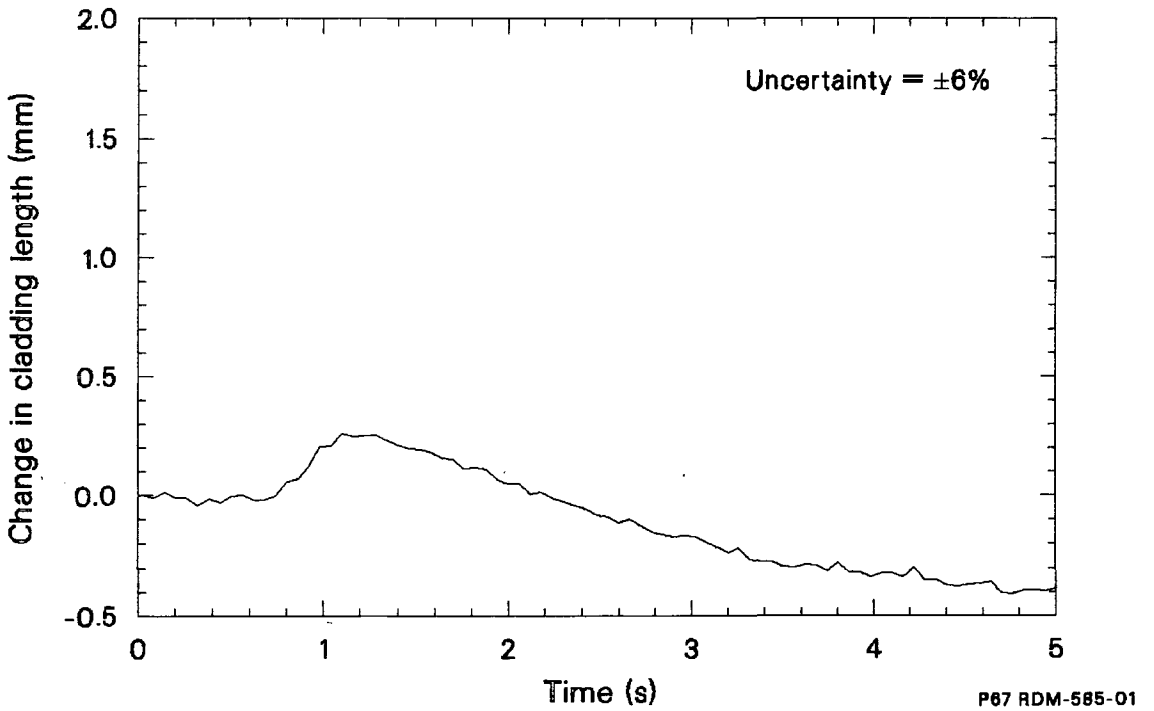

Figure 7. Cladding elongation Rod 901-1 during OPTRAN 1-1A transient.

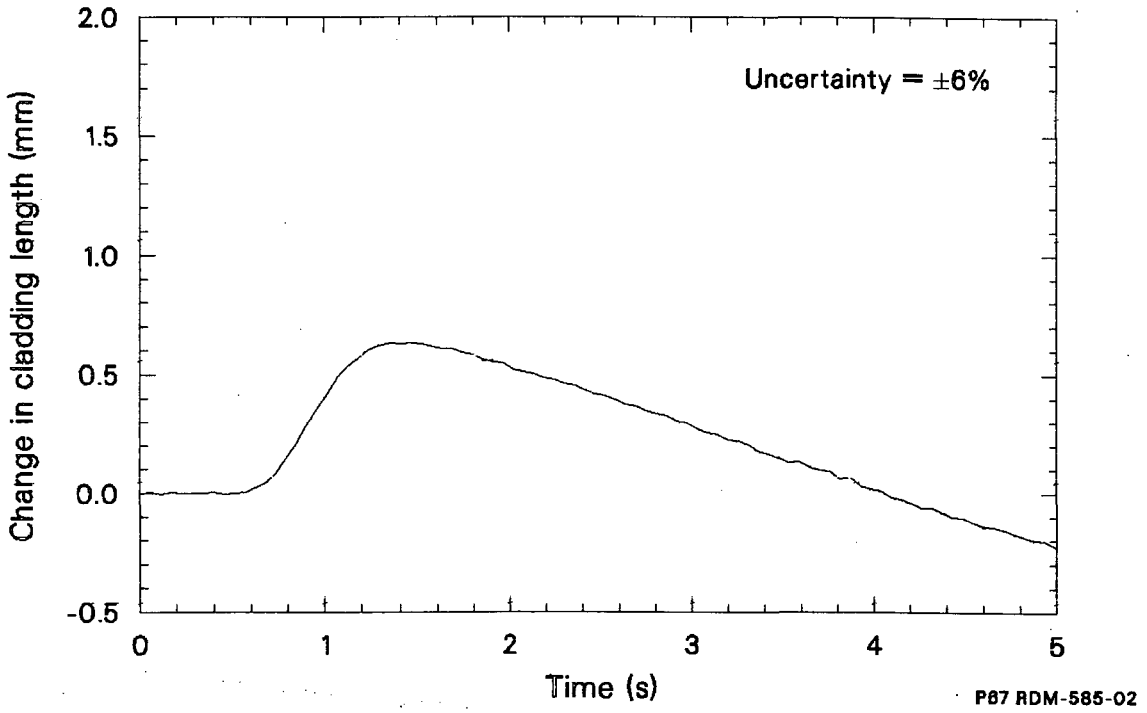

Figure 8. Cladding elongation Rod 901-6 during OPTRAN 1-1B transient.

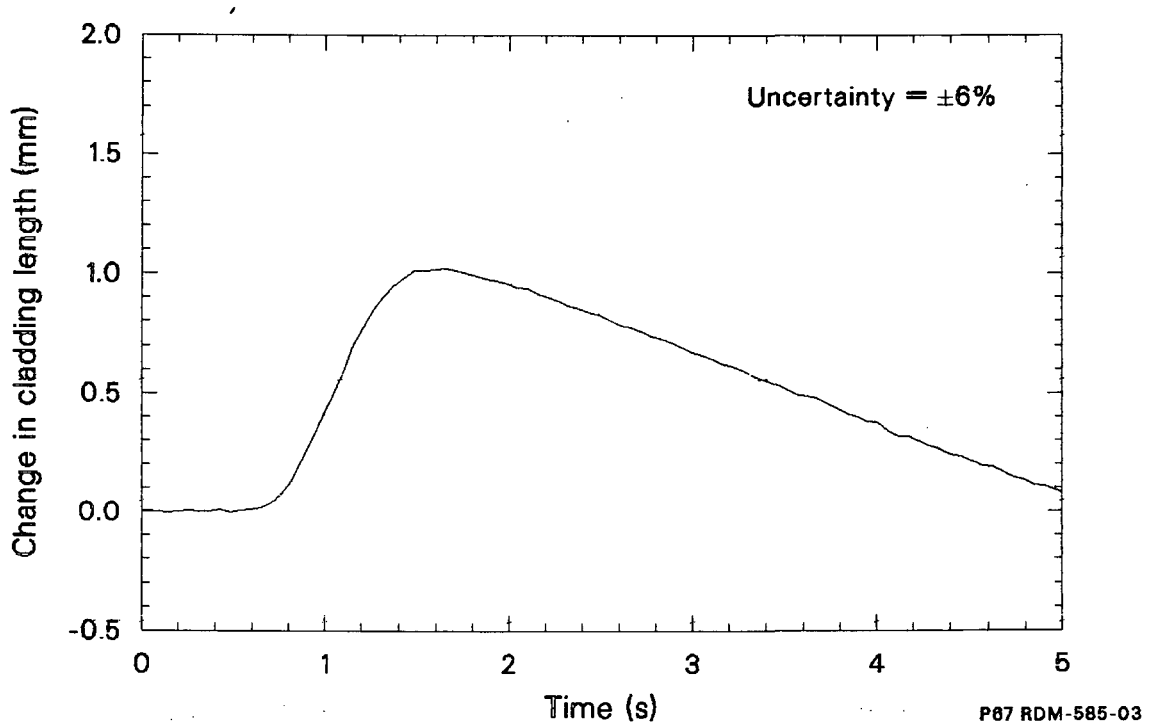

Figure 9. Cladding elongation Rod 901-6 during OPTRAN 1-1C transient.

Contact between the fuel and cladding apparently occurred at about 0.6 s, as in Transient B, when measured fuel rod elongation began. The peak cladding growth of 1.02 mm occurred at 1.49 s and then the fuel rod length began to decrease.

The measured axial growth for Rod 901-6 during OPTRAN 1-1 Transient D is shown in Figure 10. Contact between the fuel and cladding again occurred at about 0.6 s when measured fuel rod elongation began. The peak cladding growth of 1.81 mm occurred at 1.9 s, after which the fuel rod length began to decrease.

OPTRAN 1-2 Test Conduct

The nuclear operation for Test OPTRAN 1-2 consisted of an extensive fuel rod conditioning phase and a single power transient. An approximately 1-h power ramp and an approximately 3-h hold at steady reactor power preceded the transient. The nonnuclear operation consisted of two loop heatups and a radionuclide tracer injection in the loop to characterize fission product transport behavior. The test operation is shown schematically in Figure 11. The uncertainty in the power in Figure 11 is ±1.7 kW/m (2 sigma).

The purpose of the fuel conditioning phase was to measure the figure of merit (ratio of test fuel rod power to core power) and to carefully condition the irradiated fuel rods to a peak power of 29 kW/m since the Monticello BWR irradiation was at average rod powers of 9.2 kW/m for Rod 902-2 and 7.8 kW/m for Rod 902-4.

Maximum test rod power ramp rates were held to 0.5 kW/m/min up to 26 kW/m and 0.35 kW/m/h for rod powers in excess of 26 kW/m. The fuel conditioning phase was performed with single-phase coolant conditions to measure the rod power.

The power transient simulated a BWR main steam isolation valve closure ATWS for irradiated fuel rods operating slightly above BWR core-average peak rod powers. Prior to the power transient, the test rod peak powers were increased to 27 kW/m during a 1 1/2-h ramp and held constant for about 2 h. The test rod shroud outlet coolant conditions were initially maintained below saturation temperature to obtain a thermal-hydraulic power calibration of the heater rod and test rod powers.

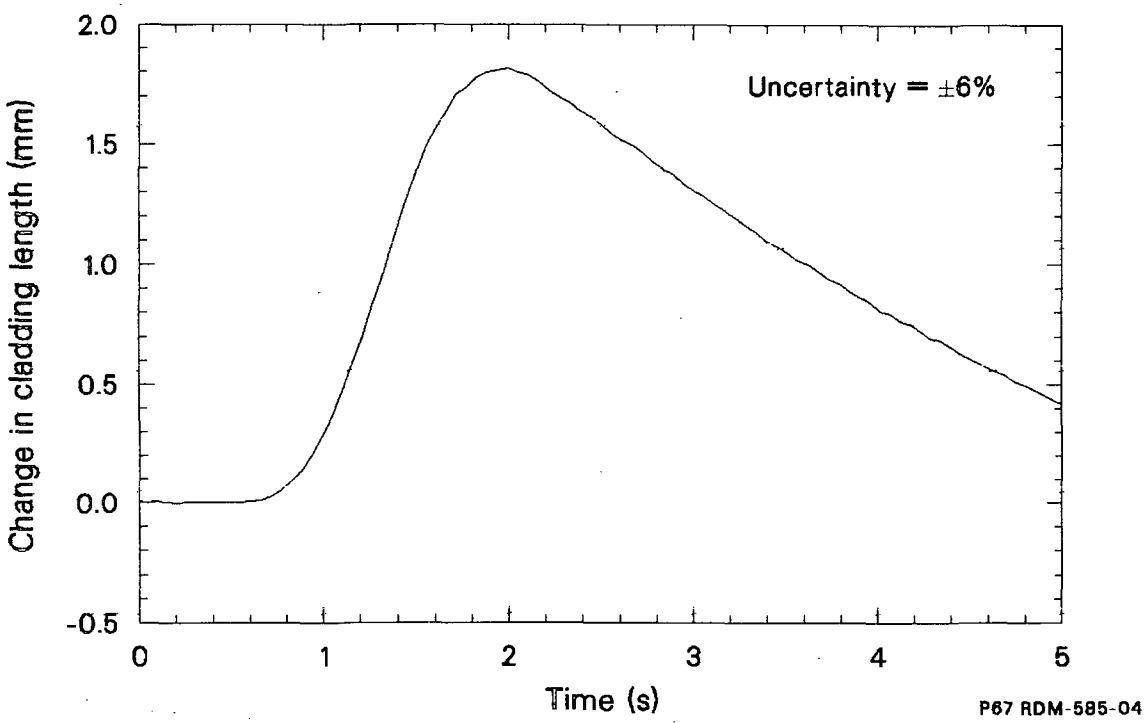

Figure 10. Cladding elongation Rod 901-6 during OPTRAN 1-1D transient.

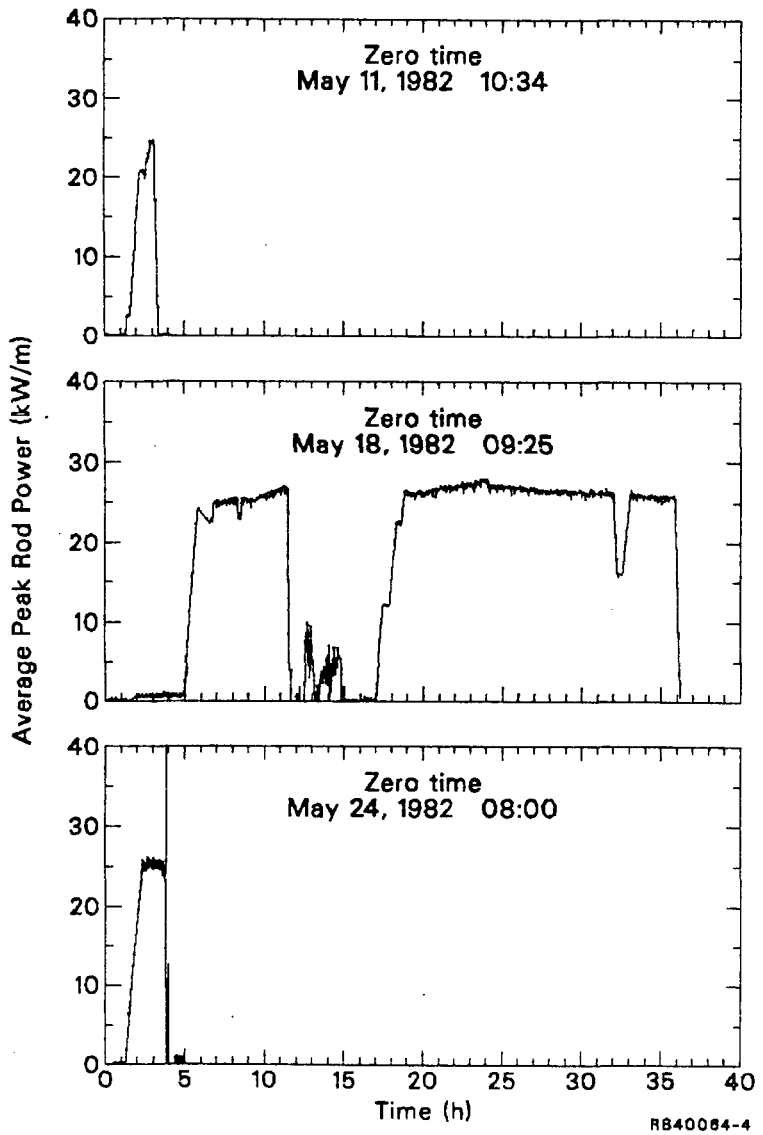

Figure 11. OPTRAN 1-2 fuel rod power history.

Saturated water conditions at the inlet of the test rods were then obtained by decreasing the coolant flow rate while keeping the variable orifices closed. Heater rod inlet coolant conditions were 550 K inlet temperature, 300 cm^3/s shroud flow rate, and 7.93 MPa coolant pressure. Prior to the power transient, the variable orifices were fully opened to reduce the test rod inlet coolant flows by about 55%.

During an actual BWR main steam isolation valve closure ATWS, the recirculation pumps would trip off and the core inlet flow rate would decrease by about 60% over a 16-s time span. The flow was reduced prior to the PBF transient to better maintain coolant conditions during the transient since the heater rod flow increased when the orifices were opened, and also to simplify timing the opening of the orifices with respect to the power transient. GE analyses for a main steam isolation valve closure ATWS indicate that the coolant pressure will rapidly increase from 7.24 MPa to a peak of ~8.96 MPa and then decrease to ~7.24 MPa over a 20-s time span. Since the PBF loop is not capable of simulating such a rapid pressure surge, a fixed pressure of 7.93 MPa was maintained during the test. This pressure was chosen because it is near the time-weighted average coolant pressure calculated by GE during the transient. In addition, 7.93 MPa

is equal to the midrange pressure set points of 7.79 to 8.07 MPa for opening the safety/relief valves of a BWR. The recirculation pump trip set point is also 7.93 MPa.

The PBF programmable reactor control system was used to obtain the power transient shown in Figure 12. The transient fuel rod power history was based on GE analysis for a fuel rod operating at maximum power. During the transient the peak test rod power increased from 27 to 300 ±25 kW/m, at a maximum ramp rate of 300 kW/m/s. The rod power was then reduced to 10 kW/m in about 32 s and was held constant at 10 kW/m for the next ∿1170 s.

Fission product release to the PBF loop coolant was observed by the fission product detection system (FPDS) during preconditioning and following the OPTRAN 1-2 transient. During preconditioning of the fuel rods, an indication of apparent rod failure was seen on three different instruments. Approximately 20 isotopes showed increases in coolant activity at the same time. The modest concentration levels of the isotopes, however, are indicative of a small cladding breach. Neither of the test fuel rods failed and, therefore, one or both of the heater rods were responsible for the measured radiation levels that indicated the pretransient leak and posttransient failure.

OPTRAN 1-2 Test Results

The measured relative cladding elongation for OPTRAN 1-2 test Rod 902-4 is shown in Figure 13. Contact between the fuel pellets and cladding apparently occurred at about 1 s when the fuel rod length began to increase. The cladding elongation reached a maximum of 5.6 mm at 4.5 s. This is twice the axial elongation that occurred during OPTRAN 1-1 Transient D even though the maximum powers were not that much different for OPTRAN 1-2 and OPTRAN 1-1D, 294 kW/m and 262 kW/m, respectively. The difference in axial elongation between the two experiments probably resulted because boiling transition occurred during OPTRAN 1-2 and cladding temperatures reached 940 to 1070 K, while boiling transition did not occur during the OPTRAN 1-1 transients.

The measured thermocouple response indicates that boiling transitions on Rod 902-4 occurred at 446 mm above the bottom of the rod but did not occur at either 546 or 646 mm. The measured temperature response at 446 mm for Rod 902-4 is shown in Figure 14. The maximum measured outside cladding surface temperature was 950 ±25 K. Thermocouples attached to Rod 902-2 indicated that boiling transition occurred at both 446 and 646 mm above the bottom of the rod but boiling transition did not occur at 546 mm. The maximum measured outside cladding surface temperature for Rod 902-2 was 1070 ±31 K at 446 mm.

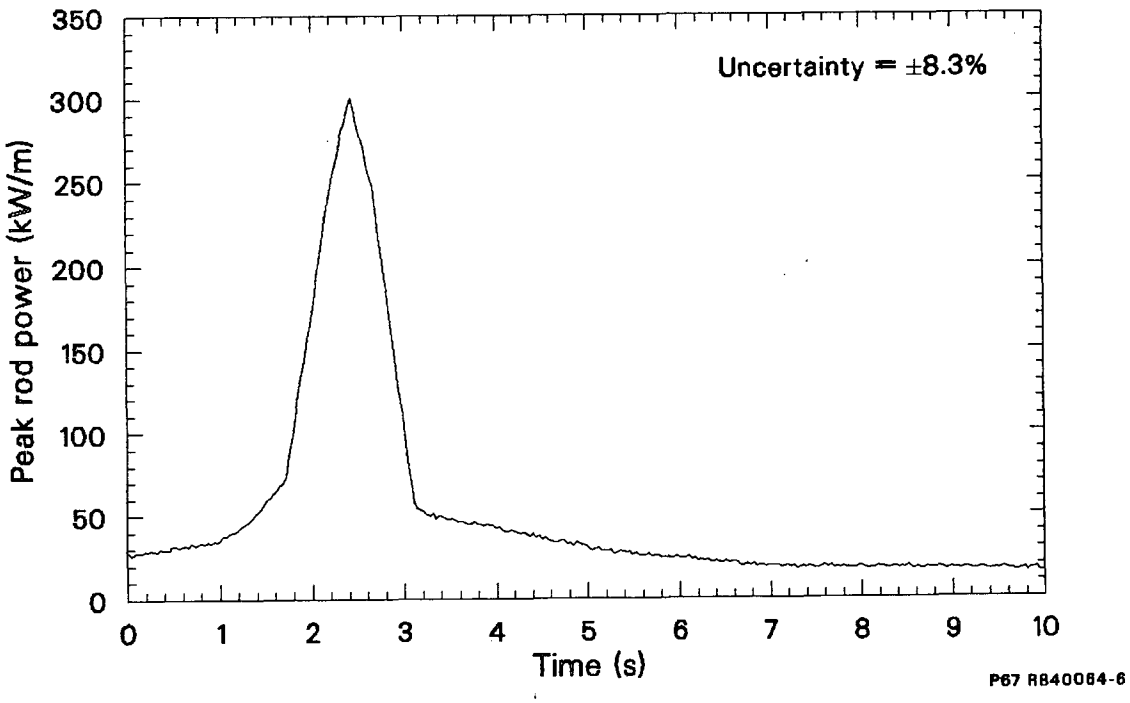

Figure 12. Test rod peak power during OPTRAN 1-2 transient.

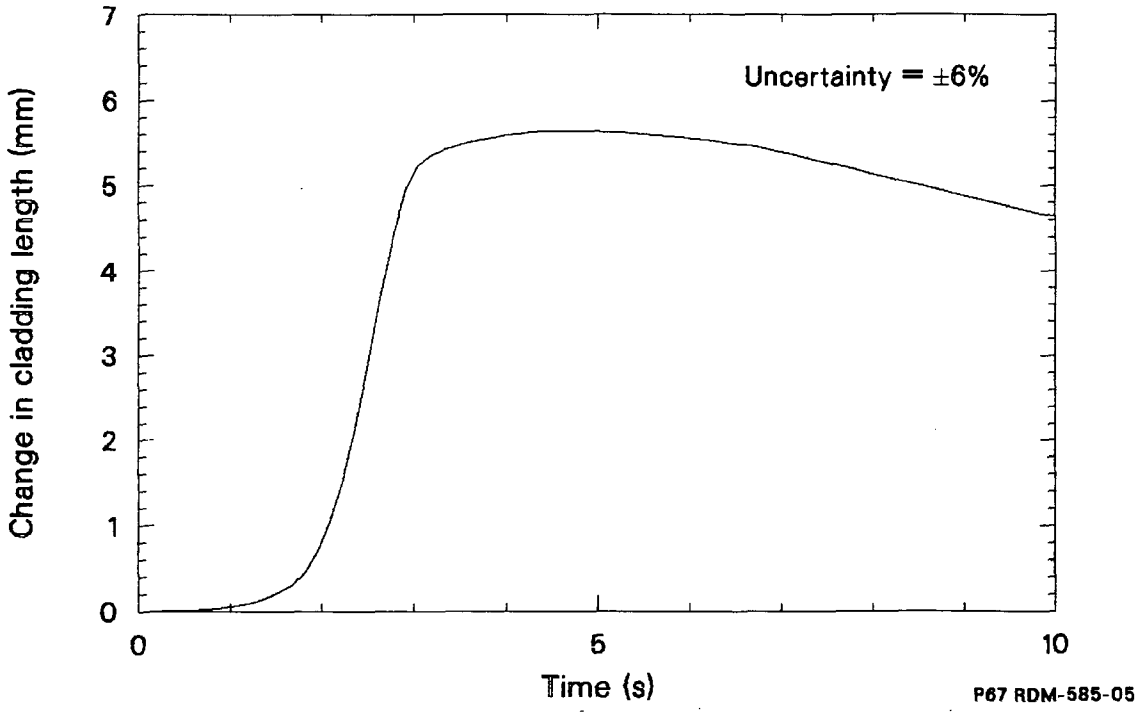

Figure 13. Cladding elongation Rod 902-4 during OPTRAN 1-2 transient.

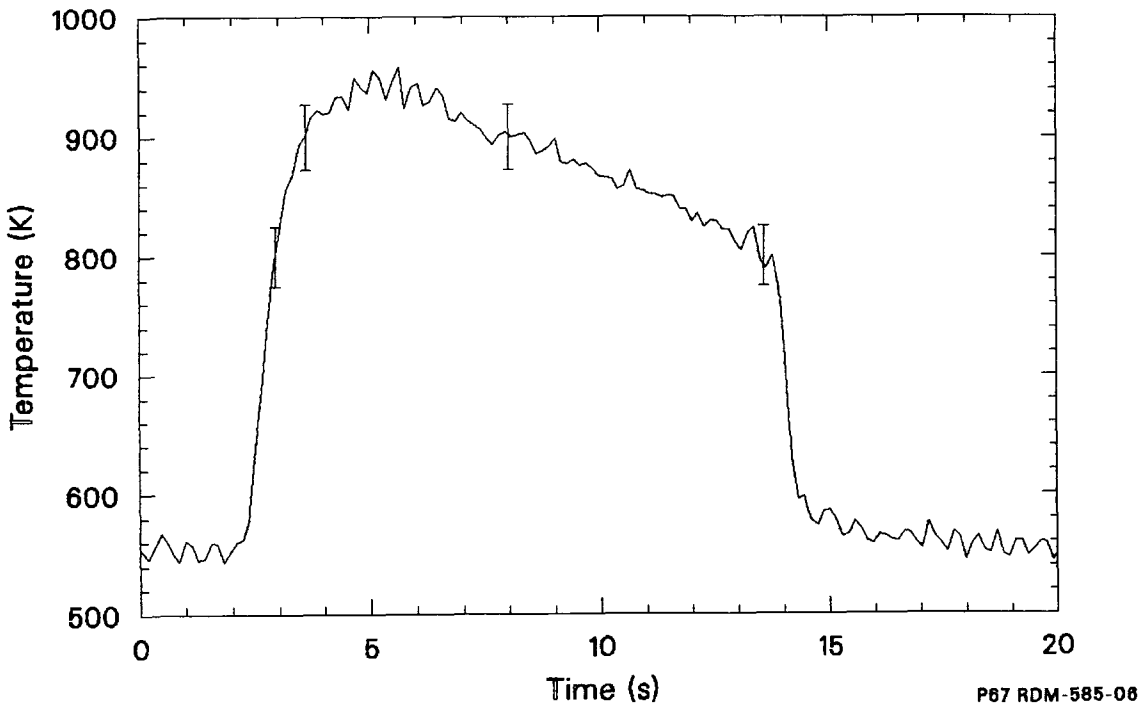

Figure 14. Cladding temperature Rod 902-4 at 70 mm above midplane.

POSTTEST ANALYSIS

Posttest analyses of the behavior of the OPTRAN 1-1 and OPTRAN 1-2 fuel rods was performed to gain insight into the timing and magnitude of the measured fuel rod elongations and their relationship with respect to PCI and possible PCI cracking of the cladding. The analyses of the OPTRAN 1-1 and 1-2 fuel rods were performed in two parts. The steady-state fuel rod analysis computer code FRAPCON-2[13] was used in the first part to calculate fuel rod behavior during the steady-state irradiation in the Monticello reactor and the preconditioning in PBF. Then, the transient fuel rod analysis code FRAP-T6[14] was used to calculate the behavior of fuel rods subjected to the operational transients described in the preceding section. The FRACAS-II subcode[15] was used in all the FRAPCON-2 and FRAP-T6 analyses. The FRACAS-II subcode has fuel and cladding deformation models that are designed to analyze PCI during operational transients or ATWS events. In the following subsections, the FRAPCON-2 analyses results for Rods 901-1 and 901-6 in the OPTRAN 1-1 experiment and Rod 902-4 in the OPTRAN 1-2 experiment are discussed first and then the FRAP-T6 analyses results for these rods are presented.

FRAPCON-2 Calculations for Steady-State Irradiation and Preconditioning

In order to properly calculate the transient behavior of the OPTRAN fuel rods, the steady-state behavior of the fuel rods during the commercial reactor irradiation and the PBF preconditioning had to be analyzed. The FRAPCON-2 code was used for these steady-state calculations. Each of the three rods, 901-1, 901-6, and 902-4, were subjected to three different power levels during steady state irradiation. The time-averaged values of these power levels were used in the FRAPCON-2 analysis. Table 1 gives the time-averaged power levels experienced and the burnup attained by the three fuel rods in the FRAPCON-2 analyses that simulated steady-state irradiation in the Monticello reactor. Table 1 also gives the maximum average power levels and the time at those power levels used in the FRAPCON-2 analysis which simulated the preconditioning of the three fuel rods in the PBF.

Figure 15 shows the axial power profiles used to analyze steady-state irradiation of the three rods. Rods 901-1 and 901-6 were irradiated in the lower portion of the Monticello core and Rod 902-4 was irradiated in the upper portion of the core. Figure 16 shows the axial power profile used to analyze preconditioning performed in the PBF for all three rods.

The FRAPCON-2 code was modified to delete the cladding creepdown calculations because the test fuel rod cladding is recrystalized zircaloy (annealed at 575 K for 2 to 2-1/2 h).[16,17] Recrystalized zircaloy experiences very little deformation due to creepdown and this was confirmed by the cladding outer diameter measurements during pretest characterization of Rods 901-1, 901-6, and 902-4. For example, the cladding outer diameter of Rod 902-4 decreased during irradiation in the Monticello reactor by 0.08%,[17] which is significantly smaller than the 0.973% calculated by the cladding creepdown model in FRAPCON-2.

Rod 901-1 was modeled with five equally spaced axial nodes. Table 2 gives the FRAPCON-2 calculations for densification, swelling, maximum temperatures, and local burnups experienced by the fuel at each of its axial nodes during steady-state irradiation and preconditioning. During steady-state irradiation, the maximum fuel temperature was the lowest at Node 1 and the highest at Node 5. Therefore the fuel experienced minimum swelling at Node 1 and the maximum swelling at Node 5. The volumetric strain due to densification and swelling is three times the percentage change in radius listed in Table 2.

During preconditioning, the maximum fuel temperature was the lowest at Node 5 and the highest at Node 3. The local burnup at the end of preconditioning was maximum at Node 5 and minimum at Node 1.

Rod 901-6 was also modeled with five equally spaced nodes. Table 3 gives FRAPCON-2 calculations for densification, swelling, maximum temperatures, and local burnups experienced by fuel at each of its axial nodes during steady-state irradiation and preconditioning.

Table 1. Power levels and burnups during steady-state irradiation and preconditioning for Rods 901-1, 901-6, and 902-4

	Steady-State Irradiation		Preconditioning	
Fuel Rod	Average Power (kW/m)	Average Burnup (GWd/mtu)	Maximum Average Power (kW/m)	Time (h)
901-1	10.96	12.823	21.6	15.2
901-6	11.15	13.060	24.00	25.1
902-4	7.81	9.112	21.60	16.0

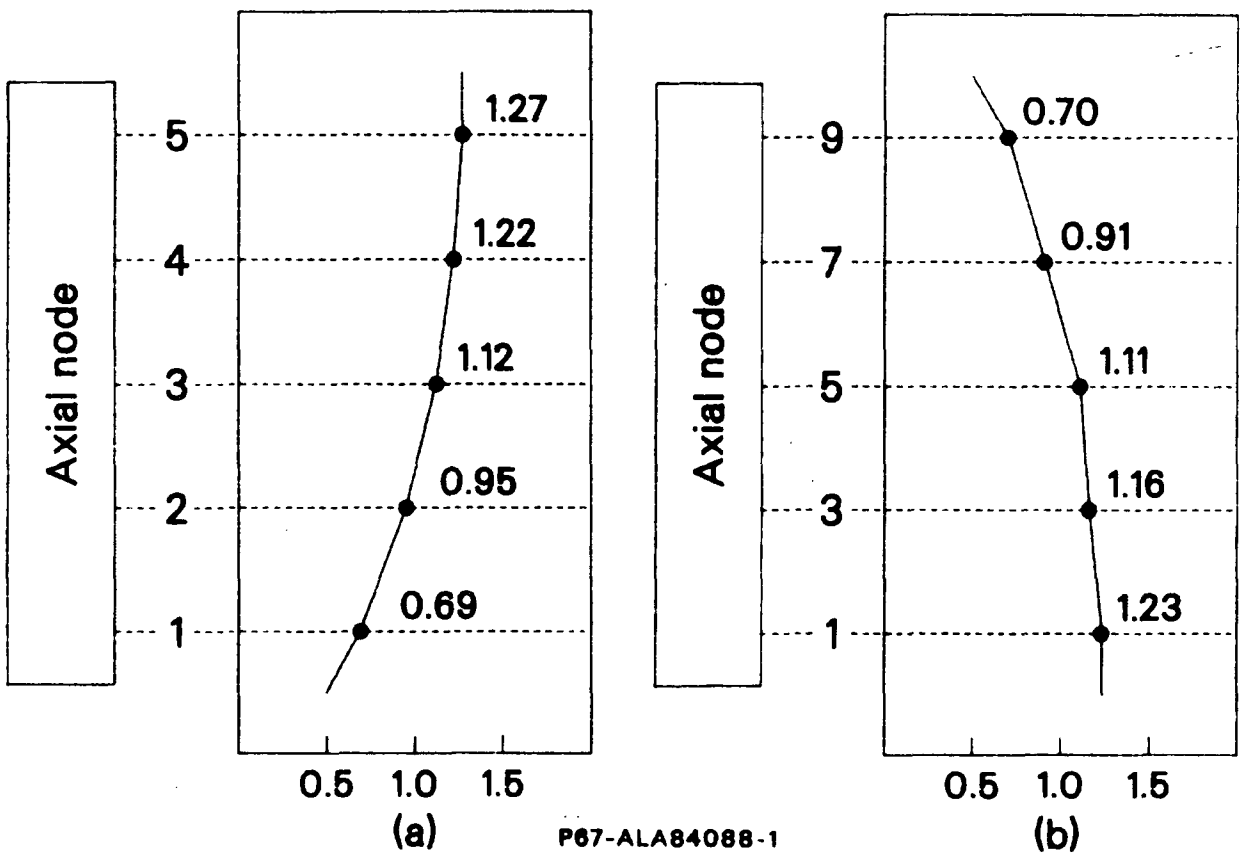

Figure 15. Axial power distribution during steady-state irradiation; Rods (a) 901-1 and 901-6, (b) 902-4.

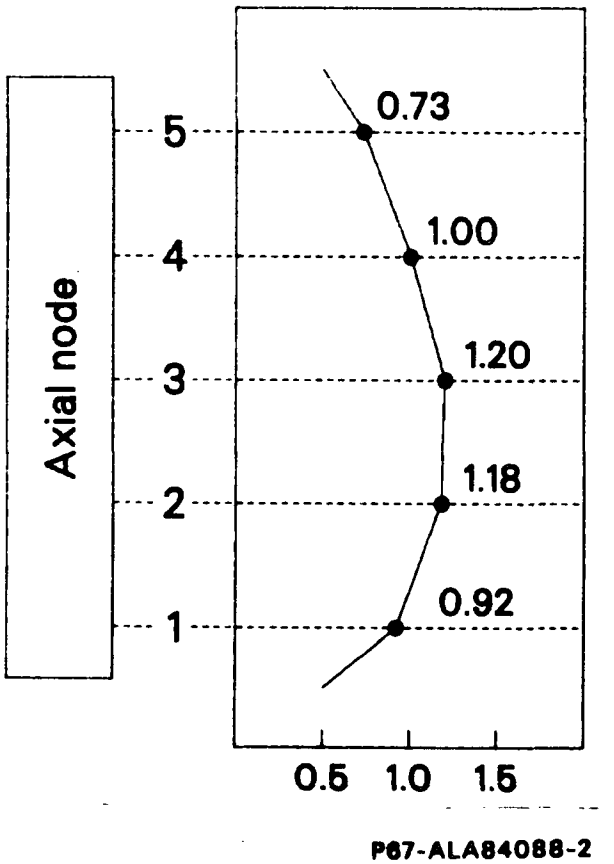

Figure 16. Axial power distribution during preconditioning; Rods 901-1 and 901-6.

Table 2. Densification, swelling, and local burnups for Rod 901-1

	Steady-State Irradiation			Preconditioning	
	Change in Radius Due to				
Node Number	Densification (%)	Swelling (%)	Maximum Temperature (K)	Maximum Temperature (K)	Local Burnup (GWd/mtu)
1	-0.264	0.074	826	1350	8.897
2	-0.264	0.160	918	1428	12.232
3	-0.264	0.188	976	1433	14.339
4	-0.431	0.243	1023	1306	15.611
5	-0.501	0.255	1060	1127	16.339

Table 3. Densification, swelling, and local burnups for Rod 901-6

	Steady-State Irradiation			Preconditioning	
	Change in Radius Due to				
Node Number	Densification (%)	Swelling (%)	Maximum Temperature (K)	Maximum Temperature (K)	Local Burnup (GWd/mtu)
1	-0.264	0.073	824	1434	8.897
2	-0.264	0.159	914	1517	12.143
3	-0.264	0.187	973	1522	14.253
4	-0.431	0.241	1019	1385	15.514
5	-0.501	0.253	1056	1189	16.235

Rod 902-4 experienced film boiling and therefore, this rod was modeled with nine axial nodes to accurately calculate the extent of the film boiling region on the cladding outside surface. Table 4 gives FRAPCON-2 calculations for the densification swelling, maximum temperatures, and local burnups for Nodes 1, 3, 5, 7, and 9. The swelling experienced by Rod 902-4 was smaller than that experienced by Rods 901-1 and 901-6 because Rod 902-4 had a smaller burnup.

The maximum calculated fuel temperatures were <1060 K during steady-state irradiation of all three rods considered here. Therefore, the fuel swelling model FSWELL[19] in FRAPCON-2 calculated very little swelling, implying that a small amount of fission products were accumulated at the fuel grain boundaries. Thus, little release of fission products to the gap would be expected during transient testing.

The FRAPCON-2 results indicate that none of the three fuel rods experienced radial PCI during the steady state irradiation in Monticello or preconditioning in PBF. A fuel rod at the beginning of life (i.e., unirradiated fuel rod) generally has random pellet stacking, pellet cocking, cladding ovality, cladding eccentricity, pellet chipping, and/or pellet hourglassing that cause axial PCI to take place earlier (i.e. at lower power) than radial PCI.[20] Once radial PCI takes place, then the fuel pellets become concentric and from that time onward, axial and radial PCI will take place at nearly the same time (or power). The OPTRAN test fuel rods did not experience any PCI during the steady-state irradiation in the Monticello reactor. In addition, the preconditioning was performed at power too low for radial PCI to take place and eliminate pellet eccentricity. Thus, the causes of an early axial PCI were not eliminated before the transient tests began and therefore it is likely that these rods experienced early axial PCI during the transient testing.

FRAP-T6 Calculations for Rod 901-1. Rod 901-1 was subjected to one power pulse, transient A in Figure 6, that simulated a BWR turbine trip without steam bypass. The calculated peak fuel rod power increased from 23.82 kW/m to 88.28 kW/m in 0.32 s. Then, in the following 0.32 s, it dropped to 22.08 kW/m. The peak fuel rod power in the FRAP-T6 analysis was 4% lower than that measured in the test because no axial node was located at the elevation of the largest axial power ratio.

The experimental observations regarding the axial and radial PCIs suggest that an axial PCI took place earlier (i.e., at lower power) than the radial PCI, and it took place at $\sim$0.68 s.

The values of the variable DIFGAP given in Table 5 were selected such that an axial PCI would take place in the calculations at all the axial nodes simultaneously at 0.68 s in the transient. The variable DIFGAP is a ratio of the pellet-cladding gap at the beginning of axial PCI to the as-fabricated pellet-cladding gap.[21] This is required input because there is no model in the code for the timing of the onset of early axial PCI. If the axial PCIs were begun at lower power during preconditioning, then the values of the variable DIFGAP would be larger.

Table 4. Densification, swelling, and local burnups for Rod 902-4

	Steady-State Irradiation			Preconditioning	
	Change in Radius Due to				
Node Number	Densification (%)	Swelling (%)	Maximum Temperature (K)	Maximum Temperature (K)	Local Burnup (GWd/mtu)
1	-0.264	0.129	884	1174	11.194
2	-0.264	0.107	868	1401	10.602
3	-0.264	0.102	854	1429	10.089
4	-0.264	0.060	804	1360	8.292
5	-0.264	0.009	751	1087	6.395

Table 5. Values of variable DIFGAP for the transient analysis of Rod 901-1

Axial Node	DIFGAP
1	0.337
2	0.067
3	0.053
4	0.121
5	0.211

Figure 17 shows the radial power profiles for the Rod 901-1 fuel pellet that had an enrichment of 2.87%. Two radial power profiles are shown, one for fresh fuel and another for fuel irradiated to the burnup of 12.9 GWd/mtu. These radial power profiles were calculated using a computer subcode, FLXDP, which was extracted from the FRAPCON-2 code.[13] The radial power profile for the irradiated fuel has a greater slope than that for the fresh fuel that will cause lower fuel centerline temperatures in the irradiated fuel and consequently smaller elongation of the fuel stack. The radial power profile for the irradiated fuel was used for the FRAP-T6 analysis.

A limitation of the subcode FLXDP in FRAPCON-2 is that it calculates the radial power profile for an irradiated fuel pellet as a function of its enrichment and the number of hours of irradiation but not as a function of burnup. Therefore, FLXDP calculated the same radial power profile for the transient analysis of all three rods since they were irradiated for the same length of time in the Monticello reactor, even though Rod 902-4 had a lower average burnup than Rods 901-1 and 901-6. Similarly, FLXDP calculated the same radial power profile for all the axial nodes of a fuel rod even though local burnup varied up to a factor of 2, as shown in Tables 2 through 4. Additionally, the same radial power profile was used for the transient analysis of all three rods because FRAP-T6 uses the same radial power profile for all the axial nodes.

The results of the posttest analysis for Transient A are presented in Figures 18 and 19, and are summarized in Table 6. Figure 18 shows FRAP-T6 calculations for average and peak fuel temperatures and rod power. The maximum fuel centerline temperature was 1226.0 K at Node 3 at 1.2 s and it lagged the maximum power by 0.31 s. The maximum calculated cladding surface temperature was 576.4 K, implying that film boiling did not occur.

A comparison between measured and calculated relative cladding elongation is presented in Figure 19. The measurements indicate that axial PCI began no later than 0.68 s and that the rate of increase in cladding axial elongation was 0.78 mm/s. FRAP-T6 calculations indicate that the rate of increase in cladding elongations was 0.77 mm/s, which is in good agreement with the measurements. The maximum measured relative cladding elongation was 0.28 mm during the 1.1- to 1.2-s time period. The maximum calculated relative cladding elongation was 0.296 mm at 1.2 s. The measured results indicate that after reaching the maximum, the cladding elongation decreased at the rate of 0.28 mm/s, while the corresponding calculated result was 0.22 mm/s. The measured results show that axial PCI continues beyond 4.0 s causing the cladding to continually shrink while the calculated results indicate that the axial PCI ended at 2.60 s. One possible explanation for this discrepancy is that an axial PCI might have started during preconditioning at peak power lower than 23.82 kW/m.

The calculated results indicate that no radial PCI took place. The maximum calculated hoop stress was due to the difference between coolant pressure and internal gas pressure and was equal to -54.6 MPa.

FRAP-T6 Calculations for Rod 901-6. Rod 901-6 was subjected to three consecutive power pulses, Transients B, C, and D, shown in Figure 6. Transient B simulated a generator load rejection without steam bypass transient for fuel rods operating at above average BWR rod powers. Transients C and D were performed at progressively higher powers in an attempt to determine the failure threshold.

Transient B. The peak fuel rod power increased from 37.13 kW/m to 204.75 kW/m in 0.45 s during transient B. Then, in the following 0.44 s, fuel rod power decreased to 18.7 kW/m.

The results of the posttest analysis for Transient B are presented in Figures 20 through 22 and summarized in Table 6. Figure 20 shows the FRAP-T6 calculations for average and the maximum fuel centerline temperature and rod power for Rod 901-6 subjected to the transient B. The peak rod power at the beginning of the transient (0.0 s) was 30.74 kW/m and the corresponding maximum calculated fuel centerline temperature was 1369.8 K. The maximum calculated fuel centerline temperature was 1612.2 K at 1.48 s and it lagged maximum power by 0.44 s. Film boiling was not predicted to occur. The maximum calculated cladding outside surface temperature was 584.5 K.

The maximum calculated fuel centerline temperature at 0.0 s was higher than the maximum fuel centerline temperature experienced by Rod 901-1 because at time 0.0 s, Transient B had a higher steady-state peak power (30.74 kW/m) than the corresponding power for Transient A (23.82 kW/m). Therefore, the calculations indicate

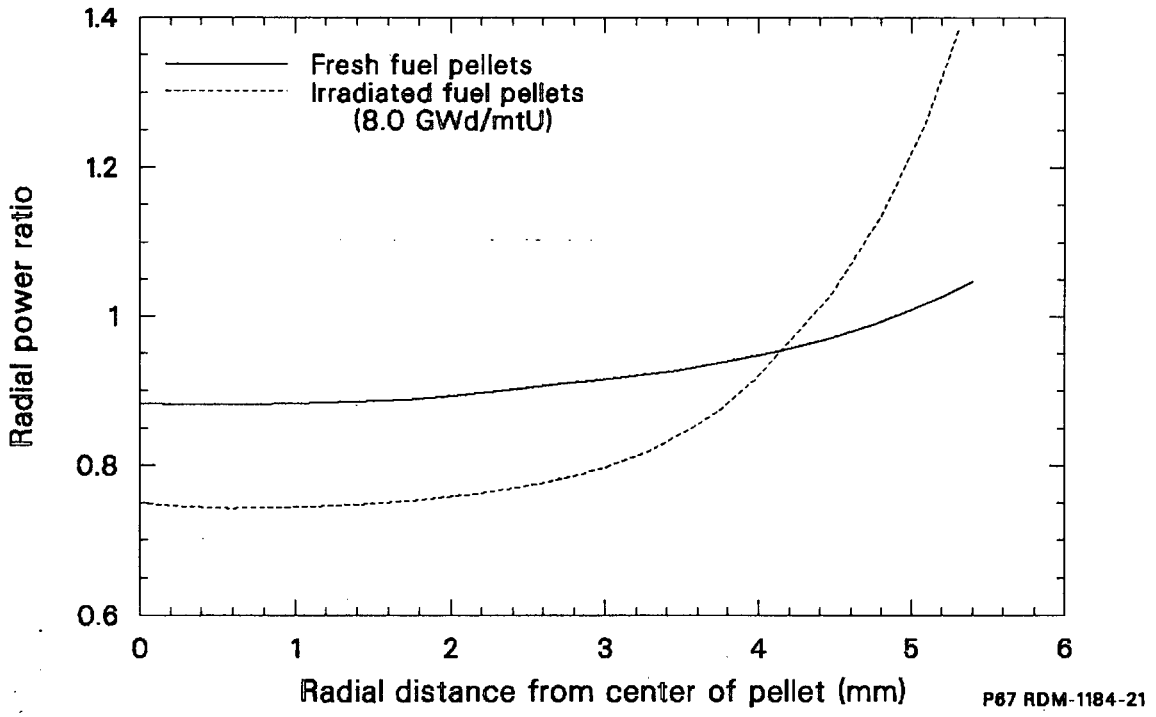

Figure 17. Radial power profiles for unirradiated and irradiated fuel pellets, Rod 901-1 OPTRAN 1-1.

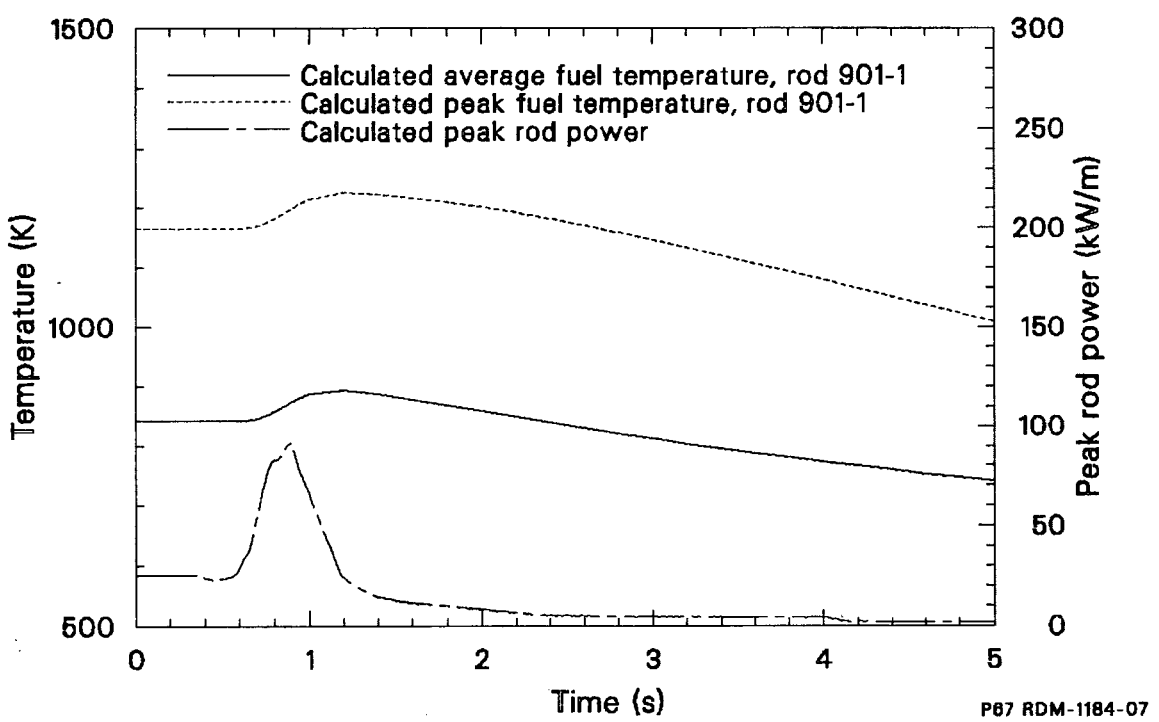

Figure 18. Calculated average and peak fuel temperatures, Rod 901-1 during OPTRAN 1-1A.

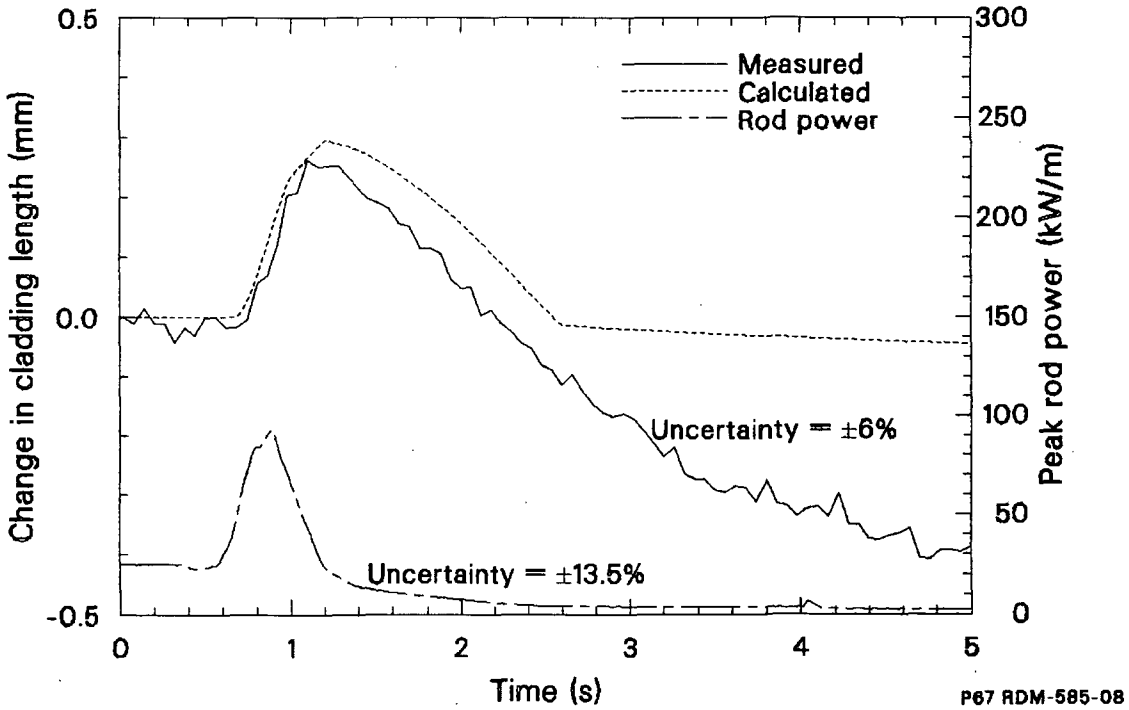

Figure 19. Comparison of measured and calculated cladding elongation with fuel rod power, Rod 901-1 during OPTRAN 1-1A.

Table 6. Summary of FRAP-T6 results for OPTRAN transient tests

Rod Number	Transient Number	Average Burnup (MWd/mtu)	Transient Peak Fuel Rod Power (kW/m)	Peak Centerline Temperature (K)	Maximum Cladding Surface Temperature (K)	Maximum Relative Fuel Stack Elongation (mm)	Maximum Relative Clad Elongation (mm)	Maximum Clad Hoop Strain (% m/m)	Maximum Clad Hoop Stress (MPa)	Peak Volume Averaged Temperature (K)	Enthalpy (cal/g)
901-1	A	12.82	88.28	1226	576	0.296	0.296	0.136	-54.6	894	46
901-6	B	13.06	204.75	1612	585	1.554	0.783	0.248	85.0	1129	67
901-6	C	13.06	224.20	1670	588	2.377	1.128	0.252	114.8	1178	72
901-6	D	13.06	262.10	1789	590	3.971	1.728	0.298	188.0	1279	81
902-4	—	9.11	294.00	2074	958	4.853	4.763	0.269	110.2	1399	97

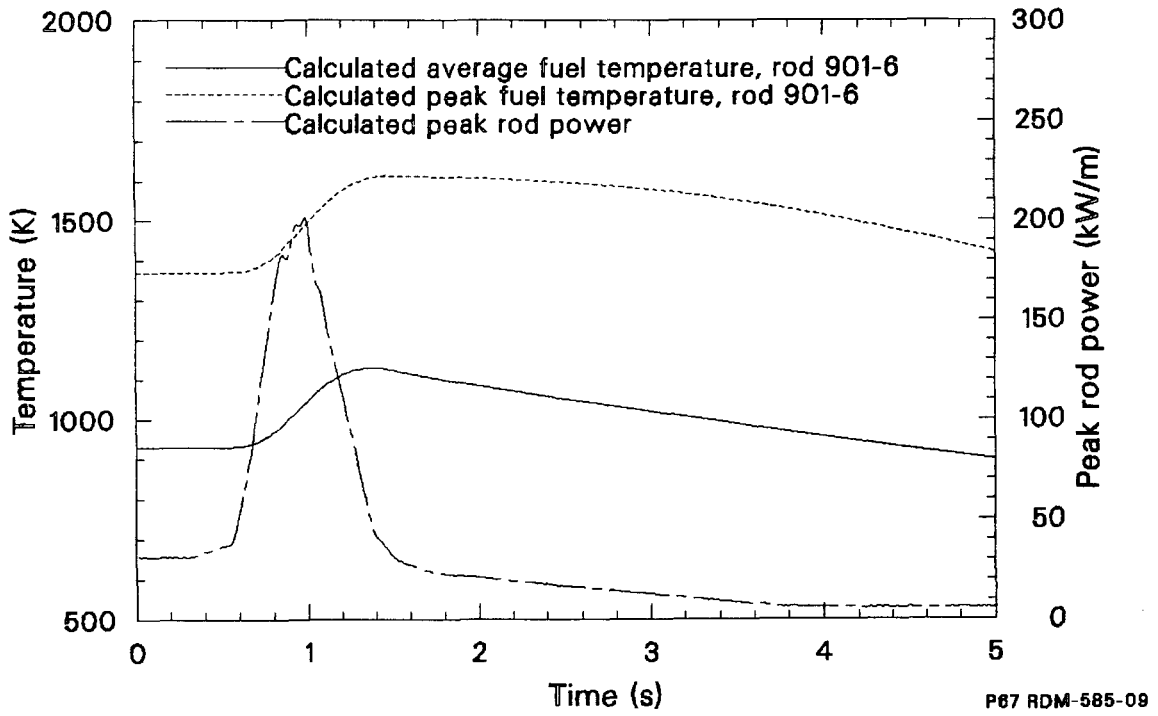

Figure 20. Calculated average and peak fuel temperatures, Rod 901-6 during OPTRAN 1-1B.

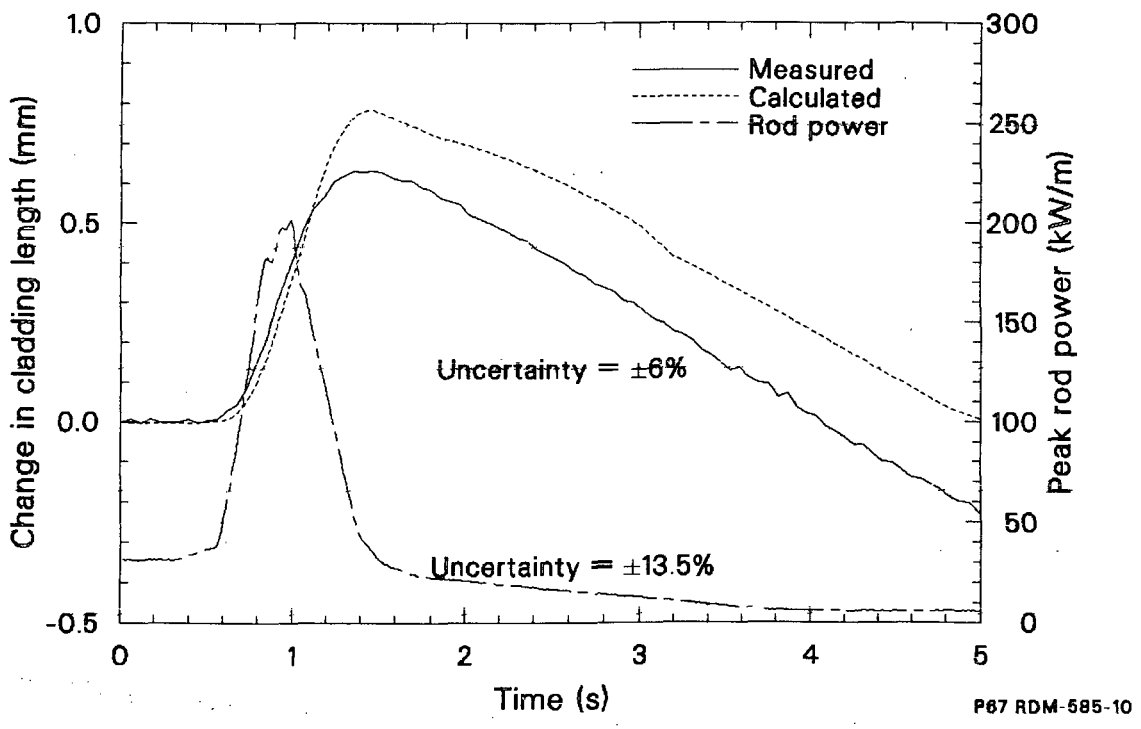

Figure 21. Comparison of measured and calculated cladding elongation with fuel rod power, Rod 901-6 during OPTRAN 1-1B.

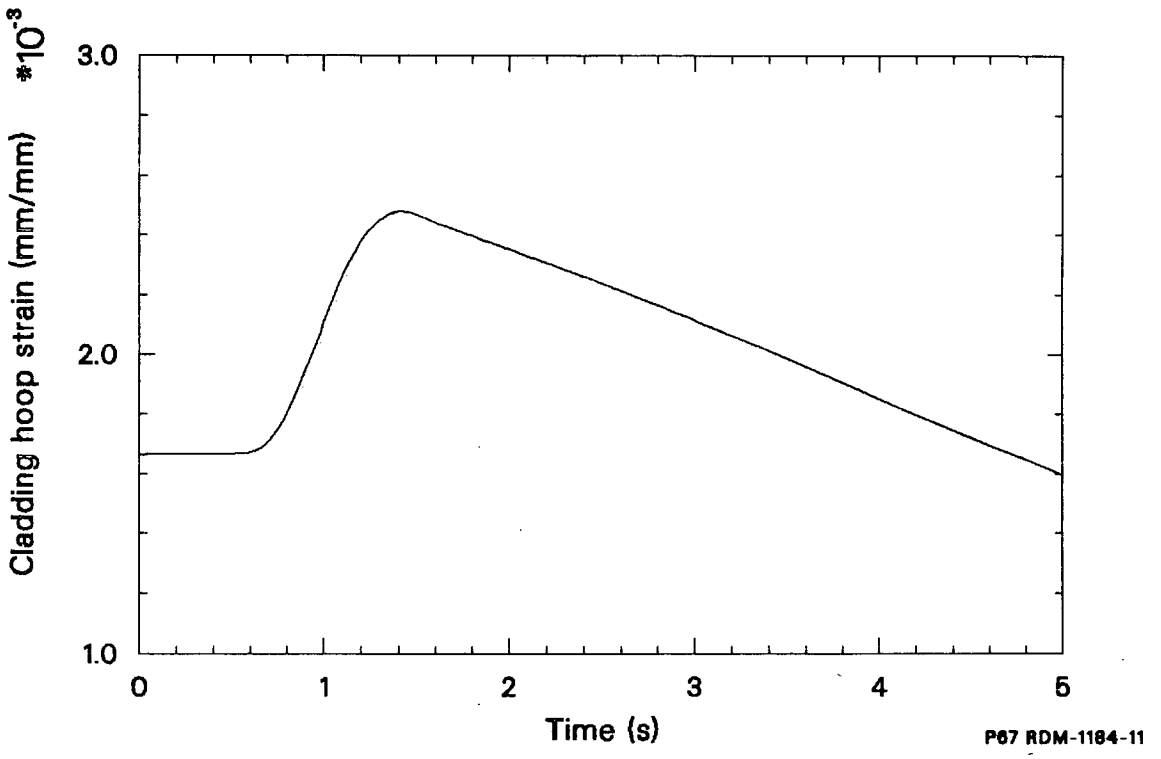

Figure 22. Calculated maximum cladding hoop strains versus time, Rod 901-6 during OPTRAN 1-1B.

that Rod 901-6 experienced both axial and radial PCI at 0.05, while Rod 901-1 experienced only axial PCI.

The comparison between measured and computed relative cladding elongation is shown in Figure 21. Based on the measured results the values for the variable DIFGAP were selected such that an axial PCI would take place during the calculations at all the axial nodes simultaneously at 0.62 s in the transient. The calculated cladding elongation increased at a rate of 1.35 mm/s, while the corresponding measured value was 1.36 mm/s. The maximum relative calculated elongation was 0.78 mm at 1.44 s, while the corresponding measured result was 0.64 mm at 1.3 s. The calculated rate of decrease in cladding elongation was 0.22 mm/s, while the measured value is 0.23 mm/s. The calculated results indicate that the relative cladding elongation was -0.04 mm at 5 s and the axial PCI was released. The measured results show that the relative cladding elongation was -0.36 mm at 5 s, the axial PCI was not released, and the cladding continued to contact the fuel.

The calculated results for hoop strains indicate that the central three nodes experienced radial PCI. The maximum calculated hoop strains were experienced at axial Node 2 and are shown in Figure 22. The maximum calculated hoop strain was 0.248% at 1.4 s. The maximum hoop stress was 84.97 MPa. The calculated permanent cladding hoop strains were small and remained negative at all the axial nodes.

The calculated cladding hoop strain and stress results may be higher than the actual ones because of a limitation of the fuel compliance model in FRAP-T6. The fuel compliance model in FRAP-T6 takes into account two phenomena that affect the calculation of the maximum cladding hoop strain during radial PCI: the compliance of cracked fuel pellets and cladding ridge formation.[22] The crack voids in fragmented fuel accommodate some fraction of the thermoelastic pellet deformation and make the pellet more compliant under the restraint of the cladding during PCI. The fuel compliance model in FRAP-T6 is based on the experimental results for fuel rods having dished pellets, while the OPTRAN test rods had flat-ended pellets. As dished-ended pellets are likely to produce bigger ridges during radial PCI than those produced by flat-ended pellets, FRAP-T6 may have overestimated the hoop strain results for Rod 901-6.

Transient C. The peak fuel rod power increased from 28.79 kW/m to 244.2 kW/m in 1.02 s during Transient C. Then, in the following 0.80 s, the peak power decreased to 28.59 kW/m.

The results of the posttest analysis for transient C are presented in Figures 23 through 25 and summarized in Table 6. Figure 23 shows the FRAP-T6 calculations for average and maximum fuel centerline temperatures and rod power for the period during which Rod 901-6 was subjected to Transient C. The maximum calculated fuel centerline temperature was 1670 K at 2.62 s and it lagged the maximum power by 1.60 s. Film boiling was not predicted to occur. The maximum calculated cladding surface temperature was 588 K.

The comparison between measured and calculated relative cladding elongation is shown in Figure 24. The calculated axial PCI started at 0.82 s, while the corresponding measured result was 0.62 s. The calculated cladding elongation increased at the rate of 1.55 mm/s, while the corresponding measured result was 1.46 mm/s. The maximum relative calculated elongation was 1.128 mm at 1.82 s, while the corresponding measured result was 1.02 mm at 1.49 s. The calculated rate of decrease in cladding elongation was 0.26 mm/s, compared with a measured value of 0.29 mm/s. Both the calculations and measurements indicate that axial PCI did not release until 5 s.

The calculated hoop strains indicate that the central three nodes experienced radial PCI. The maximum calculated hoop strain occurred at Node 3 and is shown in Figure 25. The maximum calculated hoop strain was 0.25% at 1.62 s. The maximum calculated hoop stress was 114.8 MPa. The calculated permanent cladding hoop strains were small and remained negative at all the axial nodes.

Transient D. The peak fuel rod power increased from 26.50 kW/m to 262.1 kW/m in 1.0 s during Transient D. Then, in the following 0.8 s, the peak power dropped to 38.89 kW/m.

The results of the posttest analysis for Transient D are presented in Figures 26 through 28 and summarized in Table 6. Figure 26 shows the FRAP-T6 calculations for average and maximum fuel centerline temperatures and rod power for the

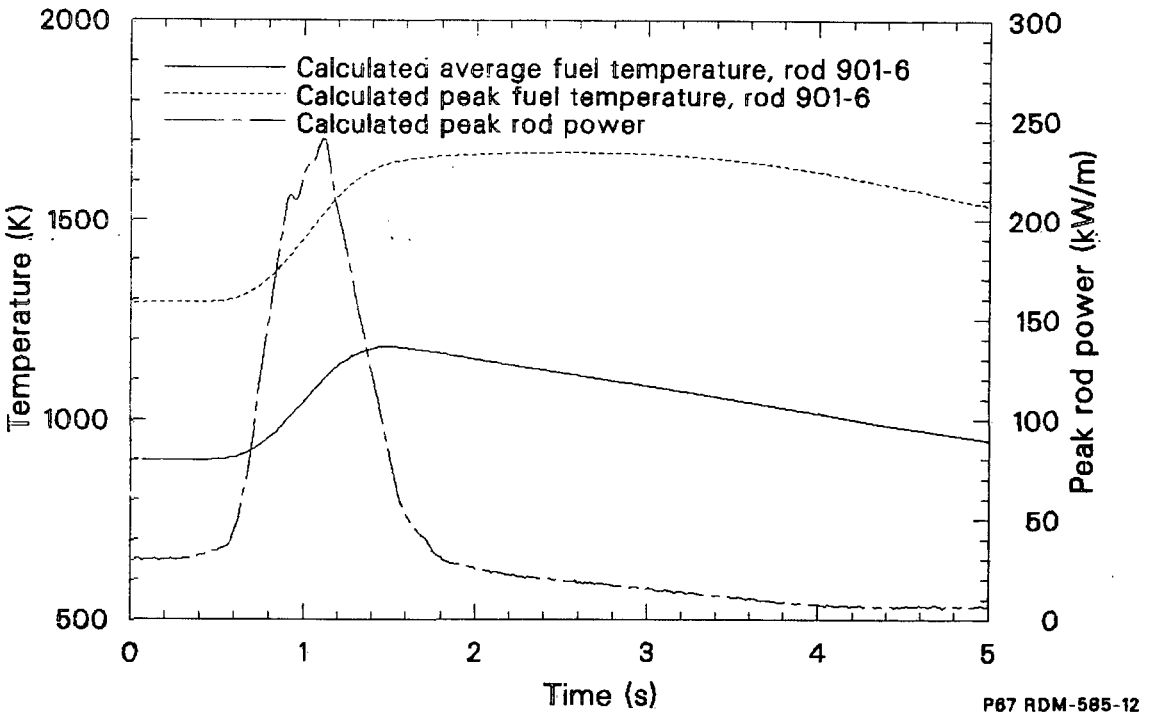

Figure 23. Calculated average and peak fuel temperatures, Rod 901-6 during OPTRAN 1-1C.

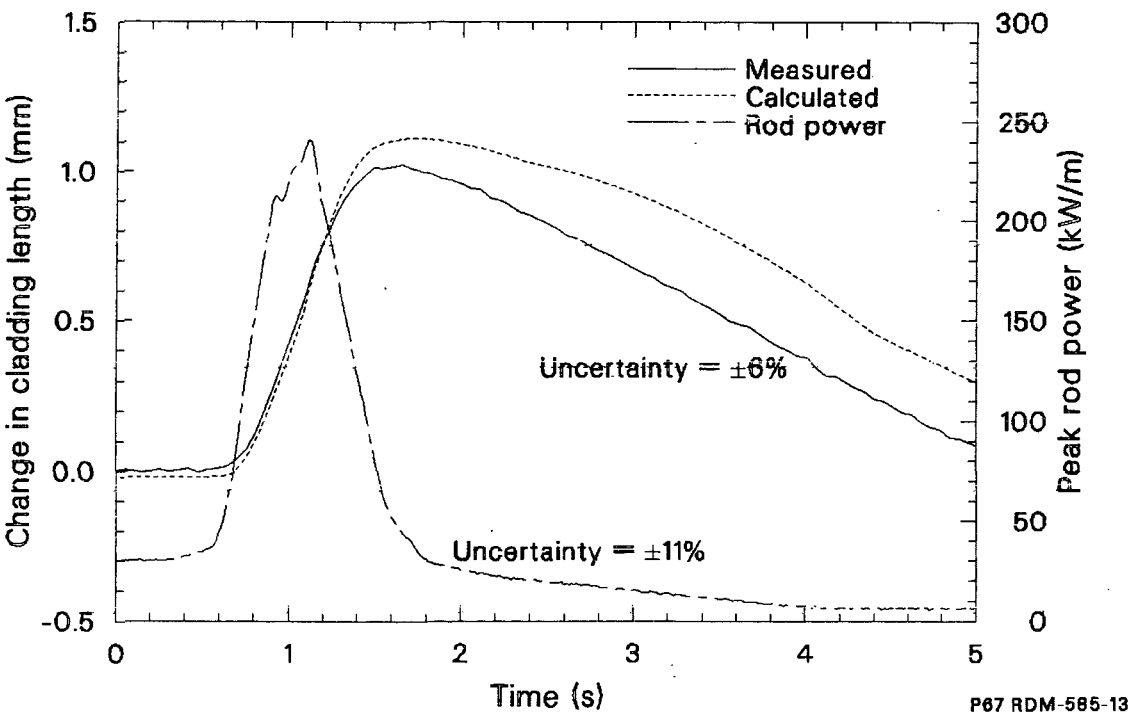

Figure 24. Comparison of measured and calculated cladding elongation with fuel rod power, Rod 901-6 during OPTRAN 1-1C.

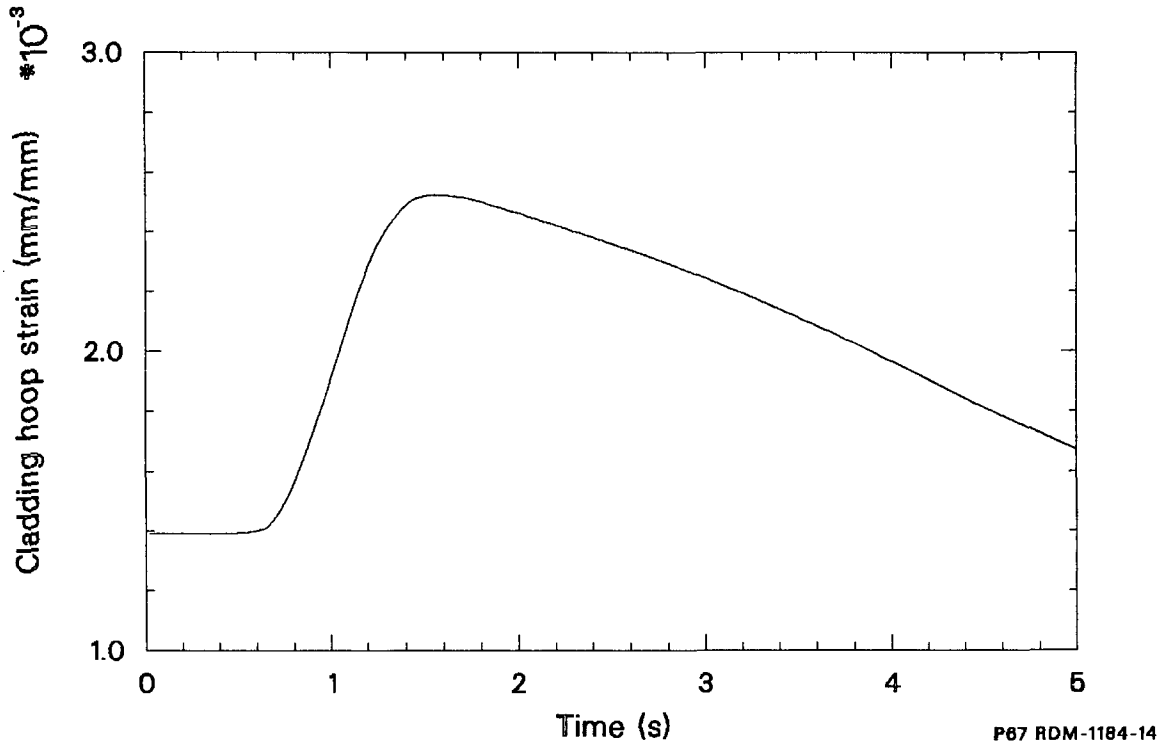

Figure 25. Calculated maximum cladding hoop strain versus time, Rod 901-6 during OPTRAN 1-1.

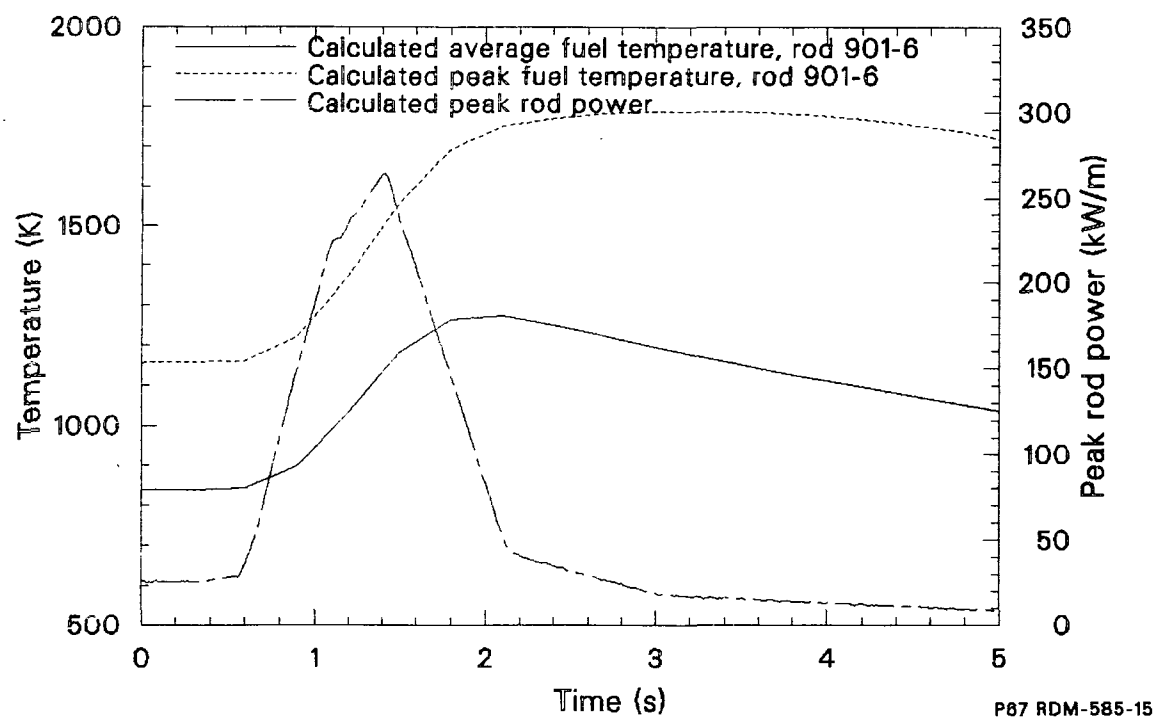

Figure 26. Calculated average and peak fuel temperatures, Rod 901-6 during OPTRAN 1-1D.

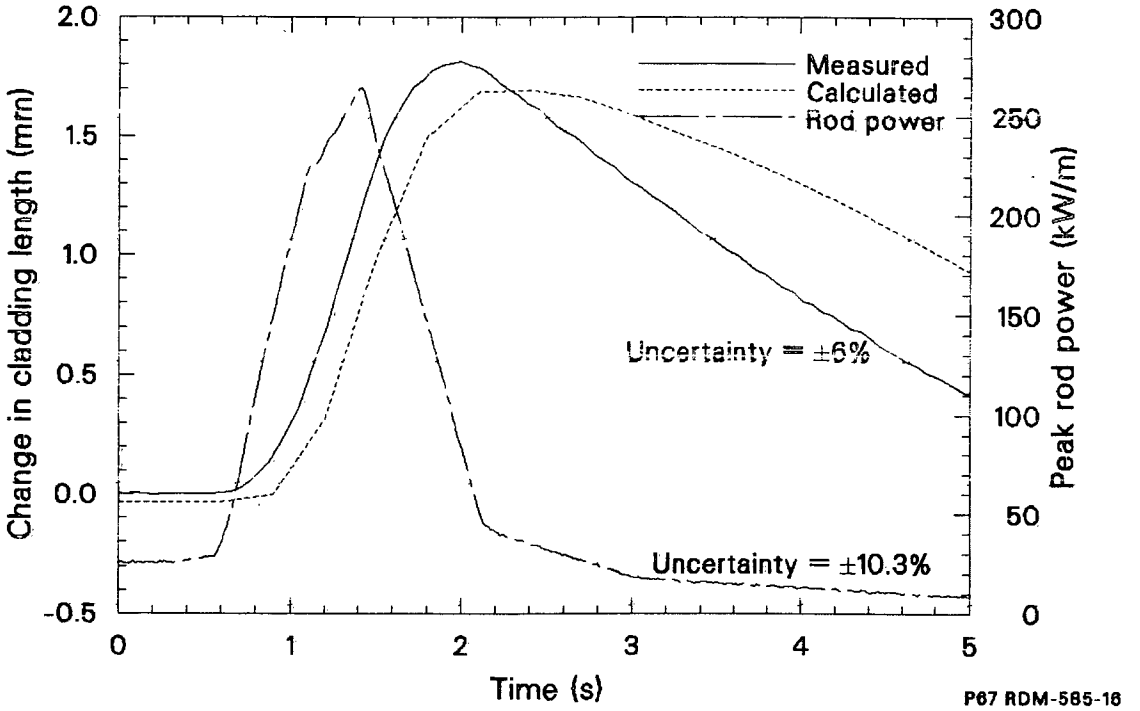

Figure 27. Comparison of measured and calculated cladding elongation with fuel rod power, Rod 901-6 during OPTRAN 1-1D.

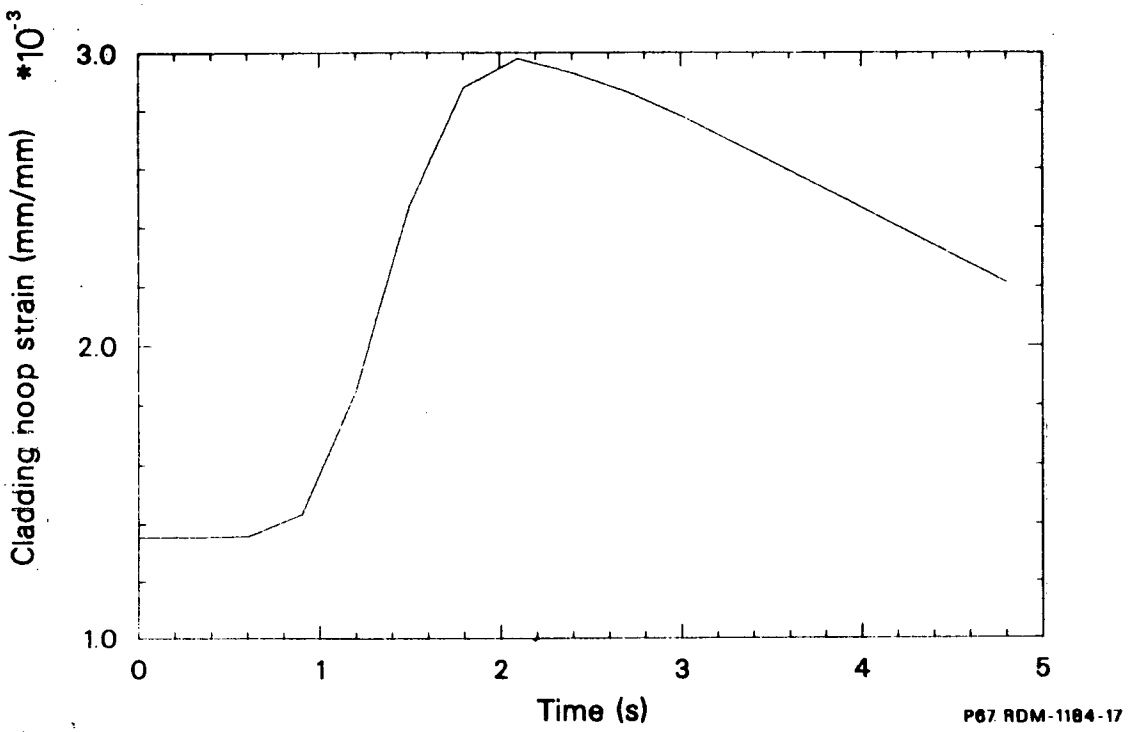

Figure 28. Calculated maximum cladding hoop strain versus time, Rod 901-6 during OPTRAN 1-1D.

period when Rod 901-6 was subjected to Transient D. The maximum fuel centerline temperature was 1789 K at 3.2 s and it lagged maximum power by 1.8 s. Film boiling was not predicted to occur. The maximum calculated cladding surface temperature was 590 K.

Calculations indicate that Rod 901-6 experienced axial and radial PCIs simultaneously at 1.2 s during Transient D. The comparison between computed and measured relative cladding elongation is shown in Figure 27. The calculated results indicate that the cladding elongation increased at the rate of 1.381 mm/s while the corresponding measured result was 1.91 mm/s. The maximum relative calculated elongation was 1.73 mm at 2.4 s, while the corresponding measured result was 1.81 mm at 1.9 s. The calculated rate of decrease in cladding elongation was 0.31 mm/s, while the measured result was 0.47 mm/s. The calculated axial PCI release time did not agree with the measured value of 6 s.

The central three nodes were calculated to experience radial PCI. The maximum calculated hoop strains were experienced at Node 3 as illustrated in Figure 28. The maximum calculated hoop strain was 0.30% at 2.0 s. The calculated maximum permanent cladding hoop strain was 1.41 10^{-4}% at Node 3. The maximum calculated hoop stress was 188 MPa.

FRAP-T6 Calculations for Rod 902-4. Rod 902-4 was subjected to the power pulse shown in Figure 12 that simulated a closure of the main steam isolation valve without scram in a boiling water reactor. The calculated peak rod power increased from 26.90 kW/m to 294 kW/m in the first 2.7 s. Then, in the following 0.7 s, it dropped to 50 kW/m. The peak fuel rod power in the FRAP-T6 analysis was slightly lower than that in the test because no axial node was located at the elevation of the largest axial power ratio.

The results of the posttest analysis of Rod 902-4 are presented in Figures 29 through 32 and summarized in Table 6. Figure 29 shows the FRAP-T6 calculations for the average and the maximum fuel centerline temperature and rod power for Rod 902-4. The peak rod power at 0.0 s was 26.90 kW/m and the corresponding maximum calculated fuel centerline temperature was 1257.0 K. The maximum fuel centerline temperature was 2070.4 K at 5.21 s and it lagged maximum power by 2.51 s.

The experimental observations regarding the axial and radial PCIs indicate that an axial PCI took place earlier (i.e., at lower power) than radial PCI, and it took place at ∿1 s. In addition, the preconditioning was performed at a power too low to eliminate pellet eccentricity. Thus, the causes of an early axial PCI were not eliminated before the transient test began. Based on the test results, values for the variable DIFGAP were specified such that the calculated axial PCI would take place at all the axial nodes simultaneously at 1 s.

The high-temperature PCI capability of the FRACAS-II subcode was used because Rod 902-4 experienced film boiling during OPTRAN 1-2 experiment.

The comparison of the measured and calculated cladding temperatures is shown in Figure 30. The thermocouples at 546 and 646 mm on Rod 902-4 did not indicate boiling transition occurrence, while the thermocouple at 446 mm did indicate boiling transition occurrence. The FRAP-T6 calculations indicate that boiling transition occurred from the 167-to 420-mm elevation and from the 669- to the 753-mm elevation on Rod 902-4. The maximum calculated cladding outside temperature was 958 K at the 293.0-mm elevation. The maximum measured cladding outside surface temperature at the 446-mm elevation was 940 K. The calculated maximum inside cladding surface temperature was 1007 K at the 293-mm elevation at 4.0 s. The measured and calculated cladding temperatures are in good agreement.

Figure 31 shows a comparison of calculated and measured relative cladding elongation versus time during the first 10.0 s of the transient. The calculated results indicate that the maximum relative cladding elongation was equal to 4.76 mm, compared with a measured elongation of 5.6 mm. The maximum measured relative cladding elongation is 18% greater than the corresponding FRAP-T6 calculation.

The calculated results indicate that Rod 902-4 may have experienced radial PCI at axial Node 4 at 2.0 s and radial PCI at the first seven axial nodes by 3.00 s. The maximum hoop strains occurred at axial Node 4 and are shown in Figure 32. The maximum hoop strain was 0.269% at 2.78 s. The maximum calculated hoop stress was 110.2 MPa at axial Node 3. The calculated permanent hoop strain remained negative at all the axial nodes.

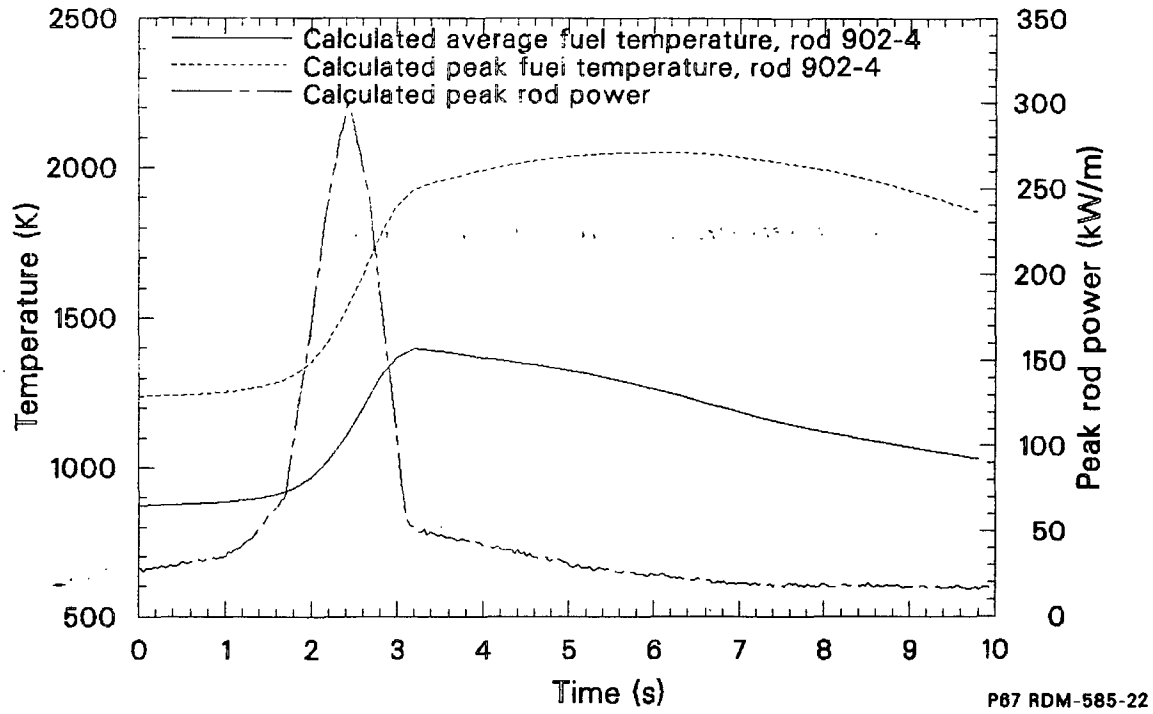

Figure 29. Calculated average and peak fuel temperatures and rod power for Rod 902-4, during OPTRAN 1-2.

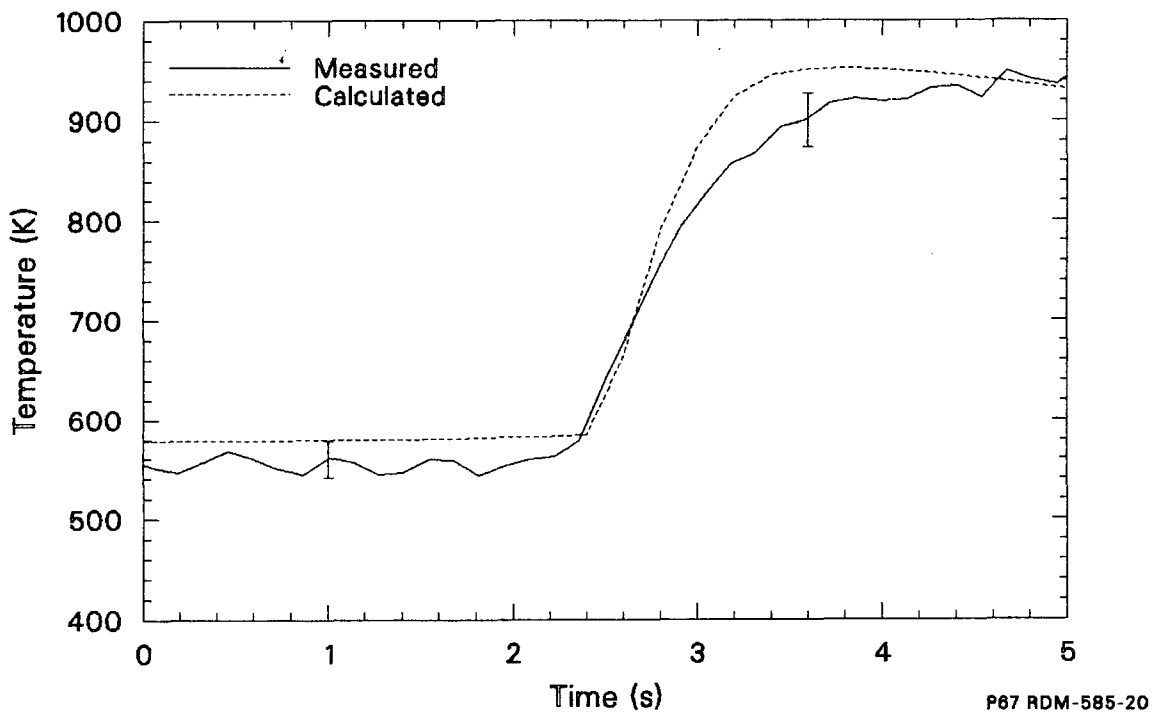

Figure 30. Comparison of measured and calculated cladding temperatures, Rod 902-4 during OPTRAN 1-2.

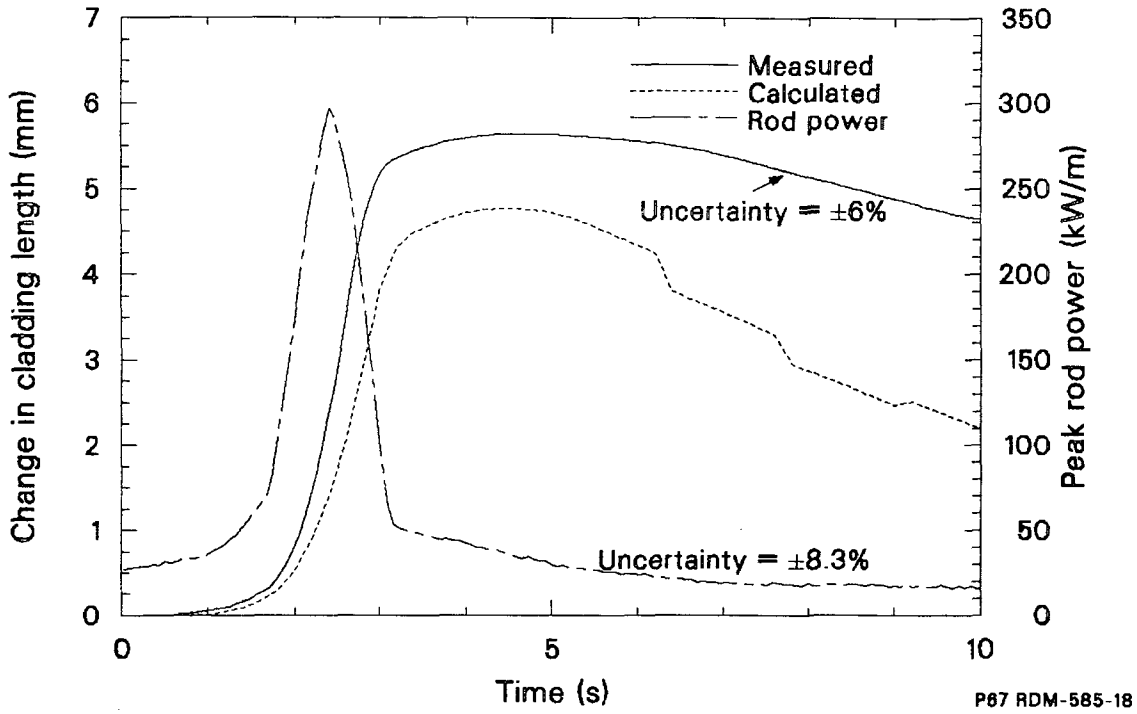

Figure 31. Comparison of measured and calculated cladding elongation with peak rod power, Rod 902-4 during OPTRAN 1-2.

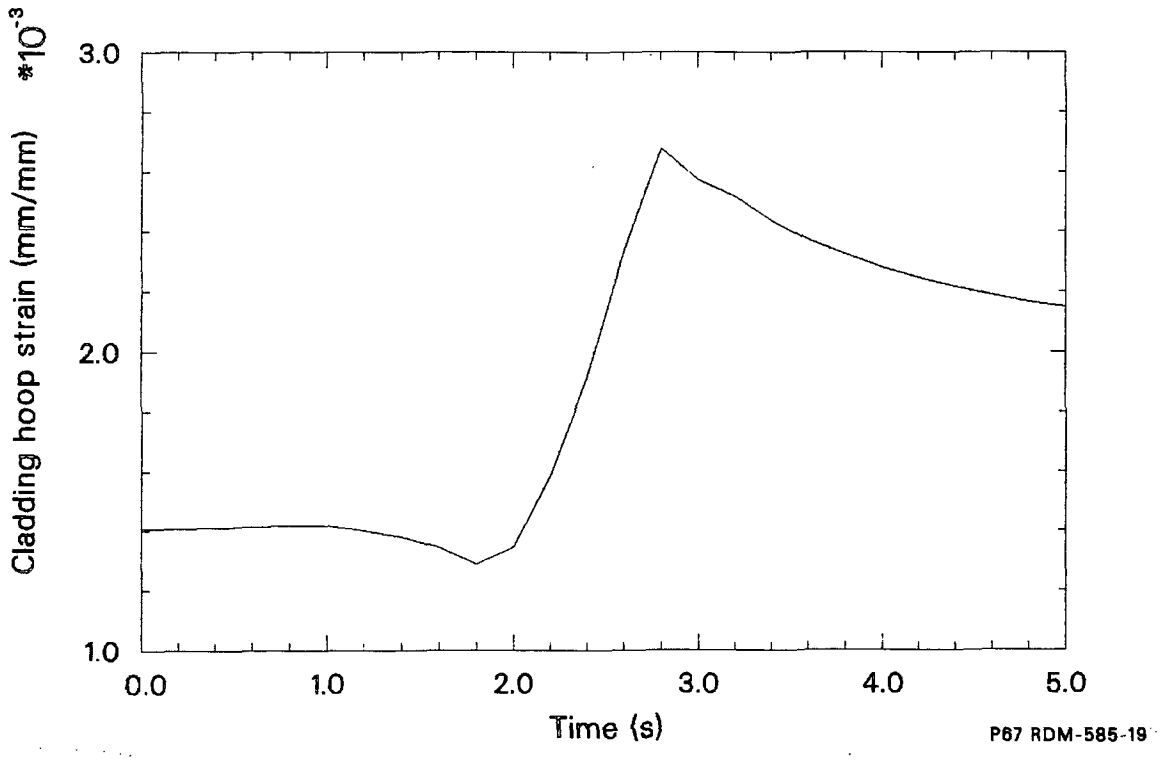

Figure 32. Calculated maximum cladding hoop strains versus time, Rod 902-4 during OPTRAN 1-2.

Discussion of Calculated Results

The posttest calculations indicate that the initial conditions established by the steady-state irradiation and preconditioning play important roles in cladding deformation during transients. Results from the transient analysis (FRAP-T6) can be explained by reviewing the results for the prior steady-state analysis (FRAPCON-2). The steady-state irradiation of the fuel rods in the Monticello reactor was performed at low power so the fuel experienced a small amount of swelling. In addition, the amount of fission products accumulated on the grain boundaries was small. The fuel densified during the Monticello irradiation and then experienced additional densification during the PBF preconditioning because its temperatures during preconditioning were higher than those during steady state. The total densification was larger than the swelling experienced by the fuel. In addition, the cladding experienced very little creepdown during the steady-state irradiation. Therefore, at the end of the steady state irradiation and preconditioning, the gap between the cladding and fuel was larger than the as-fabricated gap. This gap was larger in Rod 902-4 than in Rod 901-6 , because the fuel in Rod 902-4 experienced a smaller amount of swelling. Therefore, during transient analysis Rod 901-6 experienced higher cladding hoop stress than that experienced by the Rod 902-4.

The initial steady-state power at the beginning of an anticipated transient is important in PCI analysis. This is illustrated by the observation that although Rods 901-1 and 901-6 had the same amount of burnup, Rod 901-1 did not experience radial PCI while Rod 901-6 did experience radial PCI. At the beginning of the transient, Rod 901-1 was subjected to the lower steady-state peak power (23.82 kW/m) while Rod 901-6 was subjected to the higher steady-state peak power (30.74 kW/m). Therefore, Rod 901-6 experienced higher fuel centerline temperature than that experienced by Rod 901-1 at the beginning of transient. In fact, the fuel centerline temperature experienced by Rod 901-6 at 0 s was higher that that experienced by Rod 901-1 during the whole transient.

The comparison of cladding elongation shows the calculated magnitudes of the maximum relative cladding elongation are within 22% of the corresponding measurements. The calculated times for the maximum relative cladding elongation taking place are within 26% of the corresponding measurements. This comparison of cladding elongations indicates that an early axial PCI model is essential in calculating cladding deformation during initial PCIs.

Rod 901-6 experienced the maximum calculated hoop stress of 188 MPa during Transient D. Because this hoop stress was present for less than a second, it was not likely to have caused any PCI cracks. The maximum hoop stresses in other test rods were lower than 188 MPa. Therefore, PCI cracks would not be expected in any of the test rods.

POSTIRRADIATION EXAMINATION RESULTS

As discussed earlier, the primary objective for the OPTRAN 1-1 and 1-2 tests was to determine the extents of fuel rod damage from transient phenomena. Because no test rods failed and because rod instrumentation was limited by the necessity of preserving internal chemistries, the majority of damage information had to be provided by postirradiation examinations (PIE). The hot cell techniques used included pulsed-eddy-current scanning for cladding cracks and rod diameter changes, gross and spectral gamma scans for fission product distributions, composition analyses on extracted gap/plenum gases, fuel burnup measurements, flattening of cladding clamshell segments to expose any incipient cracks, fractographic investigations by scanning electron microscope, and determinations of cladding deformation and phase transformations by metallography.

Any fuel rod damage which may have occurred during the OPTRAN tests was probably due to PCI, both mechanical and chemical in nature. When fuel pellets expand thermally in response to large power surges, gap closure can occur and large hoop stresses can be imposed upon the adjacent cladding. If sufficient amounts of chemically aggressive fission products are simultaneously released from the UO_2 matrix, stress-corrosion cracking is thought to initiate fractures on interior cladding surfaces. Therefore, the PIE of OPTRAN fuel rods was heavily weighted toward detecting and characterizing small cladding defects.

This section presents the significant information produced by the posttest investigations. Detailed descriptions of the remote methods and a more comprehensive treatment of the findings are contained in Appendix E. Although OPTRAN 1-1 and 1-2 simulated considerably different transient scenarios, the PIE techniques employed were essentially identical and all eight test rods were examined as a single group. The PIE results are reported in a task format, rather than by test, in order to convey an appreciation for the respective transient severities.

Visual Inspections

After transient testing, the shrouded OPTRAN fuel rods were transported to hot cells, extracted from their flow shrouds, and given a prompt photovisual survey. The external surfaces of the OPTRAN 1-1 rods had many marks from bundle disassembly following irradiation in the Monticello BWR and from handling in preparation for PBF testing. However, these rods showed no signs of exposure to severe power excursions. In particular, the rods withdrawn after the relatively mild OPTRAN 1-1A transient (901-1 and 901-3) were indistinguishable from the four rods in place for the last three power spikes. Moreover, no unusual features were observed on the pressurized developmental rods (901-2 and 901-4) that experienced all four OPTRAN 1-1 transients.

By contrast, the OPTRAN 1-2 test rods displayed one distinct difference from their pretest appearances. Rods 902-2 and 902-4 were found to have bowed over most of their 75-cm fueled lengths, as shown on Figures 33 and 34. The data from functional cladding surface thermocouples demonstrate that a boiling transition occurred on both rods during OPTRAN 1-2, and bowing can be caused by asymmetrical dryout around a rod circumference. However, metallographic results discussed later in this section indicate that film boiling was restricted to upper rod portions only. Therefore, much of the observed bowing cannot be attributed to transient coolant behavior.

In addition, all eight OPTRAN rods were systematically examined for PCI X-marks—Lüders bands that converge as cracks propagated by hoop stresses penetrate cladding walls. No obvious candidates were spotted, but two locations on Rod 901-3 were further evaluated for complete assurance. As expected, metallography confirmed that these somewhat suspicious indications were merely abrasion marks.

Pulsed-Eddy-Current Investigations

The second phase of the nondestructive PIE was to check the OPTRAN fuel rods for cladding cracks and wall thickness variations from PCI-induced damage. Each rod was scanned at 5-degree circumferential increments with a conventional driver/dual pickup eddy-current coil arrangement. However, square-wave excitation pulses (1 kHz) are

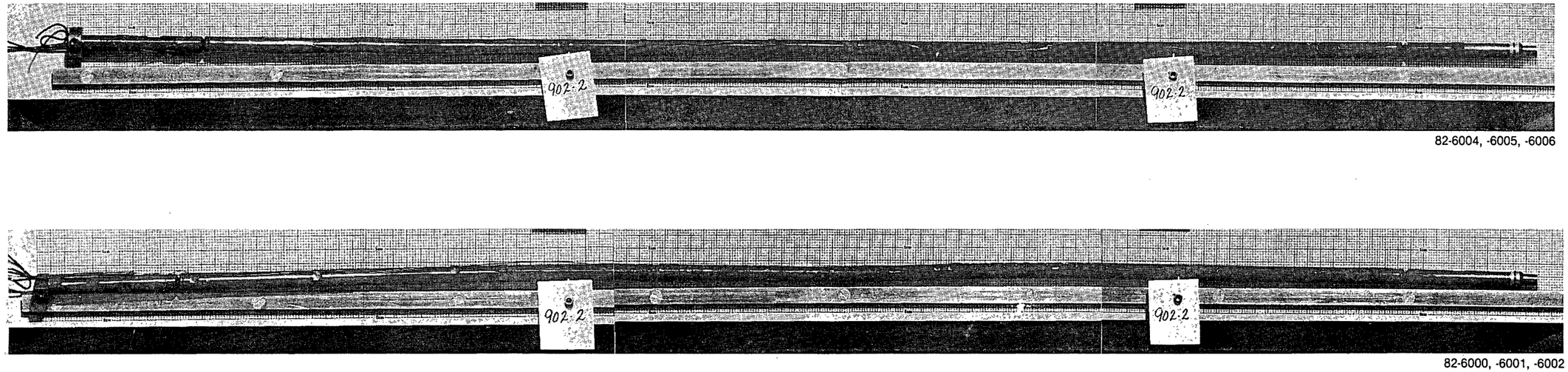

82-6004, -6005, -6006

82-6000, -6001, -6002

INEL 4 1029

Figure 33. Bowing on OPTRAN 1-2 Rod 902-2, as viewed from the 0-degree (top) and 130-degree orientations.

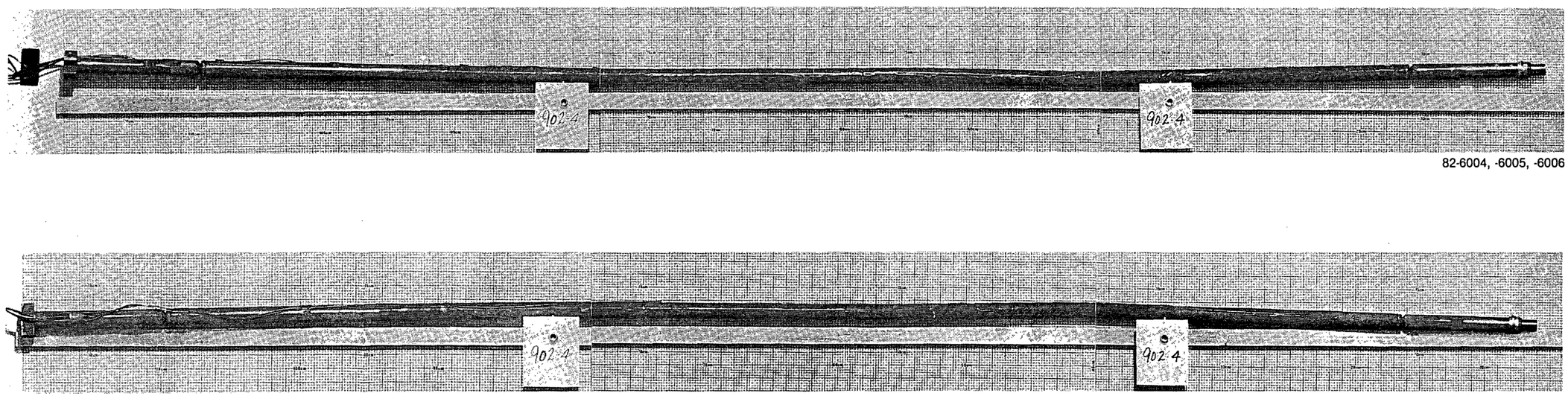

82-6004, -6005, -6006

82-6000, -6001, -6002

Figure 34. Bowing on OPTRAN 1-2 Rod 902-4, as viewed from the 315-degree (top) and 180-degree orientations.

INEL 4 1030

used on this system instead of the standard continuous sinusoidal driver wave at a tunable discrete frequency. Due to the spread of frequency components within the square wave, the pulsed eddy current (PEC) approach is simultaneously sensitive to a wide variety of defect types. The detection threshold for cladding cracks is <10% of the 0.86-mm wall thickness, as discussed in Appendix E.

No incipient cracks propagating from interior cladding surfaces were found on the seven OPTRAN rods scanned. (Unfortunately, Rod 902-4 was bowed too much to fit the PEC scanner fixture.) Furthermore, the PEC chart recordings registered no periodic defect signals at pellet-length intervals, so the fuel thermal expansion that tends to concentrate stresses on cladding near pellet interfaces apparently created no permanent hoop strains (ridges). Similarly, the absence of pellet-spaced defect signals from Rod 902-2 confirmed visual impressions that no waisting of ductile cladding into interfacial gaps took place during the high-temperature boiling transition phase of OPTRAN 1-2.

The PEC apparatus also contains opposing LVDTs for rod diameter and bowing information, which confirmed the lack of ridging on the OPTRAN 1-1 rods. The LVDTs should also have provided data on two-point buckling or uniform circumferential collapse where dryout had occurred on the OPTRAN 1-2 rods. However, failure of one LVDT early in the scanning of Rod 902-2 and the inability to mount Rod 902-4 prevented obtaining meaningful assessments on these two types of cladding deformation.

Gamma Scans

Gross and spectral gamma activities were measured on all eight OPTRAN fuel rods. Gross (total count) scans were performed first, and the profiles generally reflected the axial positions of the rods within the Monticello segmented assemblies. (See Appendix E.) The gross profiles were primarily used to set rod elevations at which isotopic information was subsequently extracted. The measured ^{95}Zr, ^{95}Nb, ^{103}Ru, ^{131}I, ^{140}Ba, and ^{140}La signals were primarily from the brief PBF preconditioning period; ^{134}Cs, ^{137}Cs, and ^{154}Eu were almost totally created during commercial irradiation; and ^{106}Rh and ^{144}Pr were due to neutron flux from both reactors.

The most important fission products with respect to stress-corrosion cracking are iodine and cesium. Iodine is widely believed to be the main corrosive agent, and it is likely to be released from UO_2 as cesium iodide—especially when the fuel has acquired significant burnup. Therefore, axial migration of these volatile species during the OPTRAN power excursions would indicate that iodine was potentially available in the gaps for attack of highly stressed cladding. (Note that such findings would not necessarily mean that the iodine was in a chemically reactive form.) However, information on axial fission product relocation cannot be directly obtained from the axial concentration profile for each radionuclide. Instead, each plot of interest must be normalized to the distribution of a stable, nonmigratory fission product with a similar half-life.

The measured ^{131}I activity at each axial position was divided by the corresponding ^{95}Zr count. Both are short-lived radionuclides due exclusively to PBF irradiation, and the zirconium is generally stable within a UO_2 matrix under relatively mild transient conditions. The plots from five OPTRAN 1-1 rods generated by this normalization process are displayed in Figure 35. Their overall flat shapes mean that no appreciable axial migration of iodine occurred with respect to the PBF power profile during OPTRAN 1-1. Regrettably, the ^{131}I within the two OPTRAN 1-2 rods had decayed beyond detectability before isotopic spectra could be taken.

An altogether different result was attained by normalizing the ^{137}Cs profiles to ^{154}Eu, a fission product particularly resistant to relocation. As shown by Figure 36, this long-lived cesium isotope (30-year half-life) has migrated toward whichever was the cooler end of each segment in the Monticello BWR. (Rods 901-1, -3, -5, and -6 were bottom segments while Rods 902-2 and 902-4 occupied the topmost position.) Because the PBF neutron flux was symmetric about each fuel stack midpoint, these findings suggest a long-term migration in Monticello rather than any transient effect in PBF. This hypothesis is further supported by Figure 37, where the relatively recent ^{134}Cs concentrations (two-year half-life) have been normalized to the same ^{154}Eu counts. Thus, virtually none of the cesium created late during commercial irradiation has moved with respect to the Monticello flux profile.

When viewed together, the normalized gamma activity measurements indicate that no axial migration

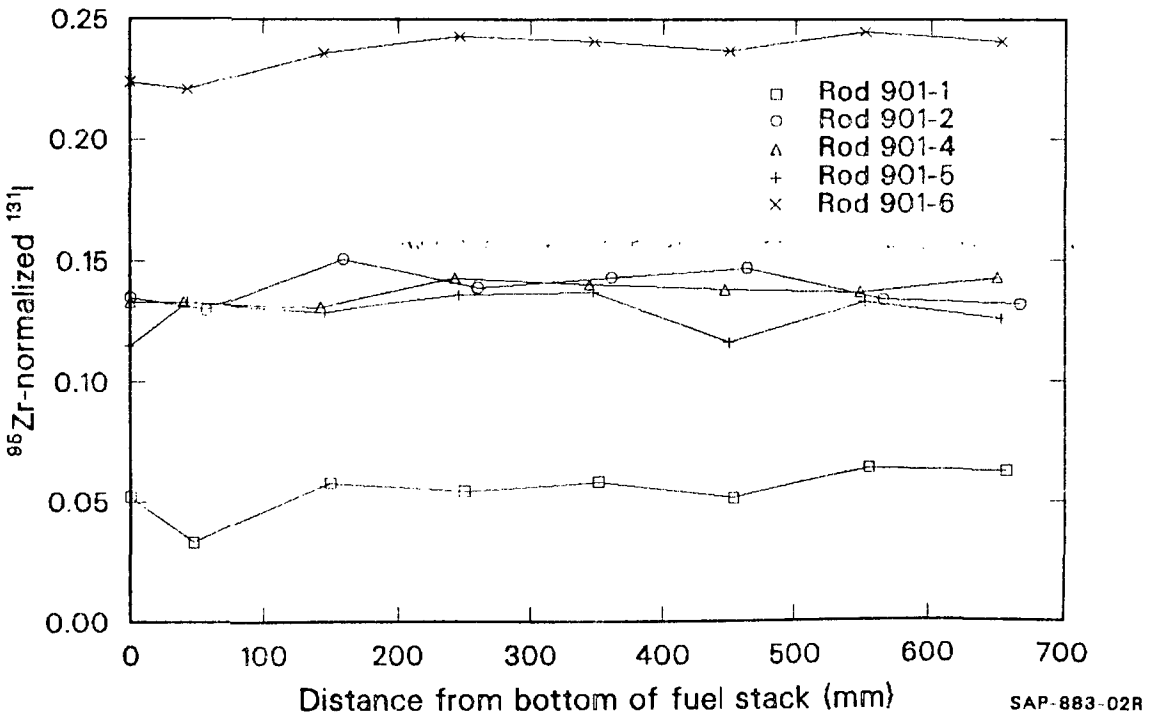

Figure 35. Normalized iodine distributions within OPTRAN 1-1 fuel rods.

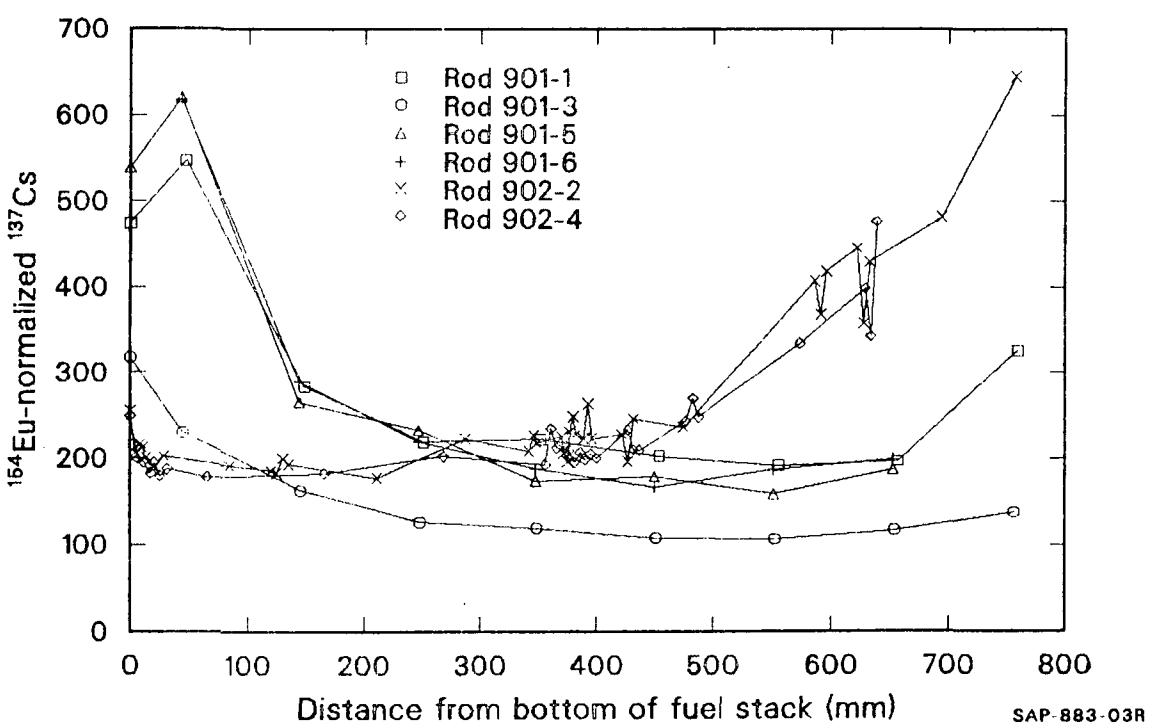

Figure 36. Normalized ^{137}Cs (30-year half-life) distributions within OPTRAN fuel rods.

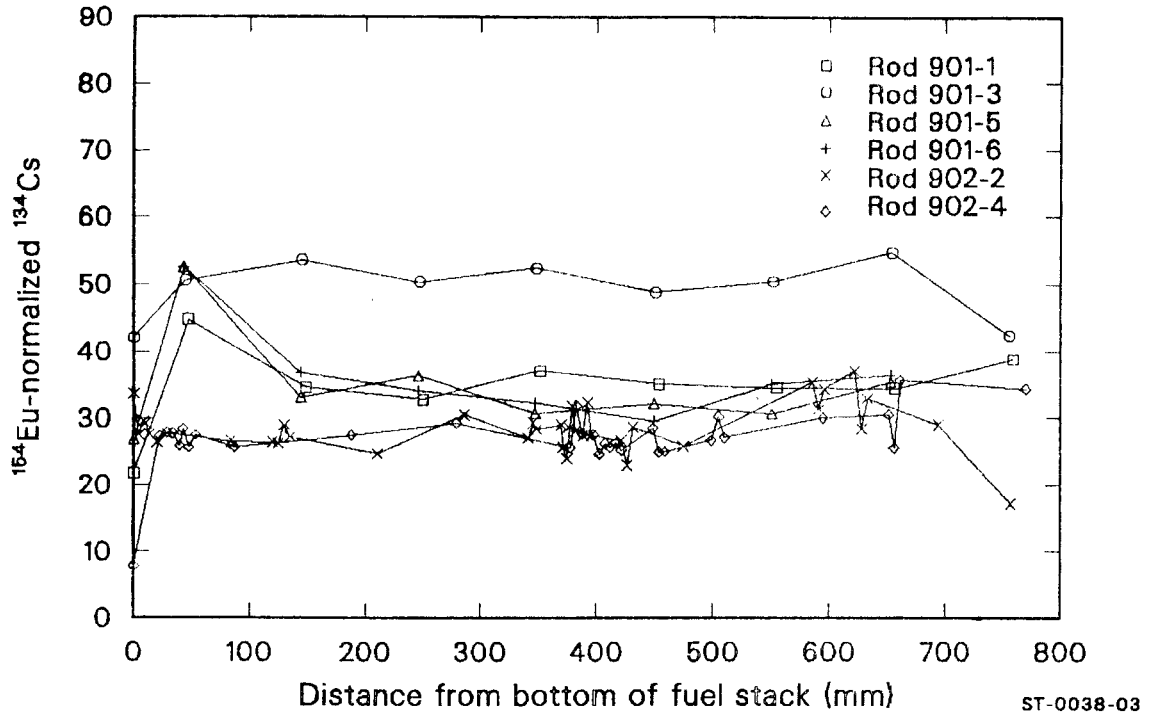

Figure 37. Normalized ^{134}Cs (two-year half-life) distributions within OPTRAN rods.

of cesium and iodine occurred as a consequence of the OPTRAN power spikes. Nevertheless, transient release and radial redistribution of fission products cannot be discounted from these results. Iodine freed from the UO_2 lattice could have reached the gaps and reacted with cladding without moving along the rods, which would not be detected by axially oriented gamma-measurement methods.

Rod Gas Determinations

Gases occupying the gap/plenum regions of each OPTRAN fuel rod were withdrawn for composition and volumetric analyses. The mixture was predominately helium fill gas in all cases, but varying amounts of inert fission gases were also extracted. These measurements and important quantities derived from them are presented in Table 7. Details on calculational methods and related assumptions are contained in Appendix E.

The values in the "inventory released" column of Table 7 correlate quite well with transient exposure. The smallest release percentages were measured on Rods 901-1 and 901-3, which experienced only the mild OPTRAN 1-1A excursion. (Note that much of the fission gas extracted from these two rods can be explained by fission fragment recoil and knockout during steady-state operation.) Meanwhile, Rods 901-5 and 901-6, in place for the last three OPTRAN 1-1 transients, show similar release values to Rods 901-2 and 901-4, which remained in PBF for all four power spikes. OPTRAN 1-2 was apparently much more severe in terms of transient duration and peak fuel temperatures, since percentage releases for Rods 902-2 and 902-4 were nearly an order of magnitude larger than the OPTRAN 1-1 rods.

The reader is cautioned not to apply these measured fission gas release percentages to typical commercial fuel rods undergoing similar transients. Larger portions of the OPTRAN gas inventories would certainly have escaped the fuel pellets had not the base irradiation powers been so low. As demonstrated by Table 8, the time-weighted average rod powers at the Monticello core periphery ranged between 7.8 and 12.7 kW/m, compared with a BWR 8 x 8 core-average rod power of 18 kW/m. Volume-averaged fuel temperatures during steady-state irradiation were typically 800 K for the OPTRAN rods—200 K below the average fuel temperature at 18 kW/m. Peak centerline fuel temperatures were between 900 and 1200 K in Monticello, while core-average commercial maximum temperatures are typically between 1400 and 1600 K over

Table 7. Rod gas analysis results

Rod Number	Burnup (GWd/mtu)	Void Volume (cm^3)	Total Gas Withdrawn (std. cm^3)	Atom% Kr	Atom% Xe	Total Inert Gases Released (std. cm^3)	Inventory Released (%)
901-1	12.9	14.4	13.4	0.24	1.83	0.28	0.13
901-2	5.0	13.8	37.9[a]	0.07	0.51	0.22	0.27
901-3	21.9	13.8	13.4	0.33	2.79	0.42	0.11
901-4	5.1	14.1	35.1[a]	0.15	0.78	0.33	0.39
901-5	11.6	13.7	13.3	0.53	4.14	0.62	0.32
901-6	13.1	13.3	12.8	0.44	3.40	0.49	0.22
902-2	10.7	15.5	19.3	2.56	19.43	4.24	2.37
902-4	9.0	14.1	15.7	1.94	14.84	2.63	1.75

a. Pressurized rod designs.

Table 8. OPTRAN base power/temperature histories[a]

Rod Number	Irradiation Time (days)	Time-Weighted Average Rod Power (kW/m)	Volume-Averaged Fuel Temperature (K)	Peak Centerline Fuel Temperature (K)	Burnup (GWd/mtu)
901-1	1101	11.0	825	1080	12.8
901-2	327	12.4	855	1150	5.0
901-3	1891	10.2	800	1025	21.9
901-4	327	12.7	860	1165	5.1
901-5	1101	9.9	790	1015	11.6
901-6	1101	11.2	820	1075	13.1
902-2	1101	9.2	775	970	10.7
902-4	1101	7.8	745	895	9.1

a. Power histories were supplied by GE. Approximate fuel temperatures were interpolated from FRAPCON II code calculations for Rods 901-1, 901-6, and 902-4.

a rod lifetime. (PBF preconditioning was performed at 21 to 24 kW/m, but for such short times that effects on gas release can be ignored.)

The low OPTRAN fuel temperatures slowed diffusion of fission products within UO_2 grains and prevented appreciable gas bubble accumulation at fuel grain boundaries. Formation of connected porosity and interlinked bubbles at grain faces would also have been inhibited. Thus, no matter what the burnup, there was little possibility for a burst-type release upon pellet expansion and microcracking during the sudden OPTRAN power ascensions. The fission gases first had to escape the fuel grains, which is not an instantaneous process—even at peak transient temperatures of >2000 K. OPTRAN 1-2 lasted barely long enough to achieve measurably significant release amounts with these initial conditions. Consequently, commercial fuel rods operated at or above core-average powers could be expected to release considerably larger portions of their gaseous inventories under comparable transient circumstances.

These differences in fuel temperatures and prospective gas releases could be quite important with regard to exceeding an iodine concentration threshold for stress-corrosion cracking during the OPTRAN tests. Recent modeling studies with Argonne National Laboratory's FASTGRASS code indicate that atomic iodine and cesium iodide migrate through the UO_2 matrix inside fission gas bubbles during steady-state irradiation.[23] Release fractions of these key volatile species thus correspond well with the noble gases. Transient iodine/iodide and gaseous fractional releases are also predicted to be comparable. Interlinked gas bubbles at fuel grain faces and edges provide direct release pathways and also encourage microcracking by reducing adhesion between grains.

Burnup Measurements

The measured figure of merit (ratio of test assembly power to PBF driver core power) was generally lower than expected from reactor physics estimates for each group of OPTRAN test rods. Burnup data figured prominently in these calculations, since remaining ^{235}U concentrations and neutron poisoning by fission products are essential considerations. Because GE did not feel its Monticello burnup calculations were accurate to better than ±15% at the core periphery, burnup samples were sectioned from all the OPTRAN rods to investigate this potential source of figure-of-merit error.

After each fuel sample was dissolved, aliquots were removed for counting of isotopic gamma emissions. Many fission products were detected, but calibrated ^{137}Cs concentrations were used to estimate local burnups due to the 30-year half-life and excellent counting statistics. Results tabulated in Appendix E are plotted against GE calculations on Figure 38. (Sample positions were factored into the GE values by interpolating between axial nodes.) Despite some difficulty in thoroughly homogenizing solutions before aliquot extractions and in correcting for axial migration, the observed agreement is quite good. Moreover, the data scatter is symmetrically distributed, so there is no evidence of a bias error. Therefore, the OPTRAN burnup measurements suggest that the GE calculations were highly accurate and in no way responsible for the figure-of-merit problems.

Cladding Clamshell Investigations

The primary motivation for performing the OPTRAN tests was to assess probabilities for rod failure and cladding damage during the various BWR transients simulated. Since no rods were breached during the OPTRAN 1-1 and 1-2 tests, postirradiation examinations focused on searching for and characterizing incipient cladding cracks. The standard technique for finding such defects is to cut lengths of fuel rod, split each length axially with two opposing longitudinal cladding slits, open each length for UO_2 removal (thus the term clamshelling), mechanically flatten each cladding half-section, and visually detect any interior cladding surface cracks that were widened and deepened by the flattening process.

Figure 39 shows that three clamshell specimens were extracted from each OPTRAN rod, with the exception of Rod 901-3 from which one sample was taken. Each clamshell was typically 15 cm in length, so ~60% of the fueled cladding length was examined. Furthermore, this coverage was biased toward the PBF power peak (fuel stack midpoint) where PCI crack formation was most likely, so few (if any) defects escaped discovery.

Figure 40 illustrates interior clamshell surfaces before flattening from the mid-length regions of five representative OPTRAN rods. Clamshells C-5 and C-9 display similar appearances, despite the developmental zirconium cladding liner in Rod 901-2 and proprietary fuel additive in

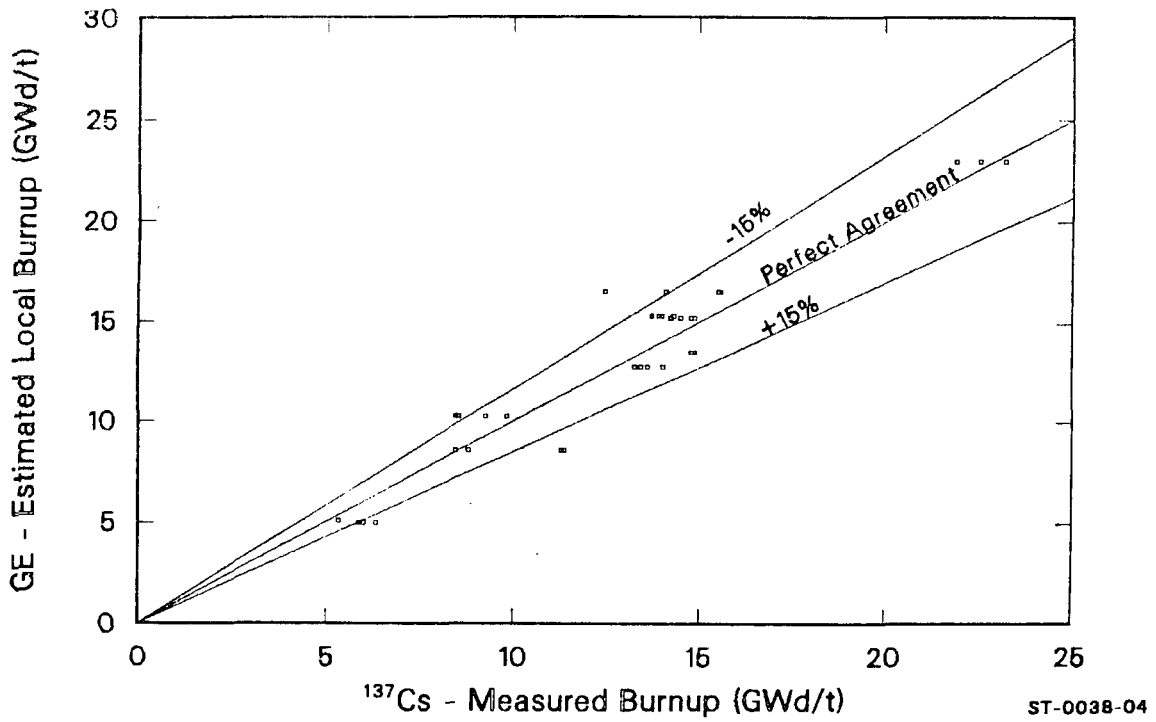

Figure 38. Confirmation of GE burnup estimations by OPTRAN sample measurements.

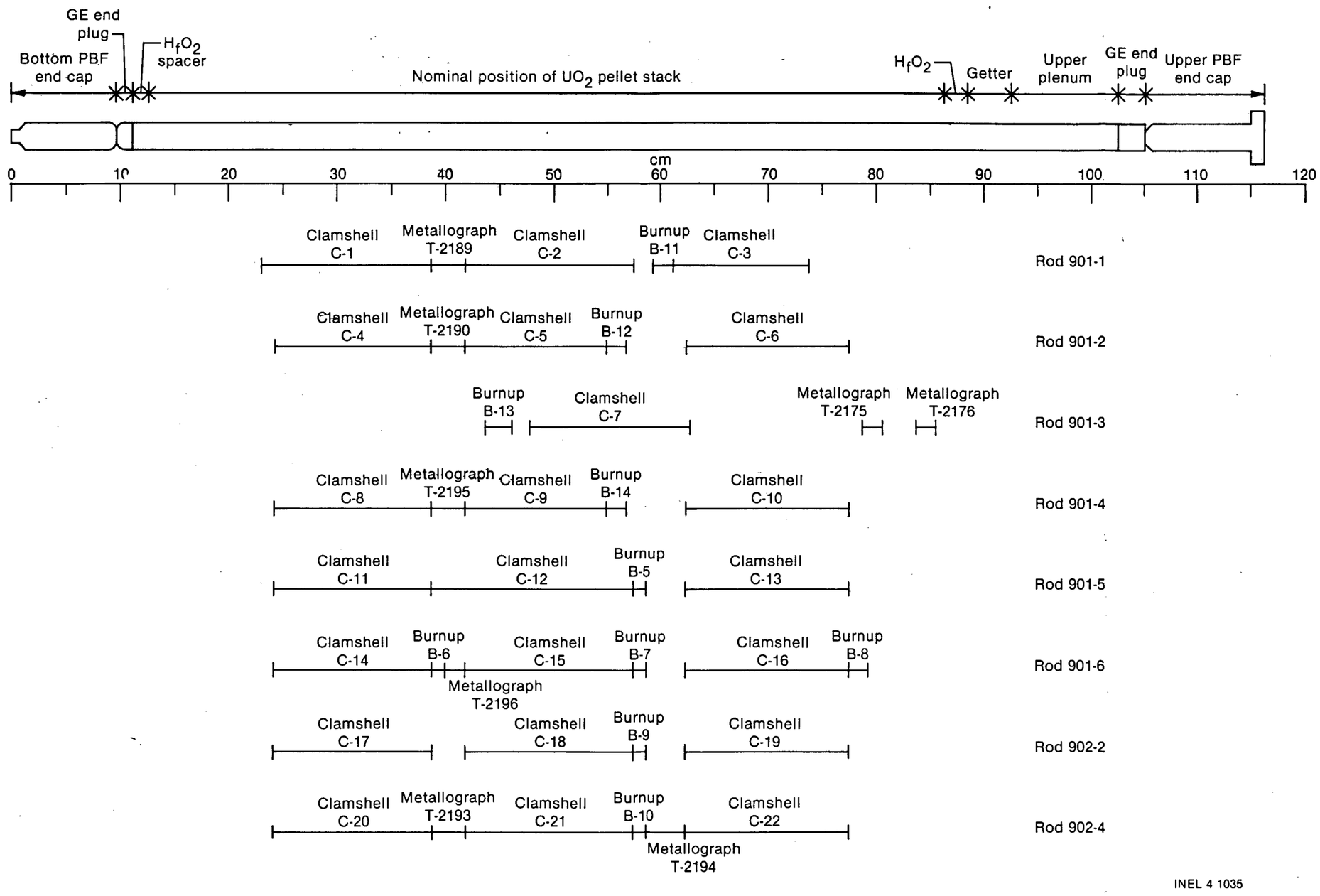

Figure 39. OPTRAN test rod configuration and sectioning locations on individual fuel rods.

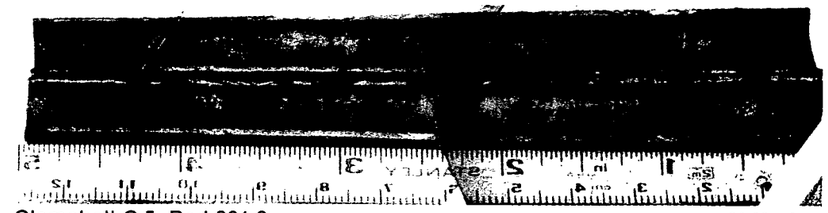

Clamshell C-5, Rod 901-2 83-39,-40,-41

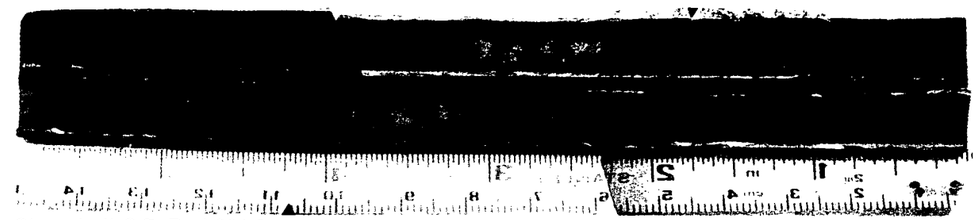

Clamshell C-7, Rod 901-3 83-56,-57,-58

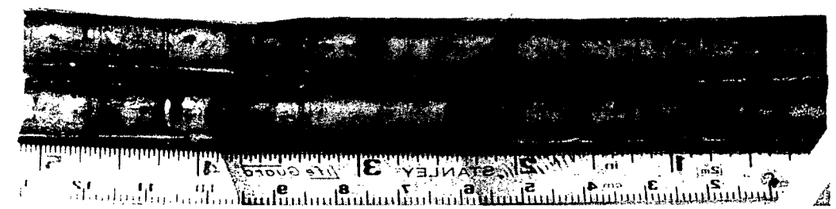

Clamshell C-9, Rod 901-4 83-71,-72,-73

Clamshell C-15, Rod 901-6 83-117,-118,-119

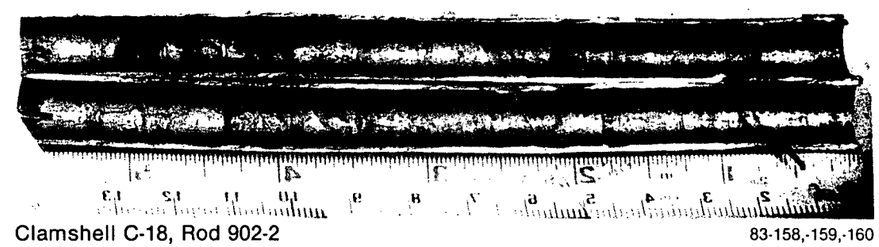

Clamshell C-18, Rod 902-2 83-158,-159,-160

INEL 4 1036

Figure 40. Preflattening appearances of interior cladding surfaces on representative clamshell specimens.

Rod 901-4, respectively. Both surfaces are generally lustrous with mottled patches and well-defined pellet interface demarcations, which is probably a consequence of the small 5-GWd/mtu burnups. By contrast, Clamshell C-7 from Rod 901-3 (22 GWd/mtu) is darkened extensively and interfacial positions cannot be distinguished. Clamshell C-15 from Rod 901-6 (13 GWd/mtu) is quite similar to C-7, but the surface is more reflective and a few pellet end locations can be resolved. Thus, the OPTRAN 1-1 specimens show changes from the initially metallic appearances that correlate well with Monticello exposure.

Alternatively, Clamshell C-18 from Rod 902-2 (11 GWd/mtu) shows distinct axially-oriented markings that may have been created during transient exposure. This type of feature was observed to varying extents on all of the OPTRAN 1-2 clamshells but not on any of the OPTRAN 1-1 specimens. These axial patterns and their concentration near the PBF power peak suggest longitudinal pellet cracks that may have opened during the OPTRAN 1-2 power excursion. If so, the dark marks are probably the residue of released fission products.

All 22 pairs of clamshell samples were flattened to enlarge any incipient cracks until detectable with the hot cell periscope. This produced no suspicious features on most specimens, but reflective indications of fresh extended fractures were found on four clamshells. As displayed on Figure 41, only Clamshell C-20 from Rod 902-4 contained an obvious crack, which was located near the bow apex at the 37-cm rod elevation (25 cm above the fuel stack base). Flattening apparently lengthened the preexisting portion to over 1 cm, per the difference in darkening between the middle and ends of the crack. Clamshell C-8 showed a similarly shaped structure 31 cm from the rod bottom, though its length was only 2 mm. Clamshells C-5 and C-9 each presented a pair of bright but shallow features after flattening at approximately the 46-cm rod elevations. They resembled superficial gouges or abrasions more than cracks, but were positioned at pellet interfaces near the PBF power peak on their respective rods—prime sites for PCI-induced defects. Consequently, these shallow anomalies could not be disregarded and were also selected for further study.

Scanning Electron Fractography

Current technology offers no ideal methods for precisely identifying PCI-induced cladding damage. The large hoop stresses and fission product releases considered by many to be essential for cladding crack initiation and propagation do not leave a unique signature. Nevertheless, brittle fracturing has been observed in connection with rod failures after commercial operation, test reactor projects, and out-of-pile simulations. Zircaloy cladding can normally accommodate hoop stresses from fuel thermal expansion by way of elastic and plastic deformation. Laboratory experiments with simulated fission products suggest, however, that cracks will nucleate on interior cladding surfaces under high stress fields in a chemically corrosive environment. Thus stress-corrosion cracking is widely felt to be the dominant mechanism in PCI-induced failures. In any case, examinations of fracture surface morphologies—commonly performed on a scanning electron microscope (SEM)—have become the primary means for classifying and characterizing PCI damage.

After flattening, each of the PCI defect candidates was punched from the clamshell where it was found. The punched sample was then bent backward in an attempt to propagate any incipient cracks through the cladding wall so that the fracture surface could be viewed directly. At least one of the mating halves was then mounted on a stage stub for SEM investigations. The preparation of the Sample C-8 SEM specimen is illustrated by Figure 42.

The postflattening cracks in Samples C-8 and C-20 concentrated stresses as expected during the bending operation, so no difficulty was encountered in extending these defects until the entire fracture surfaces were exposed. No success was achieved, however, in inducing fractures through the reflective areas on Samples C-5 and C-9. These samples were eventually fractured, but not through the defect candidates. This still allowed the specimen portions containing the desired regions to be mounted for SEM study. As detailed in Appendix E, SEM examinations of the anomalous areas and surrounding interior cladding surfaces showed only shallow gouges or abrasions that were ineffective as stress risers during flattening and bending. Thus, Samples C-5 and C-9 could no longer

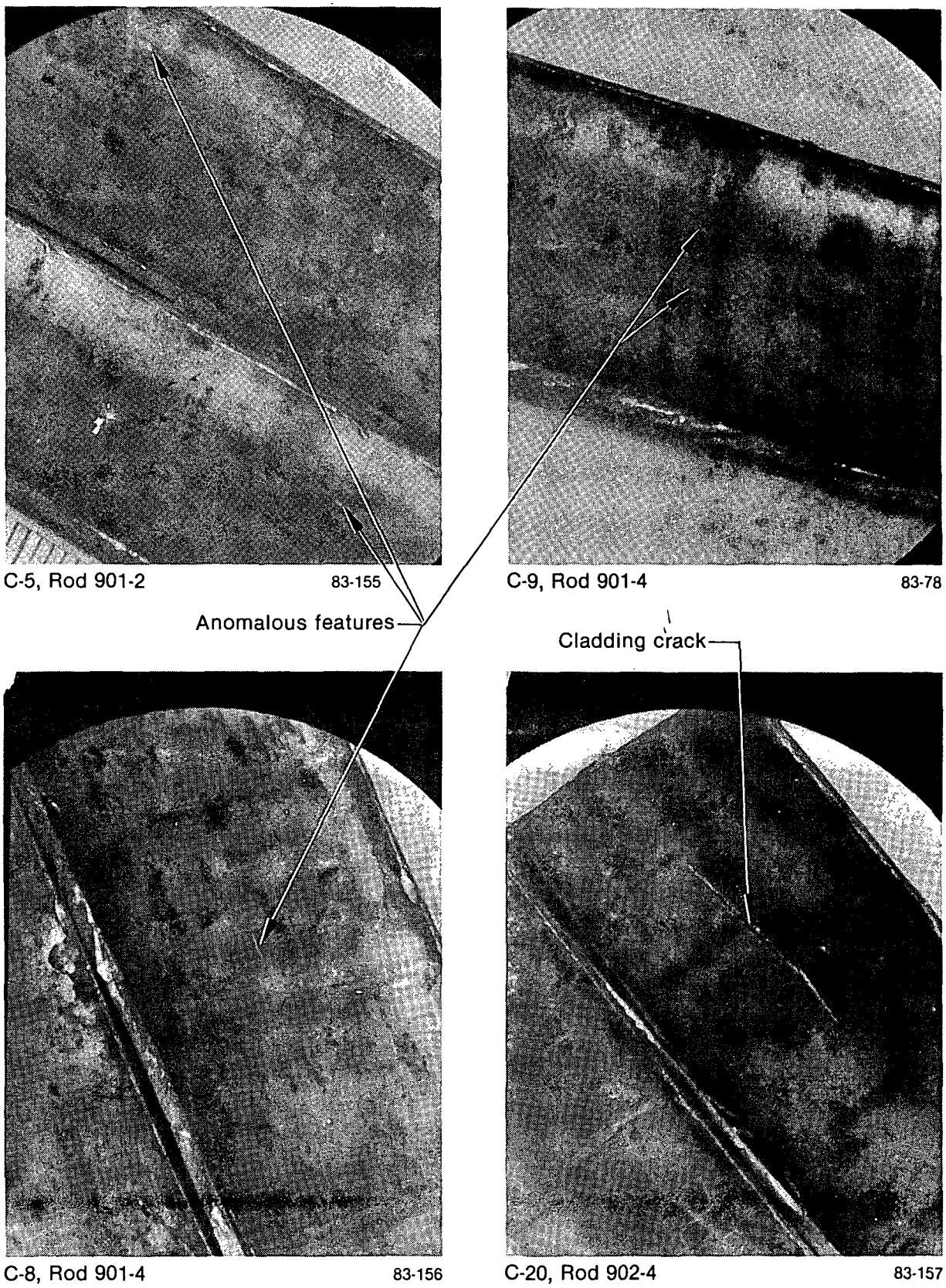

Figure 41. Interior cladding surface anomalies exposed by flattening clamshell samples.

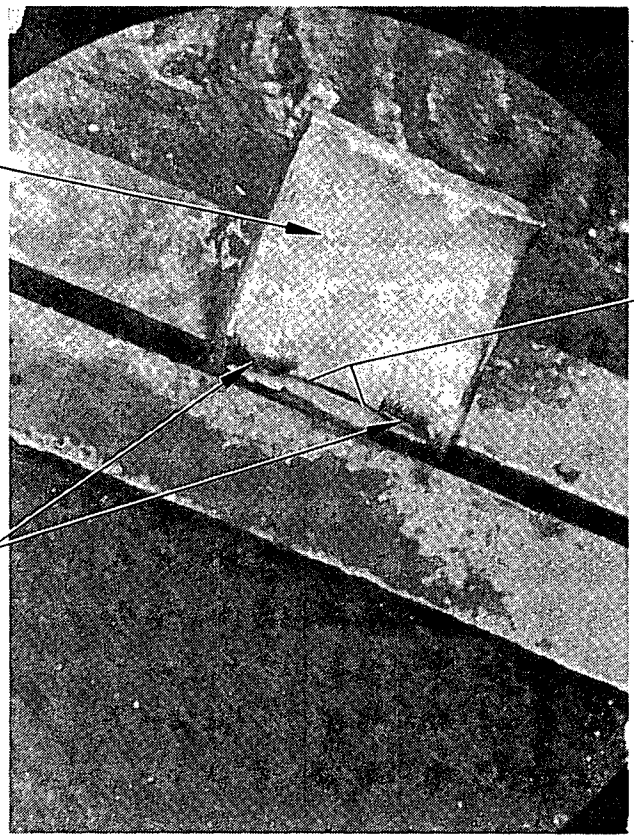

C-8, Rod 901-4 83-171

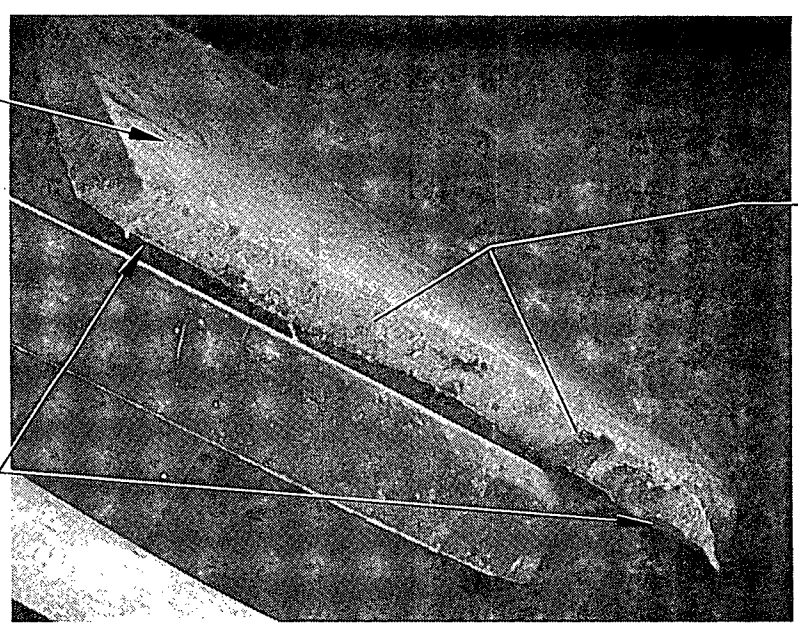

C-8, Rod 901-4 8x 83S-5

INEL 4 1038

Figure 42. Fracture surface after extension through punched Specimen C-8 (above) and after bottom half was mounted on an SEM stub.

be considered for incipient PCI cracks, and fractographic analyses were limited to C-8 and C-20.

Fractographic highlights of Sample C-8 from OPTRAN 1-1 Rod 901-4 are presented in Figure 43. Virtually all features can be readily recognized as tear ridges and dimple ruptures associated with ductile fracturing under tensile stress. No brittle inter- and transgranular fractures are evident. Moreover, the crack morphology is identical within the incipient portion exposed by flattening and over the region opened by mechanical bending.

The absence of brittle fracture signs on sample C-8 does not totally exclude incipient crack formation solely by large hoop stresses during OPTRAN 1-1. However, without corrosion-induced crack nucleation sites, the cladding should have accommodated pellet expansion stresses by uniform elastic and plastic deformation. Furthermore, it is difficult to understand how purely mechanical PCI processes could be responsible for the C-8 defect without creating a few incipient cracks elsewhere inside the OPTRAN 1-1 rods.

It is far more likely that the C-8 defect was due to flattening stresses that were not uniformly distributed. The SEM photomacrograph in Figure 43 shows a distinct inward bulge and matching exterior cladding surface depression, so the cladding may have been indented slightly at this position before flattening. In any event, there is no reason to ascribe the small C-8 crack to transient PCI phenomena.

Fractographic analysis of Sample C-20 from OPTRAN 1-2 Rod 902-4 was more difficult, because a mixture of fracture modes was observed. In the SEM photomacrograph in Figure 44, flattening of Sample C-20 propagated the crack through most of the cladding wall thickness. Here flattening stresses were almost certainly focused by a preexisting cladding discontinuity, unlike Sample C-8 where flattening seems to have only initiated the small crack. The bottom two micrographs in Figure 45 show marked differences in fracture morphology across the transition from the incipient region to the portion mechanically extended by flattening and bending. While some tear ridges and dimple ruptures are apparent throughout the upper incipient surface, these ductile features occur in considerably higher concentration below the transition. Furthermore, the incipient fracture has an appreciably softer texture than the parallel tear ridges of the extended region. The 4400X close-up fractograph in Figure 44 suggests that this texture difference is due to relatively flat transgranular facets from brittle fracturing plus cleavage feathers—tiny stair-step plateaus where the fracture direction was not precisely parallel to preferred crystallographic cleavage planes. Small particulates of unknown origin and composition are also prevalent on the preexisting crack surface.

A mixture of ductile and brittle-fracture modes is termed quasi-cleavage in failure analysis literature.[24] Regrettably, this classification provides no insights in the PCI context, nor does it explain the presence of the particulates. Many fractographic studies have been performed on failed commercial fuel rods and on test rods from both in-pile and out-of-pile experiments. Where stress-corrosion cracking could be identified as the primary damage mechanism, few (if any) signs of ductile fracturing were detected among the brittle characteristics. Cleaved cladding grains were generally flatter and more sharply defined than over the incipient region shown in Figure 46. Moreover, concentrations of particulates are not commonly reported on fracture surfaces. Therefore, while the Sample C-20 defect existed in some form before clamshell flattening, comparisons to other fractographic results do not permit assigning direct responsibility for incipient crack formation to stress-corrosion cracking and PCI during the OPTRAN 1-2 transient.

The C-20 incipient crack does not resemble typical PCI-related cladding damage in other important respects. While fuel rods have failed from PCI-induced processes at only a single location, many incipient cracks are frequently found on subsequent destructive examinations. So, had conditions been conducive to stress-corrosion cracking during OPTRAN 1-2, more than one isolated defect would have been detected inside the two test rods. In addition, the C-20 incipient crack approached 1 cm in length, which is unusually long. Although this crack was extended somewhat by flattening, PCI-induced cladding perforations generally resemble pinholes.

Despite these discrepancies, PCI and stress-corrosion cracking cannot be completely disregarded as potential causes for the C-20 defect. The existing PCI-damage data base consists almost totally of actual and simulated results from power-ascension and load-following events. Cladding stresses build slowly under these circumstances and ample time is available for enhanced fission product releases, nucleation of numerous crack sites, and crack propagation from combined stress fields and chemical corrosion.

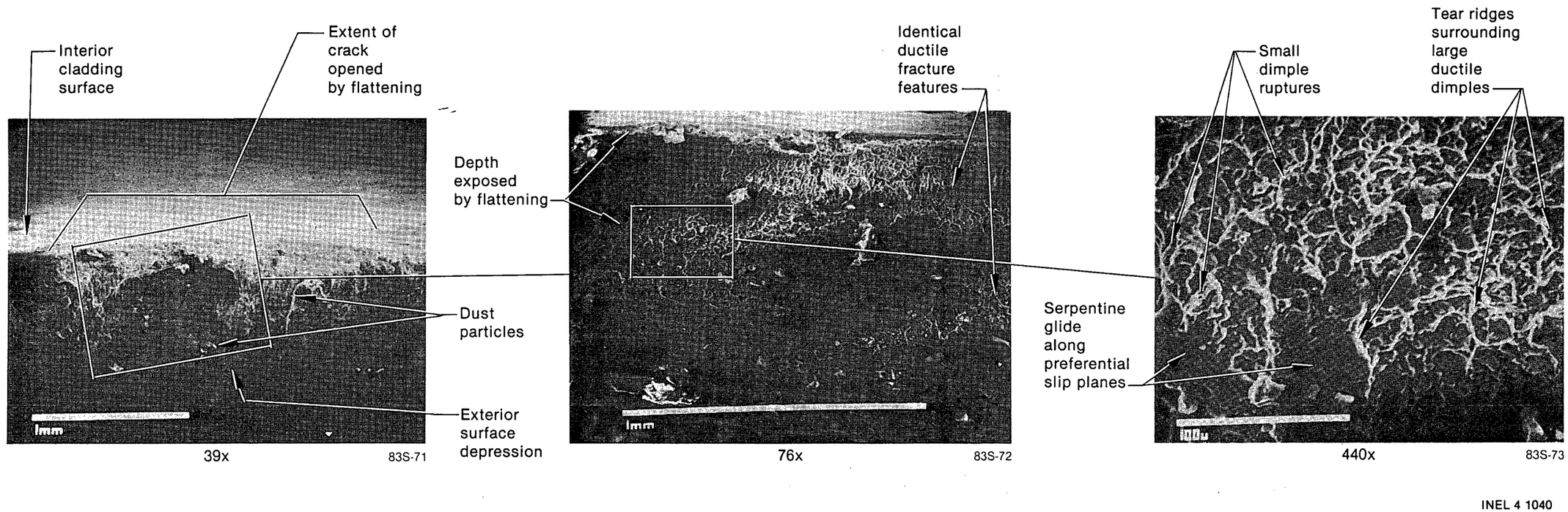

Figure 43. SEM fractography of Sample C-8 from OPTRAN 1-1 Rod 901-4.

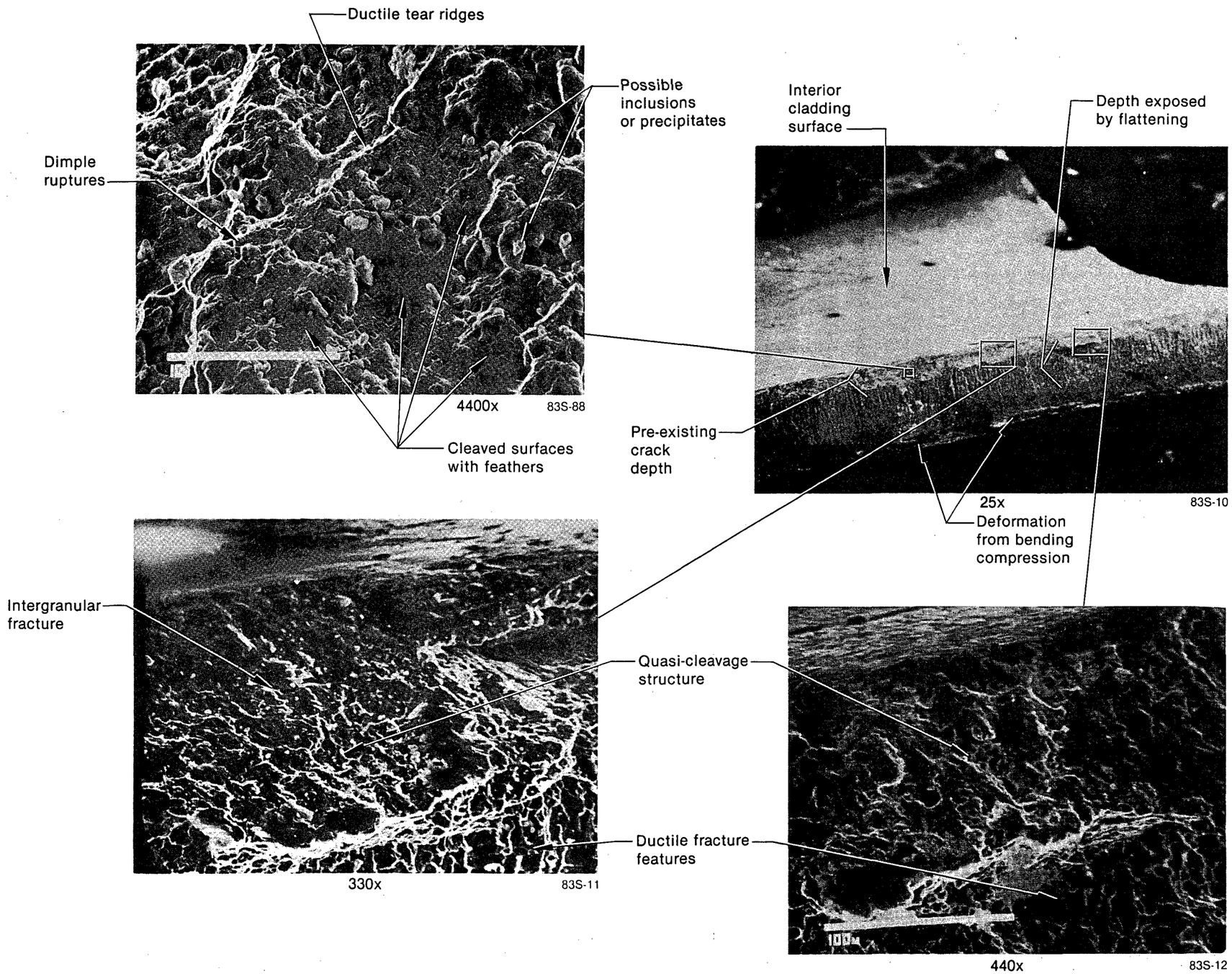

Figure 44. SEM investigations of the incipient crack found in Clamshell C-20 from OPTRAN 1-2 Rod 902-4.

INEL 4 1041

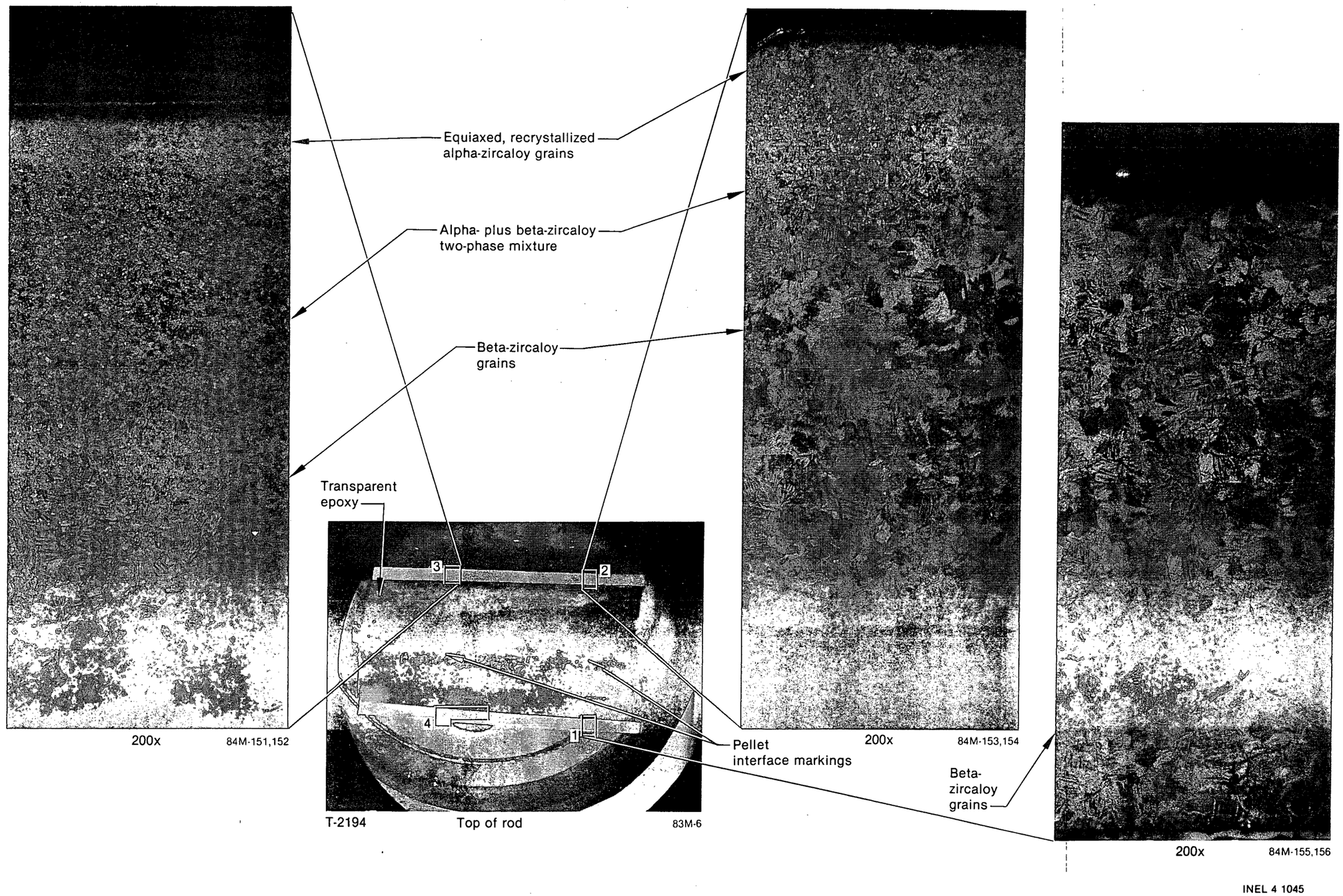

Figure 45. Cladding microstructures near the lower boiling transition boundary on OPTRAN 1-2 Rod 902-4.

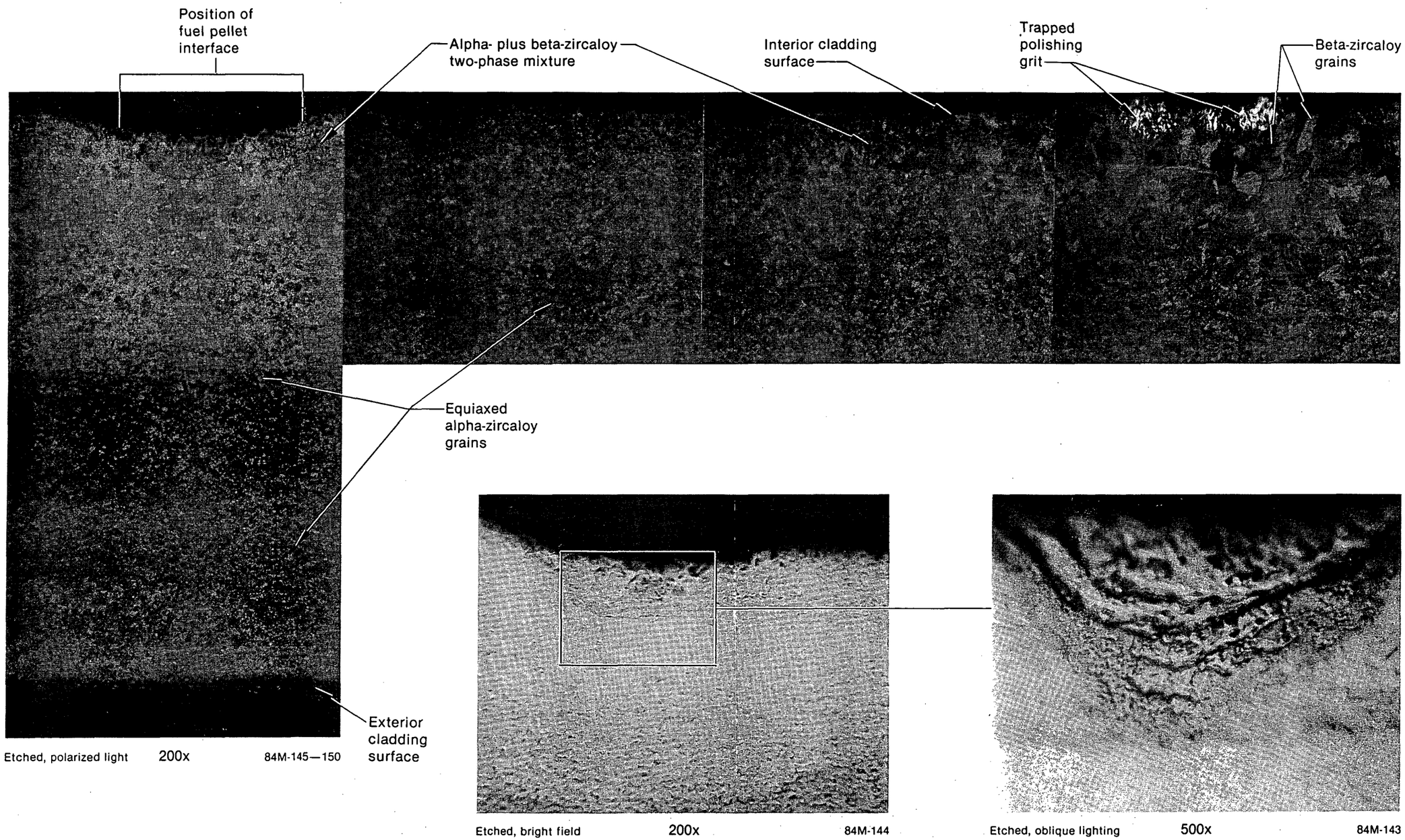

Figure 46. Cladding phase transformations from boiling transition and a possible crack nucleation site on Area 4 of Mount T-2194.

By comparison, the OPTRAN 1-2 Test imposed large cladding stresses suddenly, with only a few seconds for aggressive chemical behavior. Consequently, a small number of well-developed cracks would be predicted from a nucleation-and-growth viewpoint. Furthermore, the short time at elevated fuel temperature during OPTRAN 1-2 and the absence of connected fission product release pathways from low base irradiation powers would have tended to inhibit cladding corrosion. So, perhaps some ductile fracturing should be expected among partially developed brittle fracture features after the brief OPTRAN 1-2 Test.

Another possibility is that PCI-induced stresses might have initiated the C-20 crack without assistance from corrosive fission products. Out-of-pile experiments at Argonne National Laboratory (ANL) have recently induced mixed brittle and ductile fracturing on several stressed cladding samples from the Big Rock Point BWR.[25] The observed fractures propagated from the outside inward—apparently from ferrule compression—so residual fission products on the interior cladding surfaces were not involved. Transmission electron microscopy indicated that oxygen segregation, ZrO_3 phase formation, and dislocation immobilization were responsible for the "pseudocleavage-plus-fluting" morphology on brittle portions of fracture surfaces.

The applicability of the ANL results to the C-20 crack may be limited, however, by differences in cladding strain rate and stress intensity, as well as by the presence of moderate burnup fuel pellets. Furthermore, a fracture mechanism independent of fission products would still not explain why only a single large crack formed in the two OPTRAN 1-2 fuel rods. Thus, stoicheiometric variables like cladding fabrication flaws cannot be excluded from consideration.

Metallographic Findings

One item of interest was whether or not cladding hoop strains exceeded the elastic-to-plastic yield points during the OPTRAN 1-1 and 1-2 transients. External cladding ridges are sometimes found near fuel pellet interfaces after long-duration PCI experiments, especially on rod designs with unchamfered, dished pellets that exaggerate the "hourglass" effect. The OPTRAN fuel pellets had flat ends and chamfers, so any ridges would indicate that particularly large fuel thermal expansion had occurred. Accordingly, 1.9-cm longitudinal metallographic samples were sectioned from Rods 901-1, 901-2, 901-4, 901-6, and 902-4 (two samples) to search for permanent hoop strains. However, no ridges, wall thickness variations, and other types of permanent cladding deformation were detected, which confirmed the nondestructive PIE results in this regard.

Because a boiling transition and cladding temperature increase was measured on each of the OPTRAN 1-2 rods, some amount of enhanced cladding oxidation was predicted. Had dryout occurred for a sustained interval near the C-20 sample, oxygen embrittlement could have been partially responsible for exposing the crack during flattening. As detailed in Appendix E, the mating half of the C-20 SEM sample was mounted for examination of the cladding microstructure adjacent to the crack. However, no microstructural changes were detected and signs of significant oxygen embrittlement were definitely absent. Identical metallographic results were found on the longitudinal sample taken just above Sample C-20 (mount T-2193), which included cladding 2 to 5 cm from the defect elevation. Consequently, formation of the Sample C-20 incipient crack was not influenced by elevated cladding temperatures.

Nevertheless, the upper portion of Rod 902-4 was affected by cladding temperature increases. Although the upper boiling transition boundary was not determined, the lower boundary was found ∿25 cm above the C-20 crack position in metallographic sample T-2194, between Samples C-21 and C-22. (The sectioning diagram, Figure 38, shows that mount T-2194 was ∿60 cm above the bottom of Rod 902-4.)

Mount T-2194 and its range of zircaloy microstructures are presented on Figures 45 (areas 1, 2, and 3) and 46 (area 4). As shown by the etched, polarized-light metallography, area 1 was completely transformed to beta-zircaloy during the dryout phase of the OPTRAN 1-2 transient. Area 2 was over half beta-zircaloy at temperature, most of the remainder was alpha- plus beta-zircaloy two-phase mixture (1103 K to 1243 K), and a thin layer of equiaxed alpha-zircaloy (920 K to 1103 K) lies along the exterior cladding surface. Area 3, at a slightly lower rod elevation, was composed of approximately equal proportions of the three allotropic forms. Area 4 was mainly equiaxed alpha-zircaloy with a thin layer of two-phase mixture at the pellet interface position, but Figure 46 illustrates

how the interior cladding surface had been transformed to beta-zircaloy only 2 mm higher on mount T-2194. (This axial temperature gradient is minor by comparison to the gradient of at least 140 K that existed across the 0.86-mm cladding wall at positions 2 and 3.) Nevertheless, no intrusions of oxygen-stabilized alpha-zircaloy are present within the prior beta-zircaloy fields, so oxygen uptake from the UO_2 fuel and exterior cladding surface ZrO_2 layer was negligible. Consequently, the cladding was not embrittled after cooldown, so no embrittlement fractures occurred during flattening of Samples C-21 and C-22.

High-magnification photomicrographs were made at each of these four areas to determine cladding temperatures from external ZrO_2 layer thicknesses. However, the thicknesses contained considerable variation at each location. Furthermore, the thicknesses on average were indistinguishable from those on mount T-2193, which was located well below the boiling transition region. Therefore, temperature/thickness correlations from isothermal kinetic experiments could not be legitimately applied. The difficulties encountered in this effort were probably related to the large cross-wall thermal gradients and the brief duration of the dryout, which would also have confounded evaluations of better oxide thickness data.

Despite having no accurately estimated maximum cladding temperatures, the microstructures of mount T-2194 dictate that the cladding at this elevation was quite ductile during the dryout period. Since Rod 902-4 was unpressurized, the 7.93-MPa PBF coolant system pressure would have exceeded the internal rod pressure throughout OPTRAN 1-2. Thus, inward cladding deformation was predicted to occur, particularly waisting into pellet chamber gaps.[26] Yet, no evidence of waisting, ridges, and wall thickness changes was found. However, these metallographic results do not exclude two-point buckling and uniform circumferential collapse over the dryout regions, since these types of cladding deformation leave no telltale local indications.

The unusually large thermal gradients, the negligible oxygen embrittlement, and the absence of waisting on mount T-2194 can all be explained by the short boiling transition duration. The functional cladding surface thermocouples 70 mm above the fuel stack midpoints on Rods 902-2 and 902-4 both indicated dryout for $\sim$11 s. Fuel temperatures evidently dropped rapidly before thermal equilibrium could be reached across adjacent cladding walls, so the phase transformations shown for areas 2 and 3 of Figure 45 were effectively frozen in place. Because outer cladding temperatures lagged behind those at interior surfaces, growth of the external ZrO_2 layer and inward diffusion of oxygen were less than the well-developed beta-zircaloy grains next to fuel pellets would suggest. Cladding ductility is also a strong function of temperature, so external portions would have been relatively resistant to deformation during the boiling transition. Even at area 1, where the entire wall was transformed to beta-zircaloy, the outer surface would have been in a high-ductility regime for a few seconds at most—insufficient time for plastic flow into pellet chamfer gaps. This explanation presumably applies elsewhere over the dryout regions of the OPTRAN 1-2 test rods, because no waisting and embrittlement were detected during nondestructive testing and clamshell-flattening efforts.

A final feature of interest on Figures 45 and 46 is the presence of an interior surface concavity coincident with the pellet interface position on each cladding wall composite. These smooth, semicircular depressions are not related to waisting, which thickens the cladding wall at pellet junctions and produces indentations on the exterior cladding surface. Under oblique lighting, the area 4 concavity on Figure 46 resembles a corrosion pit with preferential attack along grain boundaries, so these features might be nucleation sites for PCI cracks. Their tiny size (by comparison to the incipient crack lower on Rod 902-4) may be due to growth termination when cladding temperatures climbed during the boiling transition. Recent Karlsruhe research indicates that the critical iodine concentration for stress-corrosion cracking increases strongly with temperatures, such that realistically available iodine amounts fall below the damage threshold at $\sim$1000 K.[27] Enough reactive iodine could have been released early during OPTRAN 1-2 to nucleate corrosion sites at this elevation, but crack propagation might have been preempted by the cladding temperature increase.

Nevertheless, occurrence of stress-corrosion cracking in Rod 902-4 remains speculative, even in small isolated locations. Had these concavities been caused by corrosive fission product attack, they should also have been detected on mount T-2193 (near the incipient crack). Furthermore, many well-developed incipient cracks would have been located below the boiling transition where cladding temperatures were ideal for stress-corrosion cracking. Therefore, the significance of the concavities with respect to PCI-induced cladding damage is unknown.

DISCUSSION

The major focus of the OPTRAN 1-1 and 1-2 tests was to evaluate the probability and extent of fuel rod damage during anticipated transient events. The OPTRAN 1-1 transients were representative of anticipated transients with scram including BWR turbine trip without steam bypass, and load rejection without steam bypass. The OPTRAN 1-2 test was representative of the most severe BWR ATWS, the main steam isolation valve closure. Coolant conditions during an ATWS are such that boiling transition can occur and high cladding temperatures can be reached, whereas boiling transition is not reached and cladding temperatures do not increase significantly during anticipated transients with scram. Even when cladding temperatures do increase significantly during an ATWS, the duration of the temperature excursion is brief (a few seconds). Therefore, the mechanism for possible cladding failure in both an anticipated transients with scram and an ATWS is pellet-cladding mechanical interaction.

Based on the measurements of axial rod elongation and the posttest analysis, early axial PCI occurred during OPTRAN 1-1 transients and OPTRAN 1-2. The reasons for the early axial PCI during the transients are that the OPTRAN test rods did not experience any PCI during the steady-state irradiation in the Monticello reactor and the preconditioning in the PBF reactor was performed at power too low for radial PCI to take place and eliminate pellet eccentricity. Thus, the causes of early axial PCI were not eliminated before the transient tests began. As a result of early axial PCI, the axial elongation of the test rods was larger than would be expected without early axial PCI. The significance of early axial PCI with respect to fuel rod behavior is that (a) it affects the calculation of permanent hoop strain if radial hoop strain takes place, and (b) axial stresses may affect the cladding failure due to PCI.[28] Since none of the OPTRAN test fuel rods failed, only the calculations of the permanent hoop strain during OPTRAN 1-2 were affected for this test program.

The posttest calculations indicate that only small amounts of fission products accumulated at grain boundaries at the end of the steady-state operation and preconditioning. The low fission product accumulation at grain boundaries resulted because the time-weighted average rod powers at the Monticello core periphery ranged between only 7.8 and 12.7 kW/m, compared with a BWR 8 x 8 core-average rod power of 18 kW/m. Peak centerline fuel temperatures were calculated to be between 900 and 1200 K during the Monticello irradiation, compared with core average commercial maximum temperatures between 1400 and 1600 K. The lower OPTRAN fuel temperatures led to slower diffusion of fission products within UO_2 grains and prevented appreciable gas bubble accumulation at fuel grain boundaries. Formation of connected porosity and interlinked bubbles at grain faces was also inhibited. Thus, there was little possibility of a burst-type release of corrosive fission products upon pellet expansion and microcracking during OPTRAN power transients. Commercial fuel rods operated at or above average core powers would be expected to release considerably larger portions of their gaseous inventories under comparable circumstances. The differences in fuel temperatures and prospective gas releases could be quite important in exceeding an iodine concentration threshold for stress-corrosion cracking during the OPTRAN tests.

The posttest calculational results indicate that the initial conditions for the operational transients established by the steady-state irradiation and preconditioning are extremely important. The steady-state irradiation of the fuel rods in the Monticello reactor led to only a small amount of calculated fuel swelling because of the low power. Also, the fuel was calculated to experience additional densification during preconditioning because preconditioning fuel temperatures were higher than steady-state fuel temperatures. In addition, the cladding was calculated to experience very little creepdown during the steady-state irradiation. Therefore, at the end of steady-state irradiation and preconditioning, the gap between the cladding and fuel was larger than the as-fabricated gap. The calculated gap in Rods 901-1 and 901-6 at the last of preconditioning was smaller than that in Rod 902-4 because Rod 902-4 had lower burnup and therefore experienced less fuel swelling. As a consequence, the calculated hoop stress for Rod 901-6 during transient OPTRAN 1-1 D was much larger than the calculated hoop stress for Rod 902-4. Based solely on calculated stresses then, the test rods used in OPTRAN 1-1 would be more likely to develop PCI cracks than the test rods used in OPTRAN 1-2.

The peak hoop stress values for OPTRAN 1-1 Transient D and OPTRAN 1-2, while seemingly low, are difficult to place in proper perspective. Had

the OPTRAN rods been irradiated at significantly higher powers in Monticello, fuel swelling (and possibly cladding creepdown) would have occurred to a larger extent. The fuel-to-cladding gap sizes would have been smaller going into the OPTRAN transients, so cladding hoop stresses would have been larger during the transients. Accordingly, it is recommended that FRAPCON II/FRAP-T6 calculations be repeated for core-average and peak-power BWR rods so that quantitative estimates of the low base-power influences can be made.

Even then, predictions on PCI crack formation for higher power rods could not be made without comparisons to hoop stresses in situations where PCI cracks did form. The Studsvik Demo-Ramp II and Trans-Ramp I projects were performed on representative BWR rods and did induce incipient cracks from high power irradiations of less than a one-minute duration. FRAPCON II/FRAP-T6 calculations should also be performed for an appropriate subset of these rods. It is likely that FRAP-calculated hoop stress values during the Studsvik experiments would be much larger than FRAP-calculated stresses for a peak-power BWR rod during OPTRAN 1-1 and 1-2. If so, a strong conclusion could be made that fuel rods would not fail from PCI during similar commercial transients. Alternatively, if peak hoop stresses were found to be approximately equivalent, further assessments of transient fission product releases during both situations by a code like FASTGRASS would be required.

The majority of the fuel rod damage information from the OPTRAN 1-1 and OPTRAN 1-2 tests was provided by PIE. The PIE of the OPTRAN fuel rods was heavily weighted toward detecting and characterizing small cladding defects characteristic of pellet-cladding interactions.

Results of pretest visual examination of the OPTRAN fuel rods indicated no signs of exposure to a severe power excursion except that the two fuel rods from OPTRAN 1-2 were bowed over most of their 75-cm fueled length. The PEC investigations, which have a detection threshold for cladding cracks that are $<10\%$ of the 0.86-mm wall thickness, indicated no incipient cracks propagating from interior cladding surfaces on the seven OPTRAN rods scanned. No permanent hoop strains (ridges) at pellet length intervals were observed and the OPTRAN 1-2 rods PEC scanned indicated that no waisting of ductile cladding into interfacial gaps took place over the high-temperature boiling transition region.

Gases occupying the gap/plenum regions of each OPTRAN fuel rod were withdrawn for composition and volumetric analyses. Results from the rod plenum gas analysis were as expected, with the rods undergoing the mildest OPTRAN 1-1 transient indicating the lowest fission gas release and the rods undergoing the OPTRAN 1-2 transient indicating the highest fission gas release. OPTRAN 1-2 had a higher fission gas release than OPTRAN 1-1 transient D because the fuel centerline temperature was considerably higher for OPTRAN 1-2 than OPTRAN 1-1 (calculated values of 2070 K compared with 1789 K).

The measured fission gas release percentage measured for the OPTRAN tests cannot be applied to typical commercial fuel rods undergoing similar transients because the base irradiation powers of the OPTRAN fuel rods were much lower than commercial average rod powers. Consequently, commercial fuel rods operated at or above core average powers could be expected to release considerably larger portions of their gaseous inventories under comparable transient circumstances.

Cladding clamshell investigations were focused on searching for and characterizing incipient cladding cracks. About 60% of the cladding length was examined on each OPTRAN fuel rod. Three clamshell sections were extracted from each OPTRAN rod. This investigation revealed only one isolated defect that could be classified as an incipient crack. The defect was found on Rod 902-4, an OPTRAN 1-2 rod. The defect was longer than typical PCI induced cladding perforations and it demonstrated a mixture of ductile and brittle fracture modes. Despite these discrepancies, PCI and stress-corrosion cracking cannot be completely disregarded as potential causes for the observed defect. However, because higher cladding hoop stresses were calculated for the OPTRAN 1-1 transient D than for OPTRAN 1-2, PCI cracks would have been more likely to occur on Rod 901-6. This suggests that the incipient crack found on Rod 902-4 is a fabrication defect.

Metallographic examinations show that during the dryout phase of the OPTRAN 1-2 test, cladding material was transformed to beta-zircaloy and cladding temperatures in excess of 1243 K were reached. This is considerably higher than the maximum calculated cladding surface temperature of 1007 K and the maximum thermocouple measured value of 1070 K.

The results of the OPTRAN 1-1 and 1-2 experiments are very encouraging. No fuel rod cladding failures occurred and only one isolated defect that could be classified as an incipient crack could be found. It can be concluded that fuel rods with average powers during irradiation up to 12.7 kW/m subjected to an anticipated transient, represented by the OPTRAN 1-1 tests, will probably not fail, and the only significant damage expected may be fuel rod bowing (fuel rod bowing may have resulted from the geometric constraints of the OPTRAN hardware). Unfortunately, conclusions cannot be reached regarding anticipated transients nor ATWS in general because of the low average irradiation power in Monticello of the OPTRAN 1-1 and OPTRAN 1-2 test fuel rods and because of the poor statistics for these experiments (only eight fuel rods were tested). However, GE is of the opinion that fuel rod failures caused by PCI are just as likely to occur if the rods have not been operated at high power. GE claims that this was secretly confirmed during the Super Ramp Program where fuel rods which had a base irradiation power of 27 kW/m failed at about the same ramp power levels as fuel which had a peak base irradiation power of 17.7 kW/m.

CONCLUSIONS

The OPTRAN 1-1 transients tests were performed to (a) determine the threshold at which light water reactor fuel rods are likely to fail during severe anticipated transients that result in a brief increase in reactor power and (b) identify any fuel and damage mechanisms that might occur. Even though the OPTRAN 1-1 test fuel rods were exposed to maximum powers about 30% larger than the worst anticipated transient expected in a commercial power plant, no test rod failures occurred. In fact, postirradiation examination revealed that no incipient PCI cracks occurred. These results must be qualified because the test rods were irradiated at powers about one-third lower than the average rod power in commercial BWR 8 x 8 reactor, which leads to less release of corrosive fission products that are believed to be necessary to initiate PCI cracks.

The OPTRAN 1-2 transient test was performed to evaluate the probability and extent of fuel rod damage for the most severe BWR ATWS. Such a transient results in the occurrence of boiling transitions with high cladding temperatures (> 1000 K). In addition to rod failure from pellet cladding mechanical interaction, boiling transition can cause cladding oxidation and embrittlement and cladding collapse and waisting. Neither of the OPTRAN 1-2 test fuel rods failed and there was no evidence of cladding collapse and waisting. One incipient cladding crack was found during the postirradiation examination but the incipient crack may have resulted from a manufacturing defect. Again these results must be qualified because the test rods were irradiated at powers about one-third lower than the average rod power in a commercial BWR.

However, for fuel rods irradiated at average powers up to 12.7 kW/m, it can be concluded from the OPTRAN experiments that fuel rod damage will probably not occur during anticipated transients represented by the OPTRAN 1-1 tests, and the only significant damage expected for anticipated transients without scram, represented by the OPTRAN 1-2 test, may be fuel rod bowing.

It is recommended that additional FRAPCON-2/FRAP T6 calculations be performed for core-average and peak-power BWR fuel rods so that quantitative estimates of the low OPTRAN 1-1 and OPTRAN 1-2 base irradiation power influences can be made. This will also require comparisons with FRAPCON-2/FRAP T6 calculated hoop stresses for rods tested in the Studsvik Demo-Ramp II and Trans-Ramp I projects, where incipient cracks did occur during high power irradiations of less than a one-minute duration.

The issue of PCI cladding failures during anticipated transients can only be totally resolved by additional OPTRAN-type tests using high-burnup test rods irradiated at BWR core-average and peak powers.

REFERENCES

1. *An Assessment of Accident Risks in U.S. Commercial Nuclear Power Plants*, WASH-1400, NUREG-75/014, October 1975.

2. F. L. Leverenz, Jr. et al., *ATWS: A Reappraisal, Part III Frequency of Anticipated Transients*, EPRI-801, July 1978.

3. M. F. Lyons et al., *High Performance UO_2 Program First Pinhole Fuel Rod Failure During Center Melt Operation, Assembly EPT-12-C-A*, GEAP-5100 K, 1966.

4. *Proceedings of the KTG/ENS/JRC Meeting on Ramping and Load Following Behavior of Reactor Fuel, November 30 to December 1, 1978.*

5. W. J. Bailey et al., *State-of-the-Technology Review of Fuel Cladding Interaction*, COO-4066-2, PNL-2488 December 1977.

6. J. T. Roberts et al., "On the Pellet-Cladding Interaction Phenomenon," *Nuclear Technology, 35*, August 1977, pp. 131-144.

7. E. E. Lewis, *Nuclear Power-Reactor Safety*, New York: John Wiley & Sons, 1977.

8. J. H. Davies et al., *Irradiation Tests to Characterize the PCI Failure Mechanism*, NEDO-21551, February 1977.

9. C. L. Mohr, *PCI Fuel Failure Analysis: A Report on a Cooperative Program Undertaken by Pacific Northwest Laboratory and Chalk River Nuclear Laboratory*, NUREG/CR-1163, PNL-2755, December 1979.

10. J. T. A. Roberts and H. Ochen, "Improving Nuclear Fuel Reliability," *EPRI Journal*, October 1978.

11. B. A. Cook et al., *Reactivity Initiated Accident Test Series, Test RIA 1-2 Fuel Behavior Report*, NUREG/CR-1842, EGG-2073, January 1981.

12. R. J. Williams, private communication, GE, San Jose, CA, "Inputs for the OPTRAN Test Series," April 7, 1980.

13. G. A. Berna et al., *FRAPCON-2: A Computer Code for the Calculation of Steady State Thermal-Mechanical Behavior of Oxide Fuel Rods*, NUREG/CR-1845, December 1980.

14. L. J. Siefken et al., *FRAP-T6:A Computer Code for the Transient Analysis of Oxide Fuel Rods*, NUREG/CR-2148, EGG-2104, May 1981.

15. M. P. Bohn, *FRACAS-II:A Subcode for the Mechanical Analysis of Nuclear Reactor Fuel Rods*, CDAP-TR-78-038, September 1978.

16. D. G. Franklin, G. E. Lucas, and A. L. Bement, "Creep of Zirconium Alloys in Nuclear Reactors," *ASTM, STP-815*, pp. 16-39.

17. J. S. West, J. E. Kasik, and S. Y. Ogawa, *BWR Fuel Bundle Extended Burnup Program, End-of-Cycle 9 Final Fuel Bundle Examination at Monticello Nuclear Generating Plant*, DOE/ET/34031-16, GEAP-30275, September 1983.

18. D. L. Hagrman, G. A. Reymann, and R. E. Mason, *MATPRO-Version 11 (Revision 2) A Handbook of Materials Properties for Use in the Analysis of Light Water Reactor Fuel Rod Behavior*, NUREG/CR-0479, TREE-1280, Rev. 2, August 1981, pp. 83-98.

19. Ibid. pp. 98-125.

20. V. N. Shah, E. R. Carlson, and G. A. Berna, "Cladding Axial Elongation Models for FRAP-T6," *Proceedings, 7th International Conference on Structural Mechanics in Reactor Technology, Paper No. C3/2, Chicago, August 1983.*

21. L. J. Siefken et al., *FRAP-T6:A Computer Code for the Transient Analysis of Oxide Fuel Rods.* NUREG/CR-2148 (Addendum), EGG-NSMD-2104, June 1983.

22. V. N. Shah and E. R. Carlson, *Fuel Compliance Model for Pellet-Cladding Mechanical Interaction in FRAP-T6*, EGG-SAAM-6510, March 1984.

23. J. Rest, "Volatile and Gaseous Fission Product Source Term Evaluation during Power Ramping Conditions in Water Reactor Fuel Using the Mechanistic FASTGRASS Computer Code," paper presented at the *IAEA Specialists' Meeting on Power Ramping and Cycling Behavior of Water Reactor Fuel, Petten, the Netherlands, September 8-9, 1982.*

24. G. F. Pittinato et al., *SEM/TEM Fractography Handbook*, Metals and Ceramics Information Center, Battelle Columbus Laboratories, December 1975.

25. H. M. Chung and F. L. Yaggee, "Deformation and Fracture Characteristics of Spent Zircaloy Fuel Cladding," paper presented at the *Sixth International Conference on Zirconium in the Nuclear Industry, Vancouver, Canada, June 28-July 1, 1982.*

26. C. S. Olsen, *Zircaloy Cladding Collapse Under Off-Normal Temperature and Pressure Conditions*, NUREG/CR-0203, TREE-1239, April 1978.

27. P. Hofmann and J. Spino, "Stress-Corrosion Cracking Failure Behavior of Zircaloy-4 Tubing at Elevated Temperatures," paper presented at the *Enlarged Halden Program Group Meeting, Loen, Norway, May 23-28, 1983.*

28. B. C. Synett et al., "The Effects of Axial Stress to Hoop Stress Ratio on the Susceptibility of Unirradiated Zircaloy-4 to Iodine Stress Corrosion Cracking," *Journal of Nuclear Materials, 96*, 1981, pp. 160-168.

NRC FORM 335 (2-84) NRCM 1102, 3201, 3202

U.S. NUCLEAR REGULATORY COMMISSION

BIBLIOGRAPHIC DATA SHEET

SEE INSTRUCTIONS ON THE REVERSE

1 REPORT NUMBER (Assigned by TIDC, add Vol. No., if any)

NUREG/CR--3948
EGG-2297

2 TITLE AND SUBTITLE

EXPERIMENTAL RESULTS OF THE OPERATIONAL TRANSIENT (OPTRAN) TESTS 1-1 AND 1-2 IN THE POWER BURST FACILITY

3 LEAVE BLANK

4 DATE REPORT COMPLETED

MONTH	YEAR
6	85

5 AUTHOR(S)

Richard K. McCardell , Scott A. Ploger, Robert D. McCormick
Vikram N. Shah

6 DATE REPORT ISSUED

MONTH	YEAR
6	85

7 PERFORMING ORGANIZATION NAME AND MAILING ADDRESS (Include Zip Code)

EG&G Idaho, Inc.
P.O. Box 1625
Idaho Falls- Idaho 83415

8 PROJECT/TASK/WORK UNIT NUMBER

A

9 FIN OR GRANT NUMBER

A6305

10 SPONSORING ORGANIZATION NAME AND MAILING ADDRESS (Include Zip Code)

U.S. Nuclear Regulatory Commission
Washington, D.C. 20555

11a TYPE OF REPORT

final, technical

b PERIOD COVERED (Inclusive dates)

12 SUPPLEMENTARY NOTES

13 ABSTRACT (200 words or less)

Operational transients occur occasionally in light water reactors when minor malfunctions of certain system components affect the reactor core. Potential effects of such malfunctions include a loss of the secondary heat sink, an increase in system pressure, and, in boiling water reactors (BWR), void collapse and a brief increase in reactor power. This report presents the results of the operational transient Tests OPTRAN 1-1 and OPTRAN 1-2, including a comparison of the data with posttest calculations and the postirradiation examination results. The OPTRAN 1-1 tests simulated operational transients with reactor scram. Four progressively higher and broader power transients at a constant coolant flow rate were performed. The first transient simulated a BWR-5 turbine trip without steam bypass, with fuel rods operating near BWR-6 core average rod powers. The second transient simulated a generator load rejection without steam bypass, with fuel rods operating near core average powers. The last two transients were performed at higher core average peak rod powers than safety analyses predict to be possible in commercial reactors to define failure threshold margins.

Test OPTRAN 1-2 was performed to evaluate the probability and extent of fuel rod damage for the most severe BWR anticipated transient without scram (ATWS) that results in boiling transition, a main steam line isolation valve closure transient without scram. Two sets of two fuel rods were tested. In each set, an unirradiated fuel rod was used to heat the coolant to typical BWR conditions for each previously irradiated fuel rod. Following an extensive fuel conditioning period of operation, a single power transient was performed that simulated the power history and coolant conditions calculated for a main steam line isolation valve closure ATWS.

14 DOCUMENT ANALYSIS a KEYWORDS/DESCRIPTORS

b IDENTIFIERS/OPEN ENDED TERMS

15 AVAILABILITY STATEMENT

unlimited

16 SECURITY CLASSIFICATION

a (This page)

b (This report)

unclassified

17 NUMBER OF PAGES

73

18 PRICE

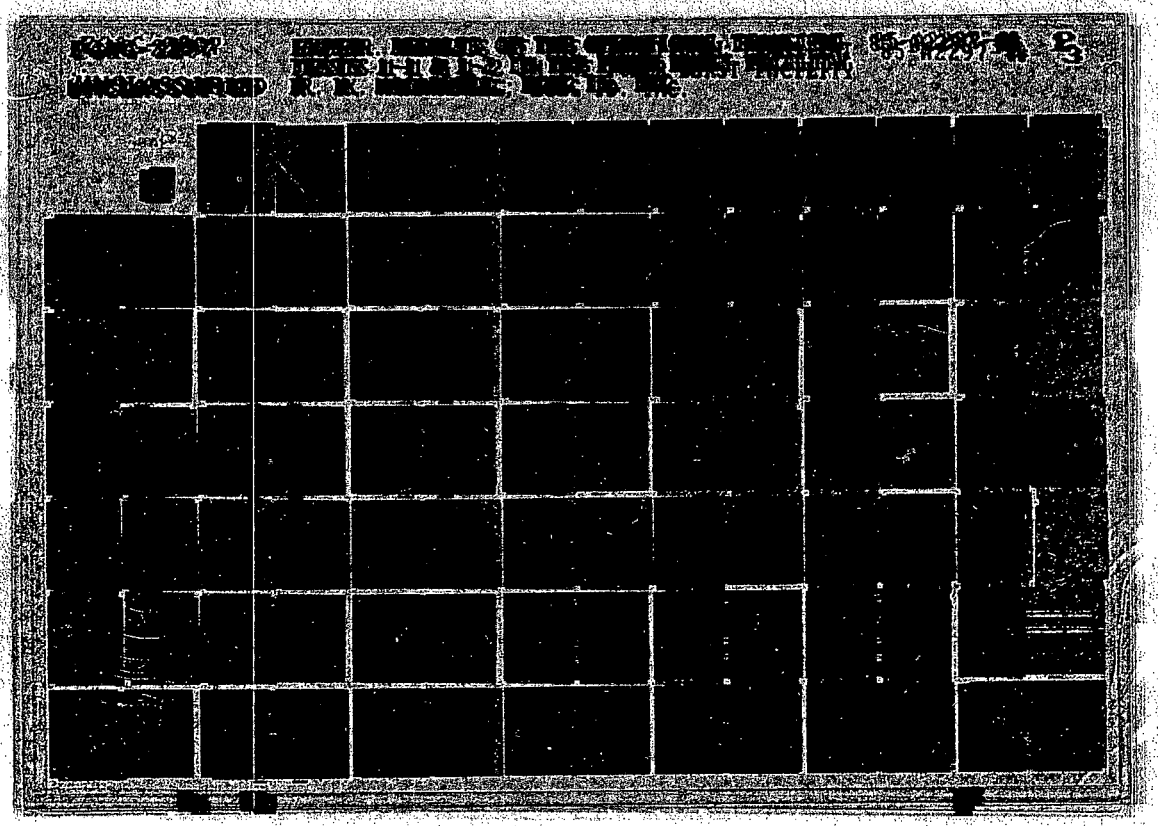

EG&G Idaho, Inc.
P.O. Box 1625
Idaho Falls, Idaho 83415